IMT School for Advanced Studies, Lucca
Lucca, Italy

Towards digital twins for the intestinal motility: from pathologies simulation to therapeutic strategies

PhD Program in Systems Science

Track in Computational Mechanics

XXXVIII Cycle

By

René Thierry Djoumessi

2026

The dissertation of René Thierry Djoumessi is approved.

PhD Program Coordinator: Alberto Bemporad, IMT School for Advanced Studies Lucca

Advisor: Dott. Pietro Lenarda, IMT School for Advanced Studies Lucca

Co-Advisor: Prof. Marco Paggi, IMT School for Advanced Studies Lucca

Co-Advisor: Prof. Alessio Gizzi, Università Campus Bio-Medico di Roma

The dissertation of René Thierry Djoumessi has been reviewed by:

Prof. Christian J. Cyron, Hamburg University of Technology, Germany

Prof. Paola Nardinocchi, Sapienza - Università di Roma, Italy

Prof. Marcello Vasta, Università Campus Bio-Medico di Roma and University of Chieti-Pescara, Italy

IMT School for Advanced Studies Lucca
2026

Acknowledgements

I would like to express my sincere gratitude to my advisor, Dr. Pietro Lenarda, for his constant support, strategic guidance, and encouragement throughout this work. His valuable advice and efforts in shaping and refining this thesis, as well as providing key resources, were essential to achieving our results.

My deep appreciation goes to my co-advisor, Prof. Alessio Gizzi, for his encouragement, insightful scientific advice, and his constant reminder that meaningful research must be original down to the smallest detail. His expertise on the physiological aspects of this work and his commitment to promoting our research have been invaluable.

I am also grateful to Prof. Marco Paggi, who introduced me to the fascinating field of contact mechanics and continuously supported me in building strong scientific collaborations.

My thanks go to Prof. Leo Cheng, who kindly hosted me at the Auckland Bioengineering Institute in New Zealand, where I gained valuable experimental experience, particularly in measuring electrical wave propagation and contact pressures.

I wish to thank in advance the reviewers of this thesis for their constructive comments that will help improve the quality of this work. I am also thankful to my colleagues and fellow students for creating a friendly and stimulating environment.

Finally, my heartfelt gratitude goes to my parents, Mr. Djoumessi René and Mrs. Doungue Wounkeng Jeanne, for their unwavering emotional support, and to all those who contributed, directly or indirectly, to the completion of this thesis.

To my family

Contents

List of Figures

List of Tables

Vita

June 28, 1994	Born, Bafoussam, Cameroon
2014	Bachelor in Mechanical Design Unversity of Bamenda Bamenda, Cameroon
2016	Master in Mechanical Design Unversity of Bamenda Bamenda, Cameroon
2018	Master in Physics Energyzing Mechanics Unversity of Dschang Dschang, Cameroon
2022	Teaching Assistant Department of Physics Unversity of Dschang Dschang, Cameroon
2024	PhD in Physics Energyzing Mechanics Unversity of Dschang Dschang, Cameroon

Publications

1. R. T. Djoumessi, "In silico model of colon electromechanics for manometry prediction after laser tissue soldering" in *Computer Methods in Applied Mechanics and Engineering*, vol. 426, pp. 116989, 2024.
2. R. T. Djoumessi, "A self-contact electromechanical framework for intestinal motility" in *Computational Mechanics* (2025), https://doi.org/10.1007/s00466-025-02692-4.

Presentations

1. R. T. Djoumessi, "Electromechanical Modeling of Colonic Motility," at *European Society of Biomechanics (ESB 2024)*, Edinburgh, Scotland, 2024.
2. R. T. Djoumessi, "Computational modeling of the effect of laser tissue soldering on colonic motility," at *Virtual Physiological Human Institute conference (VPH 2024)*, Stuttgart, Germany, 2024.
3. R. T. Djoumessi, "Modeling and simulation of the effect of laser tissue soldering in colon electromechanics," at *European Society of Biomechanics Italian Chapter (ESB-ITA 2024)*, Pescara, Italy, 2024.
4. R. T. Djoumessi, "A Generalized electromechanical framework for intestinal motility: Incorporating self-contact," at *8th International Conference on Computational Contact Mechanics (ICCCM 2025)*, Munich, Germany, 2025.
5. R. T. Djoumessi, "Modeling self contact in intestine motility", at *New Horizons In Structural Mechanics, Elasticity and Homogenization (NHISMEH 2025)*, Lucca, Italy, 2025.
6. R. T. Djoumessi, "A Generalized Contact Framework for Patient-Specific Intestinal Motility", at *11th International Conference on Computational Bioengineering(ICCB 2025)*, Rome, Italy, 2025.

Abstract

Gastrointestinal motility is essential for digestion, yet its underlying mechanisms remain poorly understood. The movement of the digestive tract results from a complex interaction between electrical signals, muscle contractions, and physical contact between tissues. Experimental and numerical approaches provide valuable insights, but they struggle to capture all these phenomena in an integrated way, especially under pathological or post-surgical conditions.

To address this limitation, we developed a digital twin model that combines the main physical processes responsible for intestinal movement: the electrical activity that triggers muscle contractions, the mechanical response of the intestinal wall, and contact phenomena that occur when the tissue folds, compresses, or interacts with surrounding organs. The model is based on well-established biological and mechanical principles and was implemented using open-source software. It also includes realistic boundary conditions to account for the influence of neighboring organs.

The simulations successfully reproduced normal intestinal motion patterns and explained the disturbances observed after surgery. Moreover, the model describes how the intestine would behave in cases of post-surgical tissue adhesions or pre-surgical pathologies such as hernias. The results show that tissue mechanical properties and contact-induced stresses strongly affect motility.

In summary, this thesis provides a new approach to explore gastrointestinal disorders and represents a promising tool to support clinical decision-making before and after surgical interventions.

Chapter 1

Introduction

1.1 Context and challenges

The gastrointestinal (GI) system plays a fundamental role in the digestion and absorption of nutrients, and its functioning relies on a complex coordination of biochemical, electrophysiological, and mechanical phenomena (see Fig. 1). Among these, intestinal motility, generated by the contraction of smooth muscle layers, ensures the propulsion of the food bolus while promoting mixing and contact with the mucosa. A deep understanding of these mechanisms is essential, not only for a better grasp of normal physiology but also for the identification and treatment of dysfunctions associated with various gastrointestinal pathologies (Azzouz and Sandeep Sharma, 2018; Sulaiman and Marciani, 2019; Precup and Vodnar, 2019).

The GI wall is a complex multilayered structure (see Fig. 1 c) comprising: serosa (outermost layer), a simple epithelium secreting serous fluid; muscularis externa, containing longitudinal and circular smooth muscles fibers; myenteric plexus containing enteric neurons; submucosa, a dense layer of connective tissues containing large blood and lymphatic vessels; mucosa, formed by three sublayers (epithelium, lamina propria, and muscularis mucosae) and containing villi and microvilli to maximise

the exchange surface.

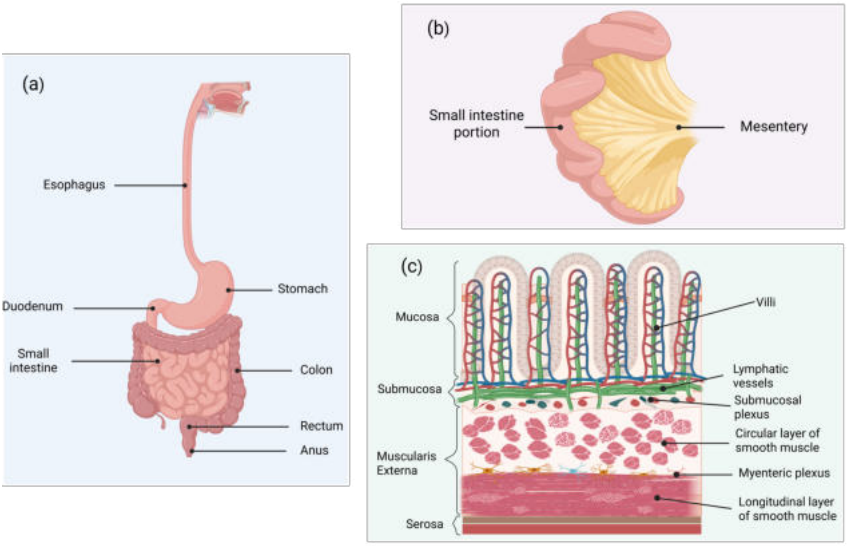

Figure 1: (a) gastrointestinal tract, (b) portion of the small intestine attached to mesentery, (c) structure of the gastrointestinal wall highlighting the different layers with their internal microstructure.

Despite significant advances in gastroenterology, experimentation, and research, many uncertainties remain regarding the precise mechanisms underlying different types of intestinal movements and functions, for instance, peristalsis, segmentation, and nutrient absorption. Their modeling and prediction remain particularly complex. For example, even today, we still do not fully understand what initiates a retrograde movement within an antegrade wave. More importantly, the specific types of waves that differentiate between the various modes of motion remain poorly understood. In reality, the intestinal wall is continuously traversed by slow-wave activity, which represents the fundamental rhythmic oscillation generated by the interstitial cells of Cajal (ICCs). However, the presence of these slow waves alone does not directly induce mechanical contraction. For a contraction to occur, a second type of electrical event known as a spike-burst must be triggered, typically under the influence of an external or neural stimulus (Holland et al., 2021). The activation of these spike-bursts is spontaneous and superimposed on the slow-wave rhythm, yet the underlying mechanisms distinguishing these two types of electrical activity remain poorly understood (Kuruppu, Cheng, Avci, et al., 2022). Experimental (see Figure. 2) investigations have shown that spike-bursts are temporally and spatially coupled with slow-waves: the slow-wave provides the rhythmic framework, while the spike-burst initiates the effective depolarization of smooth muscle cells, leading to contraction. During cyclic peristalsis, longitudinally propagating patches of spike-burst activity have been observed to coincide with slow-wave propagation, producing rhythmic circumferential contractions that drive the peristaltic wave along the intestine. These findings emphasize the intricate electrophysiological interplay governing intestinal motility and the challenges associated with replicating such dynamics in computational models. This experiment was also showing the spatiotemporal transverse strain important to identify the amount of contractions.

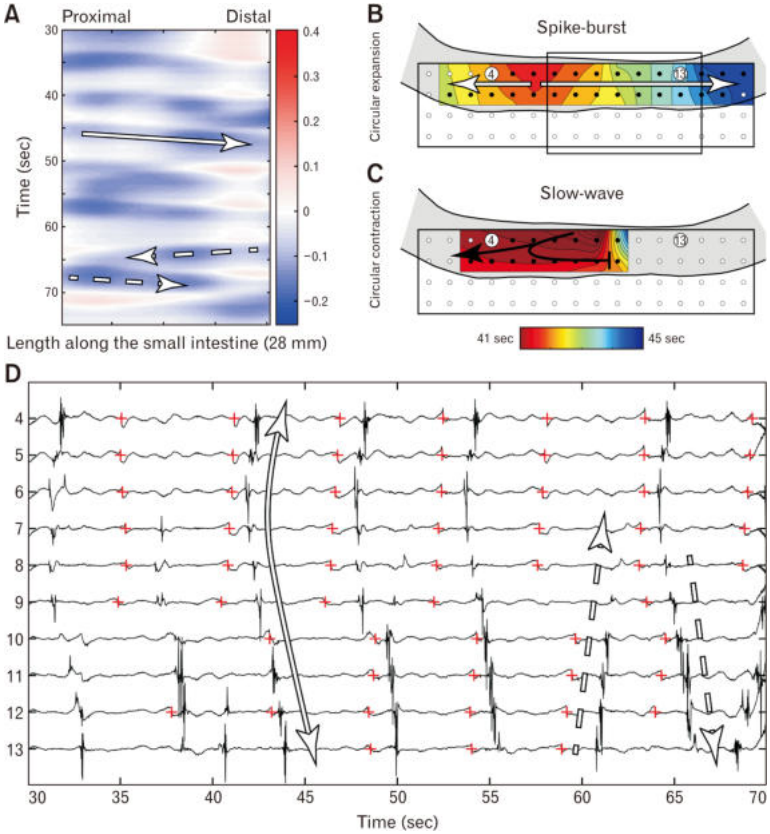

Figure 2: Slow-wave and spike-burst activity during cyclic peristalsis. (A) spatiotemporal transverse strain maps showing propagating contractions during cyclic peristalsis. (B, C) activation maps of spike-burst and slow wave activity corresponding to the contraction marked in (A). (D) electrical traces recorded from a row of electrodes in (B, C); red crosses indicate slow-wave events. Spike-bursts propagate longitudinally in association with slow-waves, producing rhythmic circumferential contractions at the frequency of the slow-waves (Kuruppu, Cheng, Avci, et al., 2022)

In essence, we still do not know precisely when the system decides to perform segmentation or propulsion or even spike-burst. Some studies suggest that the enteric nervous system (ENS) is responsible for triggering such activations and is capable of distinguishing between them

(Athavale, Avci, et al., 2024a; Fung and Vanden Berghe, 2020). However, we still lack sufficient clinical, experimental, and numerical evidence to support this hypothesis. Another major challenge lies in understanding and modeling the fibrous and highly organized structure of the intestinal wall, both from a histological and a functional standpoint. As see in Figure. 3, intestinal peristalsis relies on a complex muscular organization in which the longitudinal and circumferential fiber layers interact in a finely coordinated manner. The interstitial cells of Cajal (ICCs), which are widely distributed throughout the tissue, generate and propagate oscillation waves along the intestinal surface, thereby stimulating the excitable smooth muscle cells (SMCs) responsible for mechanical contraction. However, this activation does not occur simultaneously across all directions (Fung and Vanden Berghe, 2020). During the propagation of a peristaltic wave, when the circumferential fibers contract to locally narrow the intestinal lumen, the longitudinal fibers ahead of the wave relax, facilitating the opening of the intestinal passage. Conversely, when the longitudinal fibers contract to propel the luminal contents forward, the circumferential fibers dilate to reduce resistance to movement (Fung and Vanden Berghe, 2020).

This alternating mechanism, fundamental to intestinal motility, highlights the intricate electromechanical coupling between the circular and longitudinal muscle layers. Its modeling is particularly challenging due to the spatiotemporal coordination imposed not only by the mechanical interaction of these layers but also by the complex neural regulation provided by the enteric nervous system (ENS). ENS (see Figure. 3) forms an extensive intrinsic network composed of sensory neurons, interneurons, and motor neurons organized along the intestinal wall. When a luminal stimulus is detected, sensory neurons activate ascending and descending interneurons that, in turn, connect to excitatory and inhibitory motor neurons (Fung and Vanden Berghe, 2020; Holland et al., 2021). The activation of ascending excitatory pathways induces contraction on the oral side, while descending inhibitory pathways trigger relaxation on the anal side, thereby generating the coordinated propagation of the peristaltic wave. Furthermore, enteric glial cells actively participate in modulating

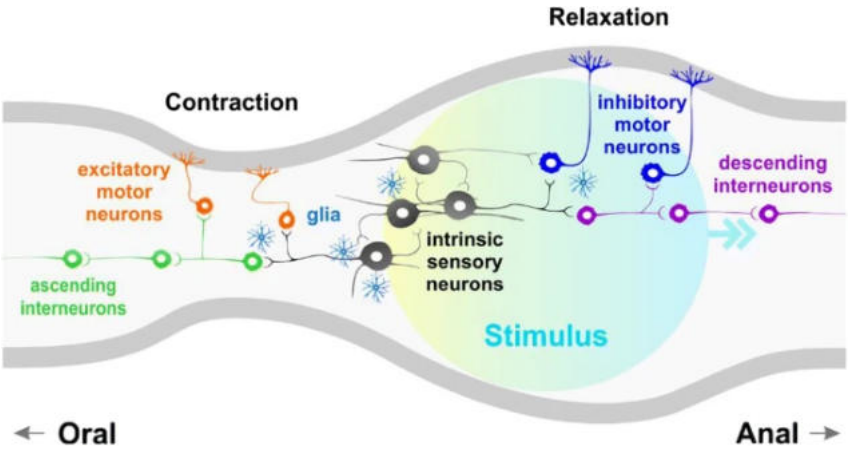

Figure 3: Simplified schematic representing the enteric circuitry underlying the peristaltic reflex (Fung and Vanden Berghe, 2020). Figure reproduced under the terms of the Creative Commons Attribution 4.0 International License (CC BY 4.0). To view a copy of this licence, visit http://creativecommons.org/licenses/by/4.0/.

this process, contributing to the fine regulation of intestinal motility.

1.2 State of the art and motivations

However, all is not lost. Over the past two decades, multiphysics and multiscale models have been proposed to better describe intestinal electrophysiology (Aliev, Richards, and Wikswo, 2000; Sharon and Nisky, 2018; Du, Calder, et al., 2018), passive mechanics (Nagaraja et al., 2021; Patel et al., 2022; Sokolis and Sassani, 2013), and active electromechanics (Brandstaeter et al., 2018; Du, Lim, and Cheng, 2013; Djoumessi, Lenarda, Alessio Gizzi, Giusti, et al., 2024). Compared to cardiovascular research, gastrointestinal modeling lags behind by approximately twenty years, due to the anatomical and functional complexity of the intestine and the lack of reference experimental data. Recent efforts aim to close this gap, particularly through novel experimental devices capable

of simultaneously providing electrophysiological and mechanical data (Patton et al., 2024; Athavale, Di Natale, et al., 2024; Kuruppu, Cheng, Angeli-Gordon, et al., 2024). Although research on the GI system remains generally less documented than that on the cardiac system, this disparity is even more pronounced within the GI tract itself. Studies focusing on the stomach are comparatively more developed, whereas investigations into the intestinal tract—particularly its complex electromechanical behavior—remain scarce. It is precisely this gap that constitutes the central focus of the present thesis.

In this context, numerical simulation and the development of digital twins of the gastrointestinal system open new perspectives for the non-invasive analysis of intestinal motility. These models not only allow the reproduction of intestinal electromechanical dynamics but also provide a virtual platform to test the impact of clinical interventions or pathological conditions. They thus represent a promising tool to improve the understanding of fundamental mechanisms and to support the design of new therapeutic strategies.

Post-surgical complications illustrate the importance of such an approach. for example, after intestinal resection, either anastomosis or endoscopic resection, leakage remains a major complication, severely affecting both prognosis and patient quality of life (Turrentine et al., 2015). Current fixation methods (sutures, staples) may induce discontinuities along the suture line, leading to leakage or pathological scarring (Gizzi, Cherubini, Pomella, et al., 2012; Chadi et al., 2016; Simone et al., 2018). In recent years, laser-based technologies, and in particular laser tissue welding (LTS) and laser tissue welding (LTW), have emerged as innovative alternatives (Gerasimenko et al., 2022; Birkelbach et al., 2020; Basov et al., 2019). The objective of this method is to put the new material on the resection part using laser tissue soldering. They even enable the integration of 3D-bioprinted patches, paving the way for personalized interventions (Chirianni, Vairo, and Marino, 2024; Alduini, 2021). However, their effectiveness depends on the precise adjustment of multiple parameters (compression force, laser power, and exposure time, soldering material) (Nisky et al., 2015; Sharon and Nisky, 2018). Failures may

still occur, either due to insufficiently consolidated welding or to inflammatory reactions leading to fibrosis and local stiffening (Ashbell et al., 2023; Urie et al., 2015; Huang et al., 2013; Mushaben et al., 2018). Nevertheless, such procedures demand exceptional dexterity from healthcare professionals. In addition, the effects of these interventions, whether by suturing or laser soldering, on both the local and global motility of the intestinal tract remain poorly understood, not only among clinicians but also within the research community. This underscores the importance of advancing in silico models as complementary tools to support clinical decision-making and to provide deeper insights into the progression of gastrointestinal.

Beyond these immediate complications, the intestine is particularly prone to self-contact phenomena. Unlike organs protected by a rigid structure, such as the heart or lungs, the intestine is relatively free within the abdominal cavity, its position being regulated by the mesentery (see Fig. 4) and the abdominal wall (Byrnes et al., 2019; Sensoy, 2021). Following abdominal surgery, more than 90% of patients develop complications related to the formation of fibrous tissue or adhesions, which compromise motility (Tabibian et al., 2017; Frager et al., 1996; Cardoz et al., 2024; Furtado, Carvalho, and Garcia, 2024). In the most severe cases, herniation may occur, potentially leading to intestinal strangulation (Jadhav, Adhikari, and Purohit, 2022; Moazzez et al., 2021; Klifto et al., 2021). These phenomena are largely associated with the mechanical interactions between different segments of the intestine, highlighting the necessity of incorporating contact mechanics into numerical models of intestinal motility—an issue that, to the best of our knowledge, has received very little attention in the current literature.

The contact mechanics literature offers various approaches to enforcing surface impenetrability. Nonconforming contact problems require determining the contact area, which is not known a priori, and this challenge becomes even greater in the context of large deformations (Mlika, Yves Renard, and Chouly, 2017). To tackle such issues, various approaches have been proposed, including the Mortar method (Popp, Gee, and Wall, 2009; Popp, Gitterle, et al., 2010; Temizer, Wriggers, and Hughes, 2012).

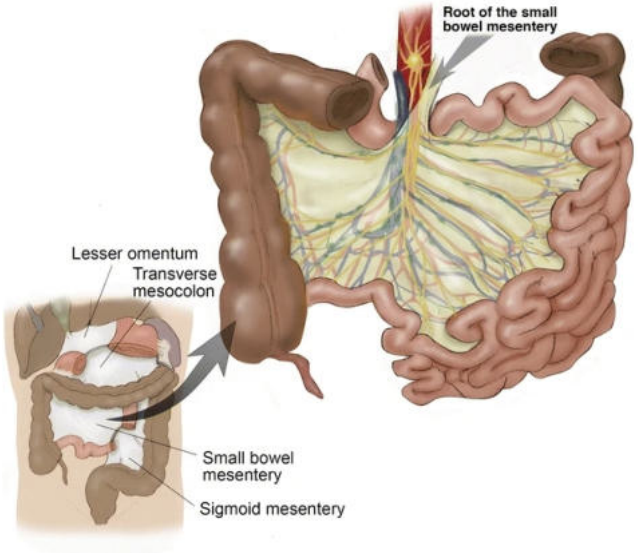

Figure 4: Mesentery attaching to the small and large intestine (Winant et al., 2014).

Among them, master–slave based strategies are the most widely used (Laursen and Simo, 1993; Paggi and Zavarise, 2011; Peter Wriggers, 2006). However, significant difficulties arise in situations involving self-contact or multi-body contact under large displacements, where it is either impossible or impractical to assign master and slave surfaces beforehand due to the evolving nature of the contact configuration. To overcome these challenges, several unbiased contact formulations have been introduced (Sauer and De Lorenzis, 2015; Neto and Peter Wriggers, 2020). The penalty method is widely used due to its simplicity and efficiency (Pore, Thorat, and Nema, 2021; Bozorgmehri et al., 2021; Xuan et al., 2024), though its success strongly depends on the choice of penalty parameter. Moreover, gap computation between contacting surfaces remains computationally expensive (complexity $O(N^2)$), motivating the adoption of acceleration strategies, such as the k-d tree algorithm, which reduces complexity to $O(N \log N)$ (Hou et al., 2018; Kamaludin and Thambu-

raja, 2023) ray-tracing and projection method (K. Poulios and Y. Renard, 2015).

In certain pathological situations, surgery is not always necessary. Instead, clinicians may use alternative techniques to explore or intervene in the intestinal system, such as inserting a catheter or inflating a balloon within the intestine. The goal may be to deploy a prosthesis or use the balloon to restore the intestinal lumen of the GI tract. For example, in diagnostic procedures, controlled rectal distension allows the assessment of visceral sensitivity (Kyloh et al., 2011; Xiao et al., 2024). Modeling these procedures requires accounting for the mechanical contact between the intestine itself and the external devices

Finally, modeling large deformations and intestinal self-contact represents a major challenge. Since soft tissues are nearly incompressible, mixed displacement–pressure formulations are required to avoid volumetric locking (Swati Sharma and Martin Lindsay Buist, 2025). Furthermore, simplified constitutive laws (Neo-Hookean or Saint Venant–Kirchhoff) fail to capture the anisotropy and nonlinearity associated with fibrous microstructures (Nan et al., 2023). These limitations may induce numerical instabilities, especially during folding or extreme fiber proximity, complicating the reliable simulation of intestinal self-contact (Bozorgmehri et al., 2021; Han et al., 2024).

1.3 Objective and plan

In this context, the objective of this thesis is to propose an integrated and robust numerical framework for the electromechanical digital twin modeling of the intestine. First, following the flowchart in Fig. 5 we develop a multiscale and anisotropic model coupling electrophysiology and nonlinear mechanics in order to analyze the impact of LTS on colonic motility. Second, we enrich this model by incorporating contact to explore pathological scenarios. This work thus proposes an original approach combining electromechanics and contact mechanics, with the ambition of providing a digital twin of the intestine capable of shedding light on physiopathological mechanisms and supporting the development of

new therapeutic strategies. However, it is important to note that although we develop an electromechanical model of the gastrointestinal system, the electrophysiological component does not explicitly model any specific type of electrical activity whether slow waves or spike-bursts. Likewise, it does not explicitly represent the ENS, which is believed to be responsible for both the differentiation of wave types and the generation of distinct motility patterns (peristalsis, segmentation, retrograde and antegrade movements).

This thesis is structured as follows: in chapter 2, we first explore the functioning of the intestinal system, from the cellular scale to the organ scale, in order to better understand the key ingredients required for its modeling of the electrophysiology. In chapter 3, we will first present the intestinal electromechanical model together with the calibration techniques employed and the second part focuses on extending the model by incorporating contact mechanics. In chapter 4 we will talk about patient specific data and data assimilation, finally, the last part of this thesis addresses the problems that our model can solve, including certain pathological cases. In chapter 5 we begin by analyzing the outcomes of the electromechanical model without contact mechanics and discuss about the 3D bioprinted material optimization, then in chapter 6 we focus more on the contact model and its application to some pathological conditions. In chapter 7 we summarize the developments achieved throughout this thesis and discuss both its current limitations and future perspectives.

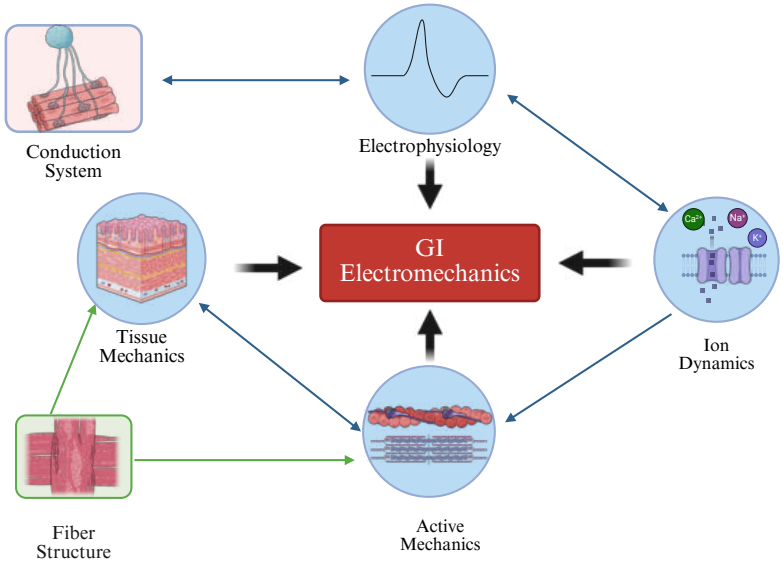

Figure 5: Summary flowchart of the electromechanical coupling, illustrating the interactions between electrophysiology, tissue mechanics, as well as the information exchanged among these components within the modeling framework.

Chapter 2

Electrophysiology of the gastrointestinal system

2.1 Introduction

The electrophysiology of the gastrointestinal (GI) system plays a crucial role in coordinating the various types of intestinal movements. In this chapter, we aim to develop a computational model that captures this complex behavior. We begin by presenting the underlying physiology of the system, followed by a detailed description of how the cells are interconnected, from the smallest cellular scale to the level of the entire organ. We then introduce the modeling framework for GI electrophysiology and discuss its calibration, taking into account existing literature and the state of the art. This chapter provides a comprehensive foundation for understanding and simulating the spatiotemporal coordination of intestinal motility. In this chapter, we adopt the following notational conventions. Scalars are denoted by lowercase letters (e.g., a), vectors by lowercase bold letters (e.g., $\boldsymbol{a}$), and second-order tensors by uppercase bold letters (e.g., $\boldsymbol{A}$). The transpose of a tensor is indicated by $\boldsymbol{A}^T$.

In accordance with standard tensor notation, the scalar (inner) product is represented by $(\cdot)$, the double contraction by $(:)$, and the dyadic (tensor) product by $(\otimes)$. Additionally, the operators ∇, $\nabla\cdot$, and ∇^2 de-

note the gradient, the divergence, and the laplacian, respectively. This convention will be used in the rest of the thesis. Some parts of this chapter are taken from author's previous publication (Djoumessi, Lenarda, Alessio Gizzi, Giusti, et al., 2024).

2.1.1 Gastrointestinal cells and physiology

In the gastrointestinal (GI) system, muscular contractions are coordinated by slow waves originating from interstitial cells of Cajal (ICCs) discovered by the Nobel prize Santiago Ramón Y. Cajal in 1893, a periodic electrical activity essential to motility. These waves are transmitted between smooth muscle cells (SMCs), which contract according to the orientation of their fibers. This coordination arises from the fact that, at the cellular level, interstitial cells of Cajal (ICCs) and smooth muscle cells (SMCs) are interconnected through gap junctions. These junctions enable ICCs and SMCs to activate in a synchronized manner, ensuring efficient propagation of signals. An illustration of this mechanism is provided in Fig 6. The cell membrane of SMCs contains ion channels that regulate the membrane potential (Vm). Depolarization, triggered by an influx of Ca^{2+} and Na^{+}, initiates contraction. This is followed by repolarization due to the activation of potassium channels. Slow waves are generally insufficient to induce significant contractions on their own but serve as a baseline for coordinated motility, with a frequency that varies by region (e.g., 3 cycles/min in the stomach, 10–12 in the duodenum) (Du, O'Grady, et al., 2010; Sanders, Ward, and Koh, 2014).

Interstitial Cells of Cajal (ICCs) as slow wave generators

The ICCs, first described by Ramón Y. Cajal (Du, O'Grady, et al., 2010), are now recognized as the pacemakers of the GI tract. Located within and between muscle layers, they generate and propagate slow waves via gap junctions connecting them to SMCs (Du, Lim, and Cheng, 2013; Du, Calder, et al., 2018). As shown in Figure. 7 Different ICC subtypes exist depending on location (ICC-MY, ICC-IM, ICC-DMP), and they fulfill four major functions: generation of slow waves, neuromuscular trans-

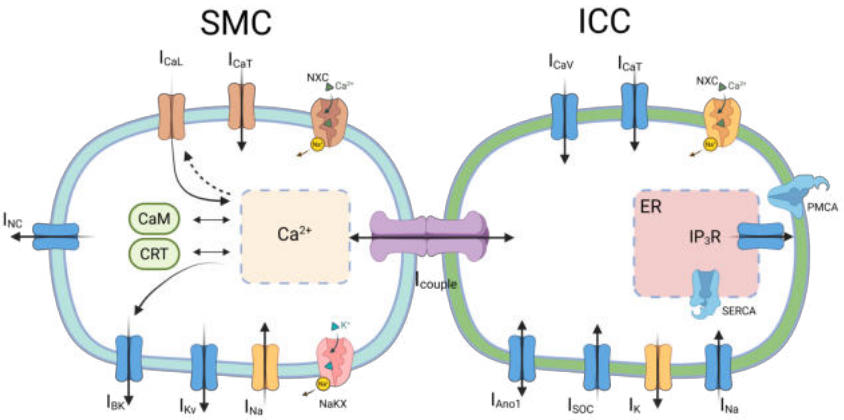

Figure 6: A schematic model of human jejunal smooth muscle cells was coupled to an interstitial cell of Cajal model through a coupling conductance. The symbols used for ion conductances (CaL, CaT, CaV, SOC, PMCA for calcium; BK, Kv, K for potassium; Na for sodium; Ano1 for chloride; NS for non-selective currents; NCX and NaKX for exchangers; Icouple for coupling conductance) and intracellular components (CaM, CRT, ER, SERCA) are consistent with those employed in the original formulations.

mission (notably cholinergic and nitrergic), mechanotransduction, and regulation of the muscle resting potential through gaseous signals (Du, O'Grady, et al., 2010; Du, Calder, et al., 2018). Individually, ICCs exhibit distinct intrinsic frequencies. To achieve effective coordination and smooth wave propagation, some cells entrain others. This mechanism, referred to as entrainment, will be discussed in the following paragraph.

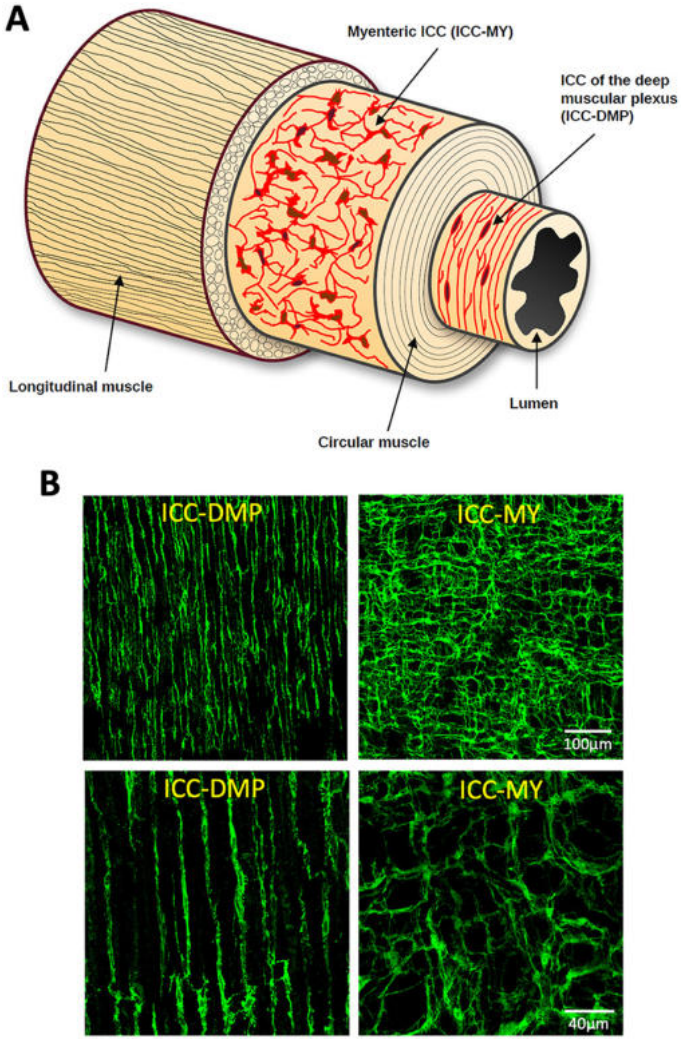

Figure 7: Interstitial cells of Cajal (ICC) distribution across layers of the small intestine. (A) structure of the intestine showing ICC at the level of the myenteric across the intestine layers. (B) confocal images showing on the left show ICC-DMP, while the ones on the right show ICC-MY. Figure reproduced from (Baker et al., 2025) under the terms of the Creative Commons Attribution License (CC BY). 2025 Baker, Blair, Kamran and Sanders

Entrainment and ionic mechanisms in ICCs

Within a functional network, ICCs are entrained to a common frequency, ensuring the efficient propagation of slow waves over long distances (Koh et al., 2003). This implies that when excitation occurs in a given direction, the cells that are activated first transmit their intrinsic frequency to neighboring cells, continuing this process until a stable common frequency is established across the network. This mechanism is essential for ensuring proper synchronization and will be a critical aspect in the calibration of our electrophysiological model, which will be discussed later. The initiation of these waves remains debated between two major theories. The first, IP_3-dependent, suggests that depolarization triggers the production of intracellular messengers (IP_3), leading to the release of Ca^{2+} from the sarcoendoplasmic reticulum. The second, the unitary potential theory, posits that random depolarizations promote this release via T-type Ca^{2+} channels (Faville et al., 2008). Recent studies also emphasize the key role of the Ca^{2+} -activated Cl^{-} channel Anoctamin 1 (encoded by the *Tmem16a* gene) in pacemaker activity. These mechanisms are critical for modeling GI electromechanical processes and for understanding pathologies such as gastroparesis.

Coupling between ICCs and SMCs

In the GI tract, slow waves generated by ICCs do not remain confined to these cells but are transmitted to SMCs through electrical coupling via gap junctions (Hanani, Farrugia, and Komuro, 2005) (see Fig 6). This interaction is bidirectional in most modeling frameworks, with ICCs acting as the source of electrical stimulation for the SMCs. The depolarization of ICC membranes leads to a local change in potential that spreads to adjacent SMCs. Once the membrane potential of SMCs reaches a certain threshold, voltage-gated calcium channels open, initiating muscle contraction.

From a computational perspective, this coupling is often represented by a signal transfer from the ICC network to the SMCs, where the electrical activity of ICCs modulates the SMCs' membrane dynamics (Sanders,

Kito, et al., 2016). This coupling ensures that SMCs depolarize in a synchronized manner, following the rhythm established by ICCs, thus generating coordinated and propagative mechanical contractions along the tract.

2.1.2 Cellular models of the electrical activity

In the literature, two main classes of mathematical models have been proposed to describe the electrical activity of gastrointestinal (GI) cells: biophysically based models and phenomenological models. Biophysical models aim to capture the detailed intracellular mechanisms and ion channel dynamics that underlie slow wave generation. These models are often built upon the Hodgkin-Huxley framework and simulate individual ion conductances, allowing a direct connection between model parameters and experimentally measurable physiological quantities (Hodgkin and Huxley, 1952). Representative examples include the SMC and ICC models by Corrias and Buist Corrias and Martin L Buist, 2007; Corrias and Martin L Buist, 2008, and the ICC model by Faville et al. Faville et al., 2008. These models have contributed significantly to our understanding of cellular electrophysiology in the GI tract. However, it is now recognized that many of them lack important components such as the Ca^{2+} -activated Cl^{-} current, which plays a key role in slow wave initiation and propagation (Corrias, Du, and Martin L Buist, 2013; Yeoh, Corrias, and Martin L Buist, 2017). Ongoing efforts aim to revise and extend these models to better reflect recent experimental findings.

In contrast, phenomenological models do not explicitly model each ionic mechanism but rather aim to reproduce the overall behavior of electrical activity through simplified equations. One such model, and the one adopted in this thesis, is the Aliev model (Aliev, Richards, and Wikswo, 2000). Originally derived from the FitzHugh–Nagumo model, it was designed to simulate intestinal slow waves in idealized geometries such as layered cylindrical structures. The Aliev model introduces a system of two first-order ordinary differential equations (ODEs), with one variable representing the membrane potential u and another a recovery variable

v:

$$\frac{du}{dt} = ku(u-a)(1-u) - v \tag{2.1}$$

$$\frac{dv}{dt} = \epsilon[\gamma(u-\beta) - v] \tag{2.2}$$

This model has the flexibility to differentiate the electrical behavior of ICCs and SMCs by adjusting the parameters γ and β, thus allowing for the simulation of both pacemaker and follower activity. Despite its abstract formulation and lack of direct biophysical grounding, the Aliev model captures key features of slow wave propagation and has been successfully applied in anatomically realistic simulations of gastric and intestinal motility M. Buist et al., 2006. Its computational efficiency, conceptual clarity and less time consuming make it an attractive choice for large-scale electromechanical simulations, such as those developed in this thesis.

2.1.3 Whole-organ models of the electrical activity

The modeling at the the tissue and organ level leads to including the diffusion part in the Eq. 2.2. The electrophysiological model adopted in (Aliev, Richards, and Wikswo, 2000; Gizzi, Cherubini, Migliori, et al., 2010) is herein used and generalized. Although simple, this model preserves the essential features of intestinal electrical dynamics: it maintains the fundamental excitability of the cells (N-shaped nullcline, threshold behavior, fast upstroke, slow recovery), faithfully reproduces experimentally observed macroscopic phenomena (frequency gradients, synchronization plateaus, distal desynchronization, phase breaks, and the reduction of propagation length and duration), and correctly captures the functional interaction between oscillatory ICCs and the excitable SMCs muscle layer, as well as the effects of spatial coupling responsible for wave propagation and phase interruptions. Its simplicity also enables simulations involving hundreds of cells, allowing the exploration of collective behaviors that would be difficult to study using full ionic-current models. In return, the model necessarily sacrifices detailed biophysics: it

does not represent individual ionic currents, channel kinetics, or the exact shape of action potentials, and therefore cannot account for fine-scale molecular mechanisms. Nonetheless, it retains all the dynamical invariants required to investigate slow-wave propagation and coordination.

The SMCs and ICCs layers are labeled with indices s and i, respectively. The resulting system of nonlinear partial differential reaction-diffusion equations describes the coupled dynamics between the transmembrane potential variables, u_s, u_i, and the slow current ones, v_s, v_i:

$$\frac{\partial u_s}{\partial t} = f(u_s) + D_s \nabla^2 u_s - v_s + F_s(u_s, u_i), \tag{2.3a}$$

$$\frac{\partial v_s}{\partial t} = \epsilon_s[\lambda_s(u_s - \beta_s) - v_s], \tag{2.3b}$$

$$\frac{\partial u_i}{\partial t} = g(u_i) + D_i \nabla^2 u_i - v_i + F_i(u_s, u_i) + I^i_{stim}, \tag{2.3c}$$

$$\frac{\partial v_i}{\partial t} = \epsilon_i(z)[\lambda_i(u_i - \beta_i) - v_i], \tag{2.3d}$$

where:

$$f(u_s) = k_s u_s(u_s - a_s)(1 - u_s)\,, \qquad F_s(u_s, u_i) = \alpha_s D_{si}(u_s - u_i)\,, \tag{2.4a}$$

$$g(u_i) = k_i u_i(u_i - a_i)(1 - u_i)\,, \qquad F_i(u_s, u_i) = \alpha_i D_{is}(u_s - u_i)\,. \tag{2.4b}$$

Here, I^i_{stim} is the stimulation currents applied to the ICCs; D_s, D_i are the diffusivities (assumed isotropic); λ_s, λ_i are the coupling factors between the membrane potential and recovery variable; D_{si}, D_{is} are the diffusivities of the gap junctions between the two cell species; $k_i, k_s, a_s, a_i, \alpha_s, \alpha_i$ are phenomenological model parameters and their values are provided in Table. 1. The parameter $\epsilon_i(z)$, which is proportional to the oscillation frequency of the ICCs cells, represents a space-dependent excitability function, decreasing with distance from the pylorus (Aliev, Richards, and Wikswo, 2000).

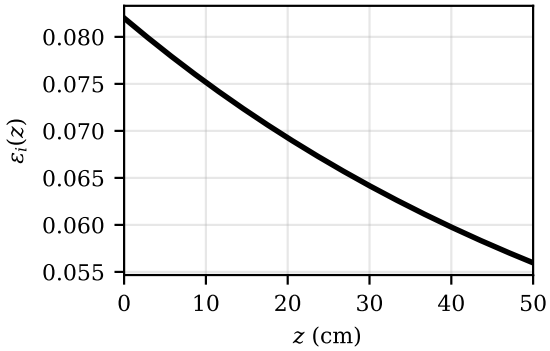

Figure 8: Plot of the excitability parameter $\varepsilon_i(z)$ for the ICC layer. The spatial coordinate z represents the axial distance from pylorus or the centerline length.

The excitability parameter $\epsilon_i(z)$ (z is the distance) of the ICC layer is defined as a function of the distance from the pylorus, in accordance with the experimental interpolation reported in (Aliev, Richards, and Wikswo, 2000), and can be expressed analytically as, $0.032+0.05\exp\left(\frac{-z}{68}\right)$ (see (Gizzi, Cherubini, Migliori, et al., 2010)).

As explained in the preceding in first subsection, the interstitial cells of Cajal (ICC), which are distributed throughout the intestinal wall, act as the pacemaker cells that drive the activity of the smooth muscle cells (SMC). In Eq. (2.3), the parameters were chosen such that the SMC remain in an excitable state, while the ICC operate in an intrinsically oscillatory regime. Only the ICC excitability parameter depends on the axial coordinate z. The excitability $\epsilon_i(z)$ is proportional to the intrinsic oscillation frequency of the ICC along the intestinal tract. Figure 8 illustrates how this excitability varies as a function of the axial distance from the pylorus, emphasizing the physiological gradient of pacemaker activity along the intestine. The parameter β shifts the system's equilibrium point from the stable branch of the nullcline (LM layer) to the unstable branch (ICC layer). The nonlinear functions $f(u_s)$ and $g(u_i)$ represent the cubic bistable Zel'dovich term (Zel'dovich and Frank-Kamenetsky,

1938), characteristic of excitable tissues, while the terms $F_s(u_s, u_i)$ and $F_i(u_s, u_i)$ ensure a symmetric but opposite coupling of the four equations through parameters α_s and α_i. This interlayer coupling is proportional to the oscillation frequency of the ICCs and has been adjusted to reproduce experimental observations, assuming as a first approximation that these values are plausibly valid for humans in the absence of specific human data. The coefficients D_s and D_i reflect strong internal coupling within the SMCs layer, contrasting with weaker coupling between the two layers and within the ICC layer. The importance of conductance in the SMC layer should be emphasized: unlike cardiac myocytes, only a few gap junctions have been observed, necessitating large values of D_{is} and D_s, but a relatively small value of D_i, to achieve a good fit with experimental data.

Additionally, no flux boundary conditions are considered for the electrophysiology:

$$D_s \nabla u_s \cdot \boldsymbol{n} = 0, \quad D_i \nabla u_i \cdot \boldsymbol{n} = 0 \quad \text{on} \quad \partial\Omega_N, \tag{2.5}$$

where $\partial\Omega_N$ stands for the Neumann boundary (the whole boundary for the electrophysiology).

As described in subsection 2.1.1, the entrainment of slow waves generated by interstitial cells of Cajal (ICC) is a crucial step, not only to enforce a common oscillation frequency among the cells, but also to ensure proper coordination of the resulting contraction waves. In this thesis, a dedicated procedure was developed for this purpose (see Section. 2.2). This approach enabled us to determine the time at which the ICC reached a common frequency and stabilized their dynamics on a limit cycle in phase space. This synchronization step is essential to enable a consistent coupling between electrophysiology and mechanics, which will be discussed in detail in the Chapter 3.

2.1.4 Electrophysiological problem

In this thesis, the finite element has been used to solve all the governing equations, but before going in deep in the next section, a step here is important to show how we discretized this equations (this will be recalled

Table 1: Electrophysiological parameters adapted from (Aliev, Richards, and Wikswo, 2000; Gizzi, Cherubini, Migliori, et al., 2010).

SMC layer		ICC layer	
k_s=10	a_s=0.06	k_i=7	a_i=0.5
$\beta_s = 0$	λ_s=8	$\beta_s = 0.5$	λ_i=8
ϵ_s=0.15	α_s=1	ϵ_i=$\epsilon_i(z)$	α_i=-1
D_{si}=0.3	D_s=0.4	D_{is}=0.3	D_i=0.04

again in the next chapter). From the strong form of the Eq. 2.3, The weak form of the electrophysiology can be written as follows: at each time step $t^{n+1} = t^n + \Delta t$ of an equispaced partition of the time interval $[0, T]$, given the solution of the electrophysiology problem at the previous timestep $(u_s^n, v_s^n, u_i^n, v_i^n) \in V^4$ find the vector $(u_s^{n+1}, v_s^{n+1}, u_i^{n+1}, v_i^{n+1}) \in V^4$ at the current timestep t^{n+1} such that it is satisfied

$$\int_{\Omega_0} \frac{u_s^{n+1} - u_s^n}{\Delta t} \delta u_s + \int_{\Omega_0} D_s \nabla u_s^{n+1} \cdot \nabla \delta u_s = \int_{\Omega_0} I_{ion}^s(u_s^n, v_s^n, u_i^n) \delta u_s \,, \tag{2.6a}$$

$$\int_{\Omega_0} \frac{v_s^{n+1} - v_s^n}{\Delta t} \delta v_s = \int_{\Omega_0} R_s(u_s^n, v_s^n) \delta v_s \,, \tag{2.6b}$$

$$\int_{\Omega_0} \frac{u_i^{n+1} - u_i^n}{\Delta t} \delta u_i + \int_{\Omega_0} D_i \nabla u_i^{n+1} \cdot \nabla \delta u_i = \int_{\Omega_0} I_{ion}^i(u_s^n, v_i^n, u_i^n) \delta u_i \,, \tag{2.6c}$$

$$\int_{\Omega_0} \frac{v_i^{n+1} - v_i^n}{\Delta t} \delta v_i = \int_{\Omega_0} R_i(u_i^n, v_i^n) \delta v_i \,, \tag{2.6d}$$

for all test functions $(\delta u_s, \delta v_s, \delta u_i, \delta v_i) \in (V_0)^4$, where:

$$I_{ion}^i(u_s, v_i, u_i) = g(u_i) - v_i + F_i(u_s, u_i) + I_{stim}^i \,, \tag{2.7a}$$

$$R_i(u_i, v_i) = \epsilon_i(z)[\lambda_i(u_i - \beta_i) - v_i] \,, \tag{2.7b}$$

$$I_{ion}^s(u_s, v_s, u_i) = f(u_s) - v_s + F_s(u_s, u_i) + I_{stim}^s \,, \tag{2.7c}$$

$$R_s(u_s, v_s) = \epsilon_s[\lambda_s(u_s - \beta_s) - v_s] \,. \tag{2.7d}$$

The implicit Euler scheme for the discretization of the time derivative has been adopted in Eqs. (2.6), while an explicit treatment of the reaction

terms has been used Eq. 2.7 are considered. In a more compact notation, the electrophysiology problem can be written as: find u_s, u_i, v_s and v_i such that

$$\mathcal{E}(u_s, u_i, v_s, v_i; \delta u_s, \delta u_i, \delta v_s, \delta v_i) := \mathcal{E}_1 + \mathcal{E}_2 + \mathcal{E}_3 + \mathcal{E}_4 = 0\,, \tag{2.8}$$

for all test functions $\delta u_s, \delta u_i, \delta v_s, \delta v_i$, where:

$$\mathcal{E}_1 = \mathcal{E}_1(u_s, u_i, v_s; \delta u_s, \delta u_i, \delta v_s)\,, \tag{2.9a}$$

$$\mathcal{E}_2 = \mathcal{E}_2(u_s, v_s; \delta u_s, \delta v_s)\,, \tag{2.9b}$$

$$\mathcal{E}_3 = \mathcal{E}_3(u_s, u_i, v_i; \delta u_s, \delta u_i, \delta v_i)\,, \tag{2.9c}$$

$$\mathcal{E}_4 = \mathcal{E}_4(u_i, v_i; \delta u_i, \delta v_i)\,, \tag{2.9d}$$

are respectively the residuals of Eqs. (2.6).

2.2 Entrainment analysis of the ICC cells and mesh convergence analysis

2.2.1 Entrainment analysis of the ICC cells

As we said previously, entrainment is one of the most significant mechanisms in gastrointestinal electrophysiology. This phenomenon is inherent. The excitability parameter $\epsilon_i(z)$ and, consequently, the intrinsic frequency of electrical oscillations at the cellular level are larger in the upper than in the lower portion of the gastrointestinal tract. Excitability and frequency in the stomach are obviously higher in the proximal region than in the distal region near the pylorus. Similarly, the pylorus has a greater frequency than the duodenum, which has a higher frequency than the jejunum and we have the same behavior in the colon. This implies that the oscillation frequencies of the ICCs in these areas would differ greatly if they were isolated. However, the ICCs in the lower region are trained due to the cellular interaction at the tissue and organ level and for good movement coordination. In other words, despite their intrinsic frequency differences, the ICC become entrained by their neighbors and are ultimately forced to oscillate at a shared, coordinated frequency.

Based on this theory, we simulated for 1000 s the Eq. 2.6 on a computational domain which was a hollow 3D cylinder of length 50 cm, the external diameter of 5cm and the tickness of 0.55cm. To determine the frequency, we then extracted the data along a line that extended from [0,50] cm (the length of the cylinder). Figure . 9 depicts the frequency gradient's temporal progression. Initially, every point or cell exhibits its own frequency of oscillation. As a result, at $t = 0s$, there is a noticeable frequency gradient throughout the domain. Gradient reduces with time. The electrical oscillations of the ICCs demonstrate nearly constant frequency from $t = 550s$, which is the same as the ICC's initial frequency in the top region of the domain (i.e. at $z = 0$).

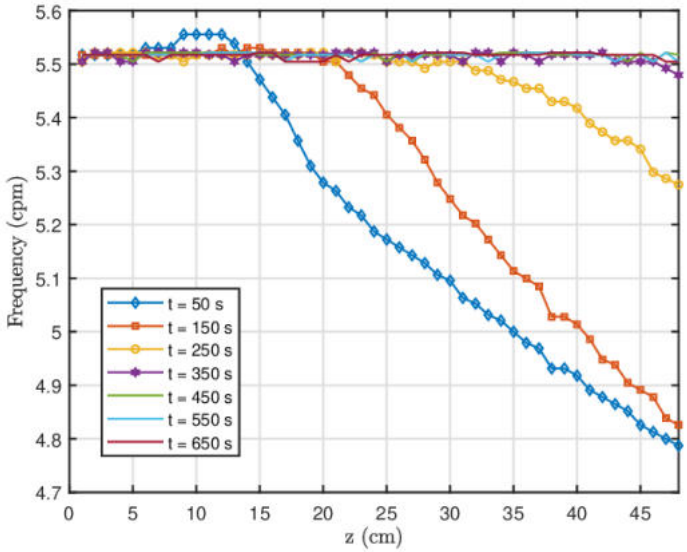

Figure 9: Temporal evolution of the frequency of the ICC at each point

This suggests that these pacemaker ICCs in the upper portion of the domain have driven the ICCs at the other end. Horizontal straight lines show that training from $t = 550s$ is consistent throughout the domain. This outcome ensures that the model can replicate a physiological entrainment procedure. In order to validate this behavior, we present in Fig.10 the progression of the phase portrait for the two electrophysiological state variables for SMC and ICC from their intrinsic to entrained states. The last 450 seconds, which we have highlighted in red, demonstrate how both cell types form a stable limit cycle. This indicates that, after 550 seconds, the system has stabilized. Brandstaeter et al. (2018) were the first to perform this kind of analysis. The ability of this analysis to solve the electrophysiological problem alone for up to 550 seconds before linking it to the mechanics problem is a crucial feature.

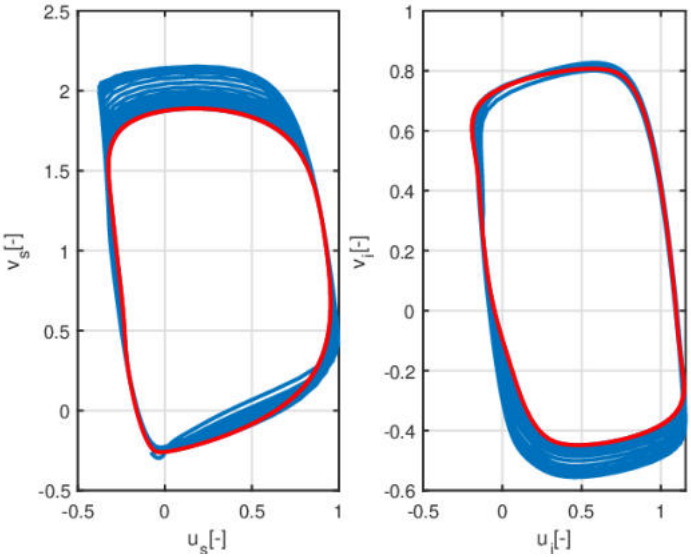

Figure 10: Development of the phase portraits from the intrinsic to the entrained state of ICCs (right) and SMCs (left) located in the middle of the domain at $z = 25cm$. The resulting stable limit cycle is shown in red.

2.2.2 Mesh convergence analysis

To assess the accuracy of the numerical scheme described in the previous section, we carried out the convergence of the electrophysiological solver towards the physical solution as a function of the number of degree of freedom (DoF). For this purpose, we consider the same cylindrical domain as in the previous subsection. For simplicity and to facilitate the implementation of this test, the domain is constructed directly in `FEniCS` (Alnæs et al., 2015) and triangular lagrangian finite elements and a homogeneous mesh of size are used. Different refinements are considered based on the number of subdivisions N from 50 to 450 with the step of 50. Each simulation runs for a total duration t = 800 s with a constant time step $\Delta t = 0.1\text{s}$.

It is well known that the conduction velocity (CV) of reaction-diffusion systems generally depends on the numerical scheme. This analysis aims to obtain a physiologically acceptable CV (Quarteroni et al., 2017).

We calculated the conduction velocity at points located in the middle of the domain to avoid contamination of the boundary conditions. To compute the conduction velocity, we assumed that the slow wave propagated in an approximately planar manner (no propagation in the thickness) along a dominant direction from proximal to distal. Two interior points, sufficiently far from the boundaries to avoid edge effects, were selected; since their coordinates were known, the distance between them could be directly calculated. The arrival time of the activation front at each point was then identified using a threshold potential V_{p}, defining the front passage as the first instant at which the local potential exceeded this threshold. The corresponding arrival times, denoted t_1 and t_2, enabled the conduction velocity to be computed using $CV = d/(t_2 - t_1)$, where d is the distance between the two points. This straightforward procedure thus provides a robust estimate of the slow-wave propagation speed. Figure.11 shows us the evolution of the conduction velocity as a function of the degrees of freedom. we see that a coarse mesh tends to

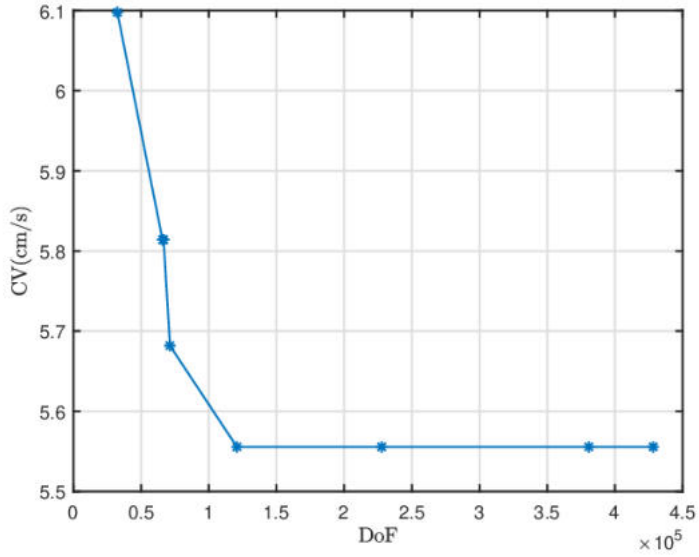

Figure 11: conduction velocity analysis

overestimate the conduction velocity. The more the number of degrees of freedom increases, the more the conduction velocity tends towards a stable value. This simulation also shows us that the conduction velocity is within the range of physiologically acceptable values (Sanders, Ward, and Koh, 2014).

2.3 Conclusion

In this chapter, the objective was to develop an electrophysiological model of the intestine. To achieve this, we began by explaining the functioning of ICCs and SMCs, from the microscopic to the macroscopic scale. We then presented a brief state of the art, highlighting several existing models. Once this groundwork was established, we proceeded to formulate and generalize the electrophysiological model of the intestinal system. The resulting model was validated and calibrated through convergence

tests and an entrainment analysis — a key process ensuring proper coordination between ICC activity and muscle contractions.

In the following chapter, we will address how this problem can be coupled with the mechanical behavior of the tissue. To facilitate the reader's understanding, some of the governing equations will be revisited in the next chapter, which will focus on tissue mechanics, electromechanical coupling, contact interactions, and finite element discretization.

Chapter 3

Electromechanics and contact mechanics

3.1 Introduction

In this chapter, we develop the mechanical formulation of the intestinal tissue as well as the electromechanical coupling. Since, during its function, the intestine can come into contact with itself, a contact mechanics formulation was implemented to account for self-contact effects using the penalty method. To further generalize the treatment of contact mechanics, we also introduce an alternative approach to model interactions between the intestine and external bodies. Specifically, we focus on the contact between the intestine and a balloon, allowing us to reproduce certain experimental tests that will be presented in the following chapter.

The structure of this chapter is as follows: we first present the fundamental aspects of intestinal tissue mechanics, then develop the corresponding mechanical model. Next, we couple this model with the electrophysiological model developed in the previous chapter. We then discuss the formulation of contact mechanics and conclude with the numerical implementation of the problem. Some parts of this chapter are taken from author's previous publication (Djoumessi, Lenarda, Alessio Gizzi,

Giusti, et al., 2024; Djoumessi, Lenarda, Alessio Gizzi, and Paggi, 2025).

3.2 Mechanics of the gastrointestinal tract

Kinematics of deformable GI tissue is embedded in the classical description of continuum mechanics under the assumption of finite elasticity (Holzapfel, 2002).

Let $\boldsymbol{X},\ \boldsymbol{x}$ be the material position vector in the undeformed and deformed configuration $\Omega_0,\ \Omega_t \subset R^d$, $d = 2, 3$ respectively of the GI. The deformation gradient tensor and its associated Jacobian are denoted as $\boldsymbol{F} = \partial \boldsymbol{x}/\partial \boldsymbol{X}$ and $J = \det \boldsymbol{F} > 0$, the right Cauchy-Green deformation tensor with $\boldsymbol{C} = \boldsymbol{F}^T\boldsymbol{F}$, the first isotropic invariant of deformation with $I_1(\boldsymbol{C}) = \text{tr}\,(\boldsymbol{C})$, where $\text{tr}\,(\cdot)$ is the trace operator, and the fourth anisotropic pseudo-invariant is $I_4(\boldsymbol{C}) = \boldsymbol{C} : \boldsymbol{G}$, where $\boldsymbol{G}$ denotes the tensor structure tensor.

3.2.1 Biomechanical constitutive modeling of the gastrointestinal tissues

The mechanical behavior of gastrointestinal tissues plays a fundamental role in the function of the digestive system, both in healthy and pathological conditions. This behavior is typically described using *biomechanical constitutive models*, which are mathematical formulations that represent the relationship between stress and strain in biological tissues (Holzapfel, 2002). The availability of validated constitutive models is therefore essential for characterizing, simulating, and understanding the mechanics of the gastrointestinal tract.

In the literature, a systematic review of these constitutive models was conducted by (Patel et al., 2022), focusing specifically on *strain energy functions* used to describe the stress-strain relationship in gastrointestinal tissues. This review categorizes different modeling approaches based on how the tissue structure is incorporated:

- **Phenomenological models**: These models reproduce the overall

mechanical behavior without explicitly accounting for the underlying microstructural features of the tissue.

- **Structure-based models**: These models incorporate the average orientation of fibers and their global mechanical contribution within the strain energy function, but do not model individual fibers.

- **Microstructure-based models**: These approaches explicitly model the mechanical behavior of individual fibers and their orientation distribution, allowing for a more mechanistic representation.

Regarding structure-based models, a comparative study by (Puértolas et al., 2020) demonstrated that a hyperelastic model incorporating four fiber families more accurately captures the anisotropic behavior of gastrointestinal tissues compared to simpler formulations.

As the GI is a fiber-reinforced tissue embedded in a matrix (see Figure. 12), a combination of a phenomenological (isotropic) model and a structure-based constitutive formulation (anisotropic) is considered in this thesis. We proceed with an additive decomposition of the elastic strain energy density into isotropic and anisotropic contributions:

$$\Psi = \Psi^{\text{iso}} + \Psi^{\text{aniso}}, \tag{3.1}$$

where the isotropic term is associated with the passive mechanical response of the non-collagenous components of the tissue, primarily the elastin matrix (Puértolas et al., 2020; Sokolis, 2021). For the sake of clarity and without loss of generality (alternative models yield similar results (Nagaraja et al., 2021)), we adopt the Neo-Hookean material model:

$$\Psi^{\text{iso}} = \mu(I_1 - 3), \tag{3.2}$$

where μ denotes the passive isotropic stiffness.

The anisotropic strain energy component generally includes both passive and active contributions (see the next section). The passive contribution models the mechanical response of directional collagen fibers. These fibers, denoted by d_1 and d_2, represent the reinforcement provided by

the submucosa and are assumed to be symmetrically oriented at an angle θ with respect to the circumferential axis (see Fig. 12). The active anisotropic contribution originates from the smooth muscle cell (SMC) fibers aligned along the longitudinal (l) and circumferential (c) directions. The complete anisotropic energy is expressed as:

$$\begin{aligned}\Psi^{\text{aniso}} &= \Psi_{\text{p}}^{\text{aniso}} + \Psi_{\text{act}}^{\text{aniso}} \\ &= \sum_{i\in\{d_1,d_2\}} \frac{k_1^i}{4k_2^i}\left[\exp\left(k_2^i(I_4^i-1)_+^2\right)-1\right] \\ &+ \sum_{i\in\{l,c\}} \frac{k_1^i}{4k_2^i}\left[\exp\left(k_2^i(I_4^i-1)_+^2\right)-1\right].\end{aligned} \tag{3.3}$$

Here in Eq. 3.3, the notation $(y)_+ := \max(0, y)$ reproduces the tension-compression switch approximation (Patel et al., 2022). The anisotropic fourth invariant is defined as $I_4^j = \boldsymbol{C} : \boldsymbol{G}_j$ where $\boldsymbol{G}_j = \boldsymbol{n}_j \otimes \boldsymbol{n}_j$ for each fiber family $j \in \{l, c, d_1, d_2\}$.

The material parameters k_1^j (stiffness-like) and k_2^j (dimensionless) govern the directional mechanical behavior. Following previous studies (Puértolas et al., 2020; Sokolis, 2021; Nagaraja et al., 2021), the diagonal fiber families are assumed to share identical parameters.

In large deformation settings, the incompressibility of biological tissues is generally handled by a fully incompressible formulation ($J = 1$) or a nearly incompressible formulation ($J \simeq 1$). A recent study (Swati Sharma and Martin Lindsay Buist, 2025) on intestinal biomechanics showed that the fully incompressible case offers the best trade-off between precision and efficiency. Based on these findings, in this thesis, the fully incompressible approach to accurately model soft tissue mechanics is adopted. Then, the strain energy function can simply be written as:

$$\Psi = \mu(I_1 - 3) + \sum_{i\in\{l,c,d_1,d_2\}} \frac{k_1^i}{4k_2^i}[e^{k_2^i(I_4^i-1)_+^2} - 1] - p(J-1). \tag{3.4}$$

In Eq. 3.4, p stands for the solid hydrostatic pressure in the fully incompressibility approach. A preliminary calibration procedure was performed to estimate the material stiffnesses based on experimental data,

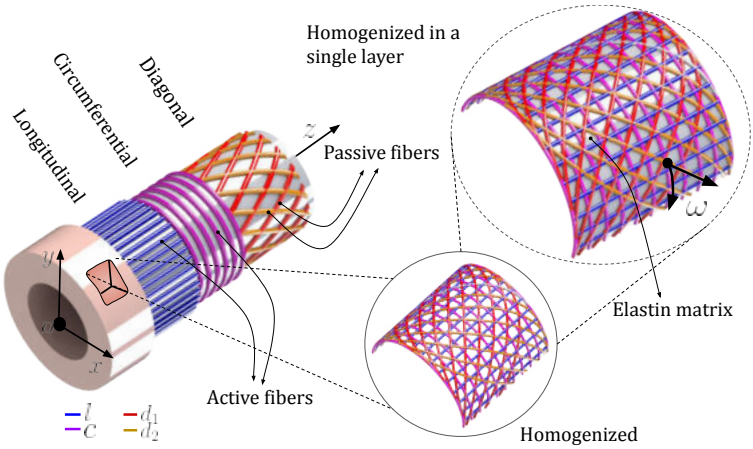

Figure 12: Schematic segment of the intestine. The zoomed cross-section represents the homogenized fiber microstructure, which is composed of four families of fibers embedded in an isotropic elastin matrix. The directions of the fibers are uniquely defined with respect to the circumferential direction by the angle ω; l represents the external longitudinal muscular layer, c the internal circumferential muscular fiber, d_1 and d_2 are the submucosa diagonal collagen fibers.

as discussed in Appendix. A. The final set of material parameters is provided in the table provided in the Appendix. A.

It is worth mentioning that from a numerical viewpoint, the precise creation of the fibrous structure of the GI tract is crucial. Due to their complex structure and strong layer adhesion, in this thesis a homogenized layer was chosen for fiber generation throughout the thickness of the wall. Similarly to the method presented in Piersanti et al. (2021), we developed and customized a rule-based algorithm (Rossi et al., 2014), originally proposed for cardiac fibers, to reproduce the microstructure of the gastrointestinal tract and generate muscle fibers throughout all simulations (a detailed explanation is provided in Appendix. B). We used this technique to generate longitudinal, circumferential, and helical fibers, allowing us to mimic the GI histology by assuming fibers spread through-

out the wall, as shown in Fig. 54. To be more precise in our modeling, we introduce a distinction between active families of fibers, namely circumferential and longitudinal, responsible for the activation of the contraction, and two additional passive diagonal ones necessary for the mechanics of the tissue.

3.3 Electromechanical coupling and strong form

3.3.1 Active model

Active models of gastrointestinal tissue are largely inspired by those developed for cardiac mechanics (Patel et al., 2022). Two main approaches are commonly employed to model active contraction: the **active stress** and **active strain** formulations. While the active stress approach has been widely used in gastrointestinal and intestinal modeling (Du, O'Grady, et al., 2010), it lacks a rigorous thermodynamic foundation. This limitation motivates the adoption of the active strain approach in this thesis.

The active strain formulation can be derived from thermodynamic principles (Alessio Gizzi et al., 2015), aligning with the framework of continuum mechanics and the notion of inelastic distortions. Moreover, the multiscale nature of smooth muscle cells (SMCs) where calcium and voltage-driven filament sliding (actin and myosin) occurs at microscopic scales justifies modeling their macroscopic contractile effect through a local distortion. Accordingly, we represent active smooth muscle contraction as a change in the local stress-free configuration of tissue elements, capturing the cumulative mechanical effect at the continuum level.

Then according to the active strain approach (Brandstaeter et al., 2018; Cherubini et al., 2008; Ambrosi et al., 2011; Ruiz-Baier et al., 2020), a multiplicative decomposition of the deformation gradient tensor into an elastic, $\boldsymbol{F}_e$, and an inelastic, $\boldsymbol{F}_a$ (see Fig. 13), part is put forward:

$$\boldsymbol{F} = \boldsymbol{F}_e \boldsymbol{F}_a \,. \tag{3.5}$$

Such an approach allows to apply multiscale and multiphysics couplings in a homogenised continuum framework over the local active deformation map.

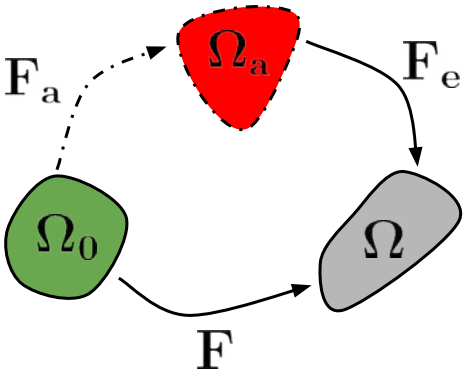

Figure 13: Multiplicative decomposition of deformation gradient $\boldsymbol{F}$ into active tensor $\boldsymbol{F}_a$ and elastic tensor $\boldsymbol{F}_e$.

Stemming from the gastric microstructural approach detailed in (Brandstaeter et al., 2018), and according to the active strain kinematics, we consider longitudinal and circumferential SMC directions as contractile units ruled by the active part of the deformation gradient:

$$\boldsymbol{F}_a = \boldsymbol{I} - \gamma(u_s)(\alpha_c \boldsymbol{n}_c \otimes \boldsymbol{n}_c + \alpha_l \boldsymbol{n}_l \otimes \boldsymbol{n}_l) + \gamma_n \boldsymbol{n}_n \otimes \boldsymbol{n}_n \,, \tag{3.6}$$

where $\boldsymbol{n}_c$, and $\boldsymbol{n}_l$ are the orthonormal unit vectors in the circumferential and longitudinal direction, respectively, while $\boldsymbol{n}_n = \boldsymbol{n}_c \times \boldsymbol{n}_l$ represents the unit vector orthogonal to their plane. In Eq. (3.6), α_c and α_l stand for material parameters ruling the amount of contraction in a certain direction, while γ_n enforces the incompressibility constraint in such a way that $\det(\boldsymbol{F}_a) = 1$, i.e.:

$$\gamma_n = \frac{1 - (1 - \gamma\alpha_c)(1 - \gamma\alpha_l)}{(1 - \gamma\alpha_c)(1 - \gamma\alpha_l)} \,. \tag{3.7}$$

The excitation function $\gamma(V)$ couples the mechanical problem with the electrophysiological one via a smooth activation function, defined in (Patel et al., 2022), dependent on the active membrane potential V crossing the smooth muscle layer:

$$\gamma(V) = (1 - e^{1-\beta_1(V-V_{th})})(1 - e^{1-\beta_2(V-V_{th})})H(V - V_{th}), \tag{3.8}$$

where, β_1, β_2, and V_{th} are the material parameters linked to the intracellular Ca^{2+} dynamics, while $H(V - V_{th})$ is a Heaviside step function switching on active contraction whenever the threshold V_{th} is reached. Parameters of $\gamma(V)$ and $\boldsymbol{F}_a$ can be found in Table 2.

Table 2: Material parameters of the active strain model (Brandstaeter et al., 2018).

α_c	α_l	β_1	β_2	V_{th}
0.2	0.2	10	10	$50\%V$

According to our electrophysiology model and since the SMCs are responsible for the activation of the mechanical contraction, Eq. (3.8) becomes:

$$\gamma(u_s) = (1 - e^{1-\beta_1(u_s - V_{th})})(1 - e^{1-\beta_2(u_s - V_{th})})H(u_s - V_{th}), \tag{3.9}$$

3.3.2 Strong form of mechanical counterpart

According to the given prescriptions in subsection 3.3.1, the first Piola-Kirchhoff stress tensor is derived under variational principles as:

$$\boldsymbol{P} = \frac{\partial \Psi}{\partial \boldsymbol{F}} - pJ\boldsymbol{F}^{-T} = \det(\boldsymbol{F}_a)\left(\frac{\partial \Psi^{\text{iso}}}{\partial \boldsymbol{F}_e} + \frac{\partial \Psi^{\text{aniso}}}{\partial \boldsymbol{F}_e}\right)\boldsymbol{F}_a^{-T} - pJ\boldsymbol{F}^{-T}, \tag{3.10}$$

where p stands for the solid hydrostatic pressure.

The strong form of the problem is given by the following set of nonlinear coupled partial differential equations prescribing mechanical equilibrium in terms of displacement field $\mathbf{u}$ and pressure p variables, defined in the undeformed GI domain Ω_0:

$$\nabla \cdot \boldsymbol{P} = \mathbf{0}, \quad \text{on} \quad \Omega_0 \times [0, T] \tag{3.11a}$$

$$J - 1 = 0, \quad \text{on} \quad \Omega_0 \times [0, T] \tag{3.11b}$$

complemented with electrophysiological balance laws Eq. (2.3), solved for the electrophysiological variables u_s, v_s, u_i, v_i.

Mixed boundary conditions of normal displacement and traction close the system:

$$\boldsymbol{u} \cdot \boldsymbol{n} = 0\,, \quad \text{on} \quad \Gamma_D \times [0,T] \tag{3.12a}$$

$$\boldsymbol{P}\boldsymbol{n} - p_0 J \boldsymbol{F}^{-T}\boldsymbol{n} = \boldsymbol{0}\,, \quad \text{on} \quad \Gamma_N \times [0,T] \tag{3.12b}$$

Γ_D and Γ_N are disjoint partition of the boundary. Condition Eq. (3.12a) constraints normal motion along the surface Γ_D. The term p_0 in Eq. (3.12b) denotes a prescribed (possibly time-dependent) boundary load (normal stress–pressure) associated with the presence of digesta within the lumen. In the present case, such a load is assumed uniform over the deformed counterpart of Γ_N, and applied in the normal direction to the internal surface of the GI in the deformed configuration.

In the previous sections, we presented the electromechanical model of the gastrointestinal (GI) system. When validating this model against experimental data, we observed pressure patterns in the experimental measurements that did not appear in the simulations. This raised several hypotheses: could these pressure zones be explained by the position of the intestine within the abdominal cavity, by self-contact of the intestine, or by interactions with neighboring organs?

To address these questions, we extended the model by incorporating contact mechanics and developing a dedicated boundary condition to account for the presence of surrounding organs. The details of this approach will be further discussed in the following sections.

3.4 Contact to the model and special boundary conditions

In this thesis, the general approach for imposing contact is shown in Figure. 14. Our objective is to prevent any interpenetration between the contact surfaces Γ_c that may occur during intestinal motility. To achieve this, we initially implemented a method based on the computation of the Euclidean distance between contact surfaces, using a contact search algorithm based on k-d-nearest neighbors (Hou et al., 2018; Kamaludin and

Thamburaja, 2023). While this approach proved to be effective, its implementation became increasingly challenging in cases involving multiple bodies or contact surfaces.

To overcome this limitation, we developed an alternative strategy based on the augmented Lagrange multiplier method. This enabled us to tackle more complex problems, thanks in particular to a contact-pair detection algorithm that relies on a ray-tracing technics (K. Poulios and Y. Renard, 2015).

In this context, we opted for unbiased contact formulations (i.e., without a master-slave distinction), which are particularly well-suited for handling complex scenarios such as self-contact and multi-body interactions, commonly encountered in gastrointestinal system modeling.

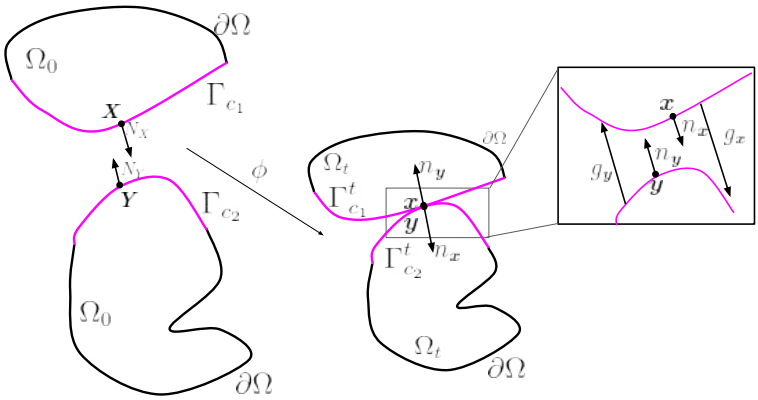

Figure 14: Concept of contact. $\boldsymbol{X}$ and $\boldsymbol{Y}$ are material points in the reference configuration, while $\boldsymbol{x}$ and $\boldsymbol{y}$ represent their positions in the current configuration. Γ_{c_i} and $\Gamma^t_{c_i}$ are the contact surfaces in the reference and current configurations, respectively. ϕ is the deformation map, $g_{\boldsymbol{x}}$ and $g_{\boldsymbol{y}}$ are the normal gaps.

Mathematically, the unilateral contact conditions on the surfaces are

given by the following Kuhn-Tucker conditions (Peter Wriggers, 2006):

$$g_x(\boldsymbol{n}_x) = \boldsymbol{u}_x \cdot \boldsymbol{n}_x \geq 0; \quad p_{\boldsymbol{n}_x} = (\boldsymbol{P}\boldsymbol{N}_x) \cdot \boldsymbol{n}_x \leq 0; \quad p_{\boldsymbol{n}_x} g_x(\boldsymbol{n}_x) = 0\,, \tag{3.13a}$$

$$g_y(\boldsymbol{n}_y) = \boldsymbol{u}_y \cdot \boldsymbol{n}_y \geq 0; \quad p_{\boldsymbol{n}_y} = (\boldsymbol{P}\boldsymbol{N}_y) \cdot \boldsymbol{n}_y \leq 0; \quad p_{\boldsymbol{n}_y} g_y(\boldsymbol{n}_y) = 0\,, \tag{3.13b}$$

where, $g_{\boldsymbol{x}}(\boldsymbol{n}_x)$, and $g_{\boldsymbol{y}}(\boldsymbol{n}_y)$ are the normal gaps between two generic points belonging respectively to Γ_{c1} and to Γ_{c2} potentially entering in contact, $p_{\boldsymbol{n}_x}$ and $p_{\boldsymbol{n}_y}$ are the normal contact traction aligned with the normals $\boldsymbol{n}_x$ and $\boldsymbol{n}_y$, respectively, and $\boldsymbol{P}$ is the first Piola-Kirchhoff stress tensor. Note that this approach can be esealy extend to multiples surfaces and bodies, Finally $\boldsymbol{u}_x$ and $\boldsymbol{u}_y$ are the relative displacements of the surfaces Γ_{c_1} and Γ_{c_2} respectively.

3.4.1 Contact search and contact pairs

In this subsection, we focus exclusively on the contact search algorithm based on the k-d-nearest neighbors method. For a detailed discussion on the ray-tracing approach, the reader is referred to (K. Poulios and Y. Renard, 2015).
Let Γ_{c_1} and Γ_{c_2} denote the two contact surfaces, both belonging to the deformable domain Ω_0. In the reference configuration, the nodal coordinates of these surfaces are extracted from the initial mesh. As the structure undergoes loading, the surfaces deform according to the nodal displacements obtained from solving the mechanical problem. To accurately track the evolution of the gap, the positions of the surface nodes must be continuously updated in the deformed configuration.

An illustrative schematic of the method is given in Figure. 15, and described as follows.

To evaluate the contact gap between points on the surfaces Γ_{c_1} and Γ_{c_2} in the *current configuration*, the nodes of Γ_{c_2} are first embedded in a hierarchical spatial partitioning structure, where each subdomain is recursively split along coordinate axes to form a binary tree. Each leaf node stores a small number of points from Γ_{c_2}. For any given node $\boldsymbol{x} \in \Gamma_{c_1}$, the algorithm descends the tree to locate the leaf that contains the spatial

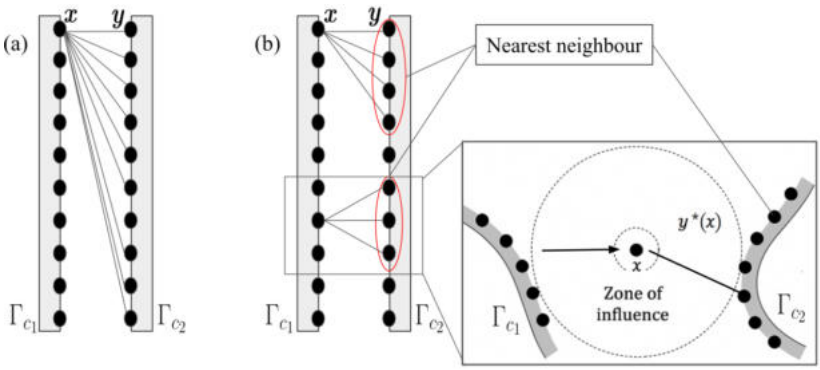

Figure 15: Concept of contact search based on the nearest neighbor algorithm: $\boldsymbol{x}$ and $\boldsymbol{y}$ represent points on the contact surfaces Γ_{c_1} and Γ_{c_2}, respectively, in the current configuration. Comparison of the method without (a) and with (b) the optimized search method incorporating the nearest neighbor algorithm: $\boldsymbol{y}^*(\boldsymbol{x})$ represents the closest point to $\boldsymbol{x}$ within the zone of influence.

region most likely to contain the closest neighbor to $\boldsymbol{x}$. At each branching point, we choose the child node whose bounding box is closest to $\boldsymbol{x}$, and we recursively evaluate the distance from $\boldsymbol{x}$ to each candidate point in the leaf. As the algorithm ascends back through the tree, it compares the minimum distance found so far with the distance from $\boldsymbol{x}$ to the other subtree's bounding region. If the latter may contain a closer point, it is also explored; otherwise, it is safely discarded. To ensure physical relevance, the search is restricted to a local *zone of influence* around each point $\boldsymbol{x}$. This zone is defined by the condition $\|\boldsymbol{x} - \boldsymbol{y}\| \leq \alpha_{\text{loc}} \cdot d_{\text{loc}}$, where d_{loc} is a local spacing metric and α_{loc} is a scaling factor controlling the extent of the influence region. This ensures that the closest point $\boldsymbol{y}^*(\boldsymbol{x}) \in \Gamma_{c_2}$ lies within a geometrically meaningful neighborhood of $\boldsymbol{x}$, allowing us to define the unsigned contact gap as:

$$g(\boldsymbol{x}) = \min_{\boldsymbol{y} \in \Gamma_{c_2}} \|\boldsymbol{x} - \boldsymbol{y}\|. \tag{3.14}$$

This result is guaranteed by the algorithm's exhaustive comparison against all subregions that could contain a closer point, ensuring that $\boldsymbol{y}^*(\boldsymbol{x})$ sat-

isfies the validity criterion

$$\|\boldsymbol{x} - \boldsymbol{y}^*(\boldsymbol{x})\| \leq \|\boldsymbol{x} - \boldsymbol{y}\|, \quad \forall \boldsymbol{y} \in \Gamma_{c_2}. \tag{3.15}$$

To include directional information, the gap is projected along a normalized direction $\boldsymbol{n}(x)$, which is computed as the normalized gradient of the scalar distance field, i.e., $\boldsymbol{n}_{\boldsymbol{x}} = \nabla g(\boldsymbol{x})/\|\nabla g(\boldsymbol{x})\|$, rather than using geometric normals, which may not be well defined or reliable under large deformations. This ensures that the final gap used in the Kuhn-Tucker conditions is a normal gap, as required, even though the intermediate search step relies on a Euclidean metric. The use of the distance-based normals rather than geometric surface normals is deliberate: under large deformations, geometric normals may become unreliable, especially when surfaces undergo folding or nearly parallel. The gradient-based normal provides a more stable and consistent direction for defining the projected gap.

The normal gap is then defined as:

$$g_{\boldsymbol{x}}(\boldsymbol{n}_x) = (\boldsymbol{y}^*(\boldsymbol{x}) - \boldsymbol{x}) \cdot \boldsymbol{n}(\boldsymbol{x}). \tag{3.16}$$

Eq.s 3.14-3.16 are used to compute the gap in Eq. 3.13, the same approach is used to compute the gap $g_{\boldsymbol{y}}(\boldsymbol{n}_y)$.

The contact search algorithm base on k-d tree nearest neighbour is described in Algorithm 1.

Algorithm 1 Nearest Neighbor Search Using KD-Tree

Require: A set of points $\Gamma_{c_2} = \{\boldsymbol{y}_1, \boldsymbol{y}_2, \ldots, \boldsymbol{y}_M\}$, a set of query points $\Gamma_{c_1} = \{\boldsymbol{x}_1, \boldsymbol{x}_2, \ldots, \boldsymbol{x}_N\}$.
Ensure: The minimum distance $g(\boldsymbol{x})$ for each $\boldsymbol{x} \in \Gamma_{c_1}$.
Step 1: Build the k-d tree
Construct a k-d tree for the points in Γ_{c_2}. ▷ This organizes the points of Γ_{c_2} into a space-partitioning tree.
Step 2: Initialize Results
Create an empty array $\mathcal{G}$ to store the gap $g(\boldsymbol{x})$ for each $\boldsymbol{x} \in \Gamma_{c_1}$.
Step 3: Perform Nearest Neighbor Search
for each point $\boldsymbol{x} \in \Gamma_{c_1}$ **do**
    Query the k-d tree to find the nearest neighbor $\boldsymbol{y} \in \Gamma_{c_2}$ to $\boldsymbol{x}$.
    Compute the Euclidean distance: $g(\boldsymbol{x})$
    Store $g(\boldsymbol{x})$ in $\mathcal{G}$.
end for
Step 4: Return Results
return $\mathcal{G}$, the array of minimum distances.

3.4.2 Penalty and Augmented Lagrangian approaches to contact

Penalty approach

One of the simplest ways to automatically ensure the satisfaction of contact inequalities (Eqs. 3.13) to a given tolerance consists of imposing the following penalized condition:

$$p_{\boldsymbol{n}_x} = -K_0\langle \mathrm{tol} - g_{\boldsymbol{x}}(\boldsymbol{n}_x)\rangle; \quad p_{\boldsymbol{n}_y} = -K_0\langle \mathrm{tol} - g_{\boldsymbol{y}}(\boldsymbol{n}_y)\rangle\,, \tag{3.17}$$

where $\langle \mathcal{J} \rangle = (\mid \mathcal{J} \mid + \mathcal{J})/2$ is the Mackauley operator computing the positive part of the gaps with K_0 a large stiffness penalty value and tol is a small tolerance used to control the activation contact to avoid small penetration which is the weakness of the penalty method. The contact forces are then computed as

$$\mathbf{p}_{N_x} = p_{\boldsymbol{n}_x}\boldsymbol{n}_x\,,\ \mathbf{p}_{N_y} = p_{\boldsymbol{n}_y}\boldsymbol{n}_y. \tag{3.18}$$

Augmented Lagrangian approach

The non-penetration condition $g(X) \geq 0$ is imposed through a Lagrange multiplier $\lambda_N(\boldsymbol{X}) \leq 0$ where $\lambda_N : \Gamma^M \to \mathbb{R}$, representing the normal contact traction (in the reference configuration).

To avoid handling inequality constraints explicitly, the problem is reformulated using an augmented lagrangian functional:

$$\mathcal{L}_r(\boldsymbol{u}, \lambda_{\boldsymbol{N}}) = P(\boldsymbol{u}) + \frac{1}{2r} \int_{\Gamma_c^S} [\lambda_N + rg]_-^2 - \lambda_N^2 \, d\Gamma, \tag{3.19}$$

in Eq. 3.19 $P(\boldsymbol{u})$ is the total potential energy (including internal elastic energy and external loading), $r > 0$ is the augmentation parameter, and $[a]_- = \min(x, 0)$ denotes the negative part of a. The set $\Gamma_c^S \subset \Gamma^S$ identifies the slave surface region where contact is detected or expected.

The first-order optimality conditions of this augmented functional yield the following weak form:

$$\begin{aligned} &\mathcal{D}J(\varphi)[\delta\boldsymbol{u}] - \int_{\Gamma_c^S} \lambda_{\boldsymbol{N}} \, \boldsymbol{n_x} \cdot (\delta\boldsymbol{u}(\boldsymbol{X}) - \delta\boldsymbol{u}(\boldsymbol{Y})) \, d\Gamma = 0 \quad \forall \, \delta\boldsymbol{u}, \\ &- \frac{1}{r} \int_{\Gamma_c^S} \left(\lambda_{\boldsymbol{N}} + [\lambda_{\boldsymbol{N}} + rg]_- \right) \delta\lambda_{\boldsymbol{N}} \, d\Gamma = 0 \quad \forall \, \delta\lambda_{\boldsymbol{N}}. \end{aligned} \tag{3.20}$$

in Eq. 3.20 $\mathcal{D}P(\boldsymbol{u})[\delta\boldsymbol{u}]$ is the directional derivative of the potential energy with respect to a virtual displacement $\delta\boldsymbol{u}$, and $\delta\lambda_{\boldsymbol{N}}$ is a virtual variation of the contact multiplier field.

This formulation possesses several advantages: it avoids explicit inequality constraints on $\lambda_{\boldsymbol{N}}$; it remains differentiable almost everywhere, which enables the use of a generalized Newton method; and it involves only the slave surface normal $\boldsymbol{n_x}$, which is differentiable and easier to compute numerically than the master surface normal.

Moreover, the weak enforcement of contact conditions through surface integrals at quadrature points makes the method robust and suitable for standard finite element discretizations, without requiring nodal enforcement or special projection schemes. Another notable advantage of this method lies in its natural ability to handle self-contact scenarios.

Indeed, the use of a ray-tracing strategy allows contact detection to be performed symmetrically, without requiring a fixed distinction between slave and master surfaces. In the case of self-contact, the same physical surface can serve both roles.

Practically, this means that the ray-tracing search can be performed from a given surface point using its outward normal, and the corresponding intersection can be detected on the same surface. This results in a so-called master–master contact strategy, which avoids the need to define separate meshes or projection directions, as typically required in standard slave–master approaches. Consequently, the method can robustly capture self-contact, even under large deformations and complex contact topologies.

3.5 Weak formulations

All problems were resolved using a hybrid numerical scheme that combines staggered and monolithic approaches. The electrophysiology problem was solved using a monolithic scheme with mixed finite element spaces. Subsequently, the electrophysiology model was coupled to the mechanical problem using a staggered scheme.

3.5.1 Electrophysiological problem

The weak form of the electrophysiology problem can be written as it follows: at each time step $t^{n+1} = t^n + \Delta t$ of an equispaced partition of the time interval $[0, T]$, given the solution of the electrophysiology problem at the previous timestep $(u_s^n, v_s^n, u_i^n, v_i^n) \in V^4$ find the vector $(u_s^{n+1}, v_s^{n+1}, u_i^{n+1}, v_i^{n+1}) \in V^4$ at the current timestep t^{n+1} such that it is

satisfied

$$\int_{\Omega_0} \frac{u_s^{n+1} - u_s^n}{\Delta t} \delta u_s + \int_{\Omega_0} D_s \nabla u_s^{n+1} \cdot \nabla \delta u_s = \int_{\Omega_0} I_{ion}^s(u_s^n, v_s^n, u_i^n) \delta u_s \,, \tag{3.21a}$$

$$\int_{\Omega_0} \frac{v_s^{n+1} - v_s^n}{\Delta t} \delta v_s = \int_{\Omega_0} R_s(u_s^n, v_s^n) \delta v_s \,, \tag{3.21b}$$

$$\int_{\Omega_0} \frac{u_i^{n+1} - u_i^n}{\Delta t} \delta u_i + \int_{\Omega_0} D_i \nabla u_i^{n+1} \cdot \nabla \delta u_i = \int_{\Omega_0} I_{ion}^i(u_s^n, v_i^n, u_i^n) \delta u_i \,, \tag{3.21c}$$

$$\int_{\Omega_0} \frac{v_i^{n+1} - v_i^n}{\Delta t} \delta v_i = \int_{\Omega_0} R_i(u_i^n, v_i^n) \delta v_i \,, \tag{3.21d}$$

for all test functions $(\delta u_s, \delta v_s, \delta u_i, \delta v_i) \in (V_0)^4$, where:

$$I_{ion}^i(u_s, v_i, u_i) = g(u_i) - v_i + F_i(u_s, u_i) + I_{stim}^i \,, \tag{3.22a}$$

$$R_i(u_i, v_i) = \epsilon_i(z)[\lambda_i(u_i - \beta_i) - v_i] \,, \tag{3.22b}$$

$$I_{ion}^s(u_s, v_s, u_i) = f(u_s) - v_i + F_s(u_s, u_i) + I_{stim}^s \,, \tag{3.22c}$$

$$R_s(u_s, v_s) = \epsilon_s[\lambda_i(u_s - \beta_s) - v_s] \,. \tag{3.22d}$$

The implicit Euler scheme for the discretization of the time derivative has been adopted in Eqs. (3.21), while an explicit treatment of the reaction terms has been used. In a more compact notation, the electrophysiology problem can be written as: find u_s, u_i, v_s and v_i such that

$$\mathcal{E}(u_s, u_i, v_s, v_i; \delta u_s, \delta u_i, \delta v_s, \delta v_i) := \mathcal{E}_1 + \mathcal{E}_2 + \mathcal{E}_3 + \mathcal{E}_4 = 0 \,, \tag{3.23}$$

for all test functions $\delta u_s, \delta u_i, \delta v_s, \delta v_i$, where:

$$\mathcal{E}_1 = \mathcal{E}_1(u_s, u_i, v_s; \delta u_s, \delta u_i, \delta v_s) \,, \tag{3.24a}$$

$$\mathcal{E}_2 = \mathcal{E}_2(u_s, v_s; \delta u_s, \delta v_s) \,, \tag{3.24b}$$

$$\mathcal{E}_3 = \mathcal{E}_3(u_s, u_i, v_i; \delta u_s, \delta u_i, \delta v_i) \,, \tag{3.24c}$$

$$\mathcal{E}_4 = \mathcal{E}_4(u_i, v_i; \delta u_i, \delta v_i) \,, \tag{3.24d}$$

are respectively the residuals of Eqs. (3.21).

3.5.2 Mechanical problem

The trial spaces, where the solution of the weak form of the problem is defined, are given by:

$$\boldsymbol{u} \in \mathbf{V} := L^2(0,T;\mathbf{H}^1(\Omega_0)),\ p \in Q := L^2(0,T;L^2(\Omega_0)), \tag{3.25}$$

for displacements and pressure
The virtual displacements for the mechanical problem are introduced as $\delta\boldsymbol{u} \in \mathbf{V}_0$, as well as the test functions for the pressure $\delta p \in Q_0$ defined on the spaces of the corresponding fields, and vanishing on the Dirichlet part of the boundary. Multiplying Eq. (3.11) by a virtual displacement, using the divergence theorem, the generic weak form of the mechanical problem without contact is:
find displacement $\boldsymbol{u} \in \mathbf{V}$ and pressure $p \in Q$ such that

$$\int_{\Omega_0} \boldsymbol{P} : \nabla\delta\boldsymbol{u} - \int_{\Gamma_N} p_0(t) J\boldsymbol{F}^{-T}\boldsymbol{n}\cdot\delta\boldsymbol{u} = 0,\ \forall\delta\boldsymbol{u} \in \mathbf{V}_0\,, \tag{3.26a}$$

$$\int_{\Omega_0} (J-1)\delta p\ \mathrm{d}V + \int_{\Omega_0} \zeta_{stab}\nabla p\cdot\nabla\delta p = 0,\ \forall\delta p\ \mathrm{d}V \in Q_0\,, \tag{3.26b}$$

where ζ_{stab} is a positive pressure stabilization parameter used as a locking-free parameter to enhance the stability of the discrete problem Chavan, Lamichhane, and Wohlmuth, 2007. The mechanical problem without contact can be rewritten in a more compact form as:
find displacement and pressure $\boldsymbol{u}$ and p such that

$$\begin{aligned}\mathcal{M}(\boldsymbol{u},p;\delta\boldsymbol{u},\delta p) := &\int_{\Omega_0} \boldsymbol{P} : \nabla\delta\boldsymbol{u}\ \mathrm{d}V - \int_{\Gamma_N} p_0(t) J\boldsymbol{F}^{-T}\boldsymbol{N}\cdot\delta\boldsymbol{u}\ \mathrm{d}\Gamma \\ &+ \int_{\Omega_0} (J-1)\delta p\ \mathrm{d}V + \int_{\Omega_0} \zeta_{stab}\nabla p\cdot\nabla\delta p\ \mathrm{d}V,\end{aligned} \tag{3.27}$$

for all test functions $\delta\boldsymbol{u}$ and δp.
Following the same procedure, the mechanical problem with the contact

with penalty method reads as:

$$\begin{aligned}\mathcal{M}(\boldsymbol{u},p;\delta\boldsymbol{u},\delta p) := &\int_{\Omega_0} \boldsymbol{P} : \nabla\delta\boldsymbol{u}\ \mathrm{d}V - \int_{\Gamma_N} p_0(t) J\boldsymbol{F}^{-T}\boldsymbol{N}\cdot\delta\boldsymbol{u}\ \mathrm{d}\Gamma \\ &+ \int_{\Omega_0} (J-1)\delta p\ \mathrm{d}V + \int_{\Omega_0} \zeta_{stab}\nabla p\cdot\nabla\delta p\ \mathrm{d}V \\ &+ \int_{\Gamma} J\,\boldsymbol{R}_{\mathrm{rob}}\cdot\boldsymbol{F}^{-T}\boldsymbol{u}\cdot\delta\boldsymbol{u}\ \mathrm{d}\Gamma \\ &+ \int_{\Gamma_{c_1}} K_0\langle \mathrm{tol} - g_{c_1}\rangle \boldsymbol{n}_{c_1}\cdot\delta\boldsymbol{u}\ \mathrm{d}\Gamma \\ &+ \int_{\Gamma_{c_2}} K_0\langle \mathrm{tol} - g_{c_2}\rangle \boldsymbol{n}_{c_2}\cdot\delta\boldsymbol{u}\ \mathrm{d}\Gamma = 0,\end{aligned} \tag{3.28}$$

for all test functions $\delta\boldsymbol{u}$ and δp.

$$\begin{aligned}\mathcal{M}(\boldsymbol{u},p,\lambda_{\boldsymbol{N}};\delta\boldsymbol{u},\delta p,\delta\lambda_{\boldsymbol{N}}) := &\int_{\Omega_0} \boldsymbol{P} : \nabla\delta\boldsymbol{u}\ \mathrm{d}V - \int_{\Gamma_N} p_0(t) J\boldsymbol{F}^{-T}\boldsymbol{N}\cdot\delta\boldsymbol{u}\ \mathrm{d}\Gamma \\ &- \sum_{i=1}^{nc}\int_{\Gamma_c^i} \lambda_{\boldsymbol{N}}^i\,\boldsymbol{n}_{\boldsymbol{x}}\cdot(\delta\boldsymbol{u}(\boldsymbol{X}) - \delta\boldsymbol{u}(\boldsymbol{Y}))\ \mathrm{d}\Gamma \\ &- \sum_{i=1}^{nc}\frac{1}{r}\int_{\Gamma_c^i}\left(\lambda_{\boldsymbol{N}}^i + \left[\lambda_{\boldsymbol{N}}^i + rg\right]_-\right)\delta\lambda_{\boldsymbol{N}}^i\ d\Gamma \\ &+ \int_{\Omega_0} (J-1)\delta p\ \mathrm{d}V + \int_{\Omega_0} \zeta_{stab}\nabla p\cdot\nabla\delta p\ \mathrm{d}V \\ &+ \int_{\Gamma} J\,\boldsymbol{R}_{\mathrm{rob}}\cdot\boldsymbol{F}^{-T}\boldsymbol{u}\cdot\delta\boldsymbol{u}\ \mathrm{d}\Gamma = 0,\end{aligned} \tag{3.29}$$

for all test functions $\delta\boldsymbol{u}$, $\delta\boldsymbol{u}_b$, δp and $\delta\lambda_{\boldsymbol{N}}^i$, nc is the number of contact surfaces and $\boldsymbol{R}_{\mathrm{rob}}$ stands for the Robin boundary condition that will be discussed in the chapter 6.

3.5.3 Finite element discretization

This subsection presents the finite element discretization applied to all the problems addressed in this thesis, as well as the numerical scheme adopted. We describe here the core of the numerical scheme used for

solving the various models. For the contact problems, a specific variant of this algorithm has been developed and will be presented in the Alg 3. The computational domain Ω_0 has been discretized into tetrahedral finite elements and the unknowns have been approximated using Lagrangian shape functions $\mathbb{P}_2$ and $\mathbb{P}_1$ for the all variational problems. Some problems has been implemented in the open-source finite element software `FEniCS` (Alnæs et al., 2015) while others in the open-source finite element software `GetFem` (Yves Renard and Konstantinos Poulios, 2020). A staggered scheme was adopted to couple the mechanical problem and the electrophysiology problem. The monolithic scheme was adopted for each problem separately, the nonlinear mechanical problem is solved using the Newton-Raphson method and, at each Newton's iteration, the resulting linear system given by $d\mathcal{M}(\Delta\boldsymbol{u}, \Delta p; \delta\boldsymbol{u}, \delta p) = -\mathcal{M}(\boldsymbol{u}_k^{n+1}, p_k^{n+1}; \delta\boldsymbol{u}, \delta p)$ for the corrections $\Delta\boldsymbol{u}$ and Δp is solved using a `MUMPS`. The tangent operator $d\mathcal{M}$ associated to the nonlinear variational mechanical problem in Eq. (3.27) has been computed via the symbolic derivative `derivative`. For the solution of the electrophysiological problem, the `PETSc` library (Portable, Extensible Toolkit for Scientific Computing) has been used. The algorithm for the solution of the coupled electromechanical problem describing the GI motility is detailed in Alg. 2.

Algorithm 2 Algorithm for the electromechanical motility of a GI tract

Input Initial and boundary conditions for displacement, pressure and electrophysiological variables:
while $t^n < T$ **do**
    Given: displacement and pressure $\boldsymbol{u}^n, p^n$ solve the linear electrophysiology problem: $\mathcal{E}(u_s^{n+1}, u_i^{n+1}, v_s^{n+1}, v_i^{n+1}; \delta u_s, \delta u_i, \delta v_s, \delta v_i) = 0$
    Update EP solutions $(u_s^n, u_i^n, v_s^n, v_i^n) \leftarrow (u_s^{n+1}, u_i^{n+1}, v_s^{n+1}, v_i^{n+1})$
    Given: the electrophysiological variables $(u_s^{n+1}, u_i^{n+1}, v_s^{n+1}, v_i^{n+1})$, solve the mechanical problem via Newton-Raphson procedure:
    for a given Newton iteration k **do**
        Given: $\boldsymbol{u}_k^{n+1}$ and p_k^{n+1} solve the linearized mechanical problem: $d\mathcal{M}(\Delta\boldsymbol{u}, \Delta p; \delta\boldsymbol{u}, \delta p) = -\mathcal{M}(\boldsymbol{u}_k^{n+1}, p_k^{n+1}; \delta\boldsymbol{u}, \delta p)$
        Set: $\boldsymbol{u}_{k+1}^{n+1} = \Delta\boldsymbol{u} + \boldsymbol{u}_k^{n+1}$ and $p_{k+1}^{n+1} = \Delta p + p_k^{n+1}$
        if $\|\boldsymbol{u}_{k+1}^{n+1} - \boldsymbol{u}_k^{n+1}\| < tol$ **then**
            Update the Newton solutions $\boldsymbol{u}_k^{n+1} \leftarrow \boldsymbol{u}_{k+1}^{n+1}$ and $p_k^{n+1} \leftarrow p_{k+1}^{n+1}$
        else $k \leftarrow k + 1$
        end if
        Update mechanical solutions $\boldsymbol{u}^{n+1} \leftarrow \boldsymbol{u}_{k+1}^{n+1}$ and $p^{n+1} \leftarrow p_{k+1}^{n+1}$
    end for
    Update time: $t \leftarrow t + \Delta t$
    Output: Displacement $\boldsymbol{u}^{n+1}$, pressure p^{n+1} and electrophysiological variables $(u_s^{n+1}, v_s^{n+1}, u_i^{n+1}, v_i^{n+1})$ at the current time t^{n+1}
end while

Algorithm 3 Algorithm for the electromechanical motility with self-contact

Input Initial and boundary conditions for displacement, pressure and electrophysiological variables:
while $t^n < T$ **do**
  Given: displacement and pressure $\boldsymbol{u}^n, p^n$ solve the linear electrophysiology problem: $\mathcal{E}(u_s^{n+1}, u_i^{n+1}, v_s^{n+1}, v_i^{n+1}; \delta u_s, \delta u_i, \delta v_s, \delta v_i) = 0$
  Update EP solutions $(u_s^n, u_i^n, v_s^n, v_i^n) \leftarrow (u_s^{n+1}, u_i^{n+1}, v_s^{n+1}, v_i^{n+1})$
  Given: the electrophysiological variables $(u_s^{n+1}, u_i^{n+1}, v_s^{n+1}, v_i^{n+1})$, solve the mechanical self-contact problem.
  Contact detection: Run Algorithm. 1
  if Eq. 3.13 **then** activate contact force
  else Pass
  end if
  Newton-Raphson procedure:
  for a given Newton iteration k **do**
    Given: $\boldsymbol{u}_k^{n+1}$ and p_k^{n+1} solve the linearized mechanical problem: $d\mathcal{M}(\Delta\boldsymbol{u}, \Delta p; \delta\boldsymbol{u}, \delta p) = -\mathcal{M}(\boldsymbol{u}_k^{n+1}, p_k^{n+1}; \delta\boldsymbol{u}, \delta p)$
    Set: $\boldsymbol{u}_{k+1}^{n+1} = \Delta\boldsymbol{u} + \boldsymbol{u}_k^{n+1}$ and $p_{k+1}^{n+1} = \Delta p + p_k^{n+1}$
    if $\|\boldsymbol{u}_{k+1}^{n+1} - \boldsymbol{u}_k^{n+1}\| < tol$ **then**
      Update the Newton solutions $\boldsymbol{u}_k^{n+1} \leftarrow \boldsymbol{u}_{k+1}^{n+1}$ and $p_k^{n+1} \leftarrow p_{k+1}^{n+1}$
    else $k \leftarrow k + 1$
    end if
    Update mechanical solutions $\boldsymbol{u}^{n+1} \leftarrow \boldsymbol{u}_{k+1}^{n+1}$ and $p^{n+1} \leftarrow p_{k+1}^{n+1}$
  end for
  Update time: $t \leftarrow t + \Delta t$
  Output: Displacement $\boldsymbol{u}^{n+1}$, pressure p^{n+1} and electrophysiological variables $(u_s^{n+1}, v_s^{n+1}, u_i^{n+1}, v_i^{n+1})$ at the current time t^{n+1}
end while

3.6 Conclusion

In this chapter, we developed the electromechanical model of the intestinal tissue, incorporating the effects of self-contact. In addition, an alternative contact formulation was proposed to investigate the interaction between the intestine and external bodies, allowing the reproduction of specific clinical procedures. The mechanical model was validated through uniaxial and triaxial tests, in which a parameter identification algorithm was employed to estimate the constitutive parameters of the tissue.

A finite element discretization was then derived for the numerical resolution, and dedicated algorithms were implemented for both the electromechanical coupling and the electromechanical problem with contact. In the next chapter, we will introduce a complete workflow for applying this model to patient-specific geometries, along with the computational tools required for its implementation.

Chapter 4

Integrating patient specific and experimental data into the model

4.1 Introduction

To make numerical simulations reliable and truly useful, even for healthcare professionals, the developed computational models must be able to integrate and assimilate real clinical data. Such data may come in various forms, including anatomical geometries, physiological measurements (such as pressure or electrical potentials), or experimental observations. However, incorporating these data into numerical models remains a significant challenge.

The objective of this chapter is to describe, step by step, a methodology for transforming geometries obtained from CT-scan or MRI images into models suitable for finite element simulations. We also present the software tools used throughout the process. In addition, we explain the experimental procedures we carried out to acquire in vivo data on porcine models.

We first describe the acquisition and segmentation of imaging data, along with the file formats generated. Then, we demonstrate how these

files can be processed to become compatible with finite element analysis. We further illustrate how such models can be employed to generate intestinal muscle fiber orientations. Finally, we detail the experimental procedures and explain how physicians perform high-resolution manometry an essential measurement for assessing intestinal motility in patients.

4.2 Preparing patient-specific geometry for finite element simulation

4.2.1 Image segmentation

In the literature, several software tools are available for segmentation and extraction of geometries suitable for numerical modeling. Among the most widely used are Materialize, ITK-SNAP, MITK, and others. In this work, we selected 3D Slicer which is open-source, well-documented, and relatively easy to use. 3D Slicer is a software application designed for the visualization and analysis of medical imaging datasets (Fedorov et al., 2012). It supports a wide range of commonly used data types, including images, segmentations, surfaces, annotations, and transformations, in 2D, 3D, and 4D. Visualization can be performed both on a desktop workstation and in virtual reality environments. The software also provides a comprehensive set of analysis tools, including image segmentation, image registration, and various quantitative analyses.

The data most commonly used with 3D Slicer are stored in the DICOM format (Digital Imaging and Communications in Medicine) (Mildenberger, Eichelberg, and Martin, 2002), a technical standard for the digital storage and transmission of medical images and related information. These datasets are typically acquired in three anatomical planes: axial, coronal, and sagittal, represented respectively by the red, green, and yellow views, and finally the 3D view as shown in Figure. 16.

Once the data have been imported, several filters and tools can be applied to segment the tissues and isolate the regions of interest (ROI) needed for geometric reconstruction. For more information on the segmentation methods and available options, readers are encouraged to con-

sult the official 3D Slicer documentation. Specifically, the procedure involved a mixture of manual contour refinement, threshold-based filtering, and region-growing operations, depending on the anatomical region and the quality of the available images. No deep-learning or machine-learning techniques were used. Instead, segmentation was performed through classical semi-automatic tools complemented by manual corrections to ensure anatomical coherence.

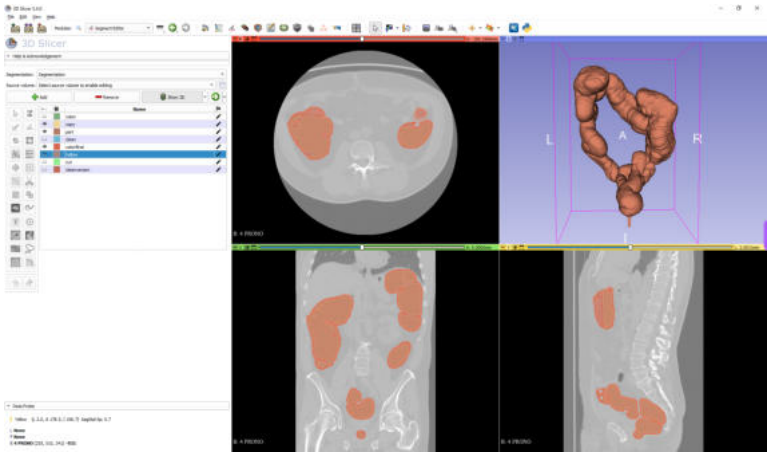

Figure 16: 3D geometry of the colon obtained from a CT-scan. Axial, coronal, and sagittal directions are represented respectively by the red, green, and yellow windows, and the last window is a 3D view.

In it important to note that he colon CT dataset was the only raw clinical imaging dataset available to us for demonstrating the segmentation workflow in 3D Slicer; however, its quality was insufficient for use in the subsequent steps of the chapter.

4.2.2 Obtaining 3D mesh for simulation

For simplicity in this demonstration, we used a simplified duodenum geometry obtained from a male cryosection of the Visible Human Project (VHP) (Ackerman, 2002). Once segmented in 3D Slicer, the geometry is typically exported in STL (STereoLithography) format, which represents

only the surface without thickness, as shown in Figure. 17a. However, the resulting mesh is usually of poor quality, requiring post-processing before it can be used for numerical simulations.

Several commercial and open-source tools are available for cleaning and preparing STL geometries. In this work, we used Meshmixer (Schmidt and Singh, 2010), Autodesk's free and lightweight toolbox for mesh editing and 3D printing preparation. Positioned between heavy CAD suites and digital sculpting tools, Meshmixer has become an essential software for quickly repairing, merging, and preparing polygonal models.

Using Meshmixer, we performed several operations:

- cleaning the raw mesh,
- smoothing the surface to remove irregularities,
- cutting and removing undesired regions,
- adding a thickness to the surface, and
- reducing the mesh density to make it compliant and lighter.

After these operations, we also created surface groups to simplify the identification of regions of interest for subsequent processing. The resulting mesh after cleaning and refinement is shown in Figure. 17b.

As discussed in Chapter. 2, the excitability of the interstitial cells of Cajal (ICC) plays a crucial role in coordinating slow-wave propagation. This excitability, expressed as z, which represents the cumulative distance along the intestinal centerline.

To extract this centerline, we developed a custom script based on the VMTK (Vascular Modeling Toolkit) library. Successful extraction requires the geometry to be thin-walled and fully closed. The resulting centerline geometry is illustrated in Figure. 17c.

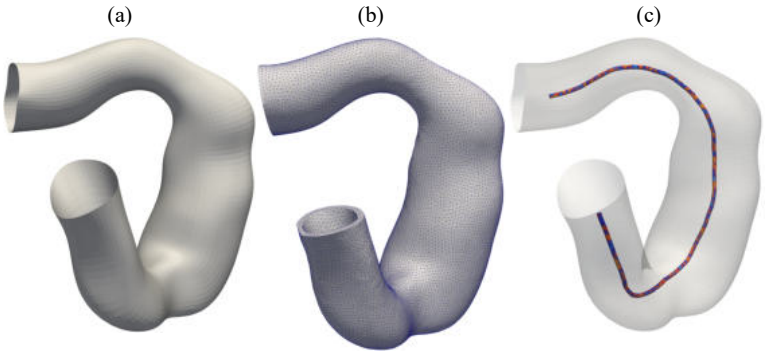

Figure 17: Different geometries obtained after each operation. (a) STL file from 3D slicer, (b) cleaned mesh obtained from Meshmixer and (c) centerline obtained from VMTK

4.2.3 Create boundary conditions and test case

It should be noted that even at this stage, although the mesh is clean and usable, it still cannot be used directly for finite element problems, as it remains a surface STL without volume. To add volume to a mesh, several commercial and open-source software tools are available. In this thesis, we mainly used two of them: Salome-meca (Drouet, 2017) and Gmsh (Geuzaine and Remacle, 2009). However, for this demonstration, we used Gmsh. Once the geometry is imported into Gmsh, a volume is generated from the STL surface.

It is important to mention that the STL file exported from Meshmixer must be encoded in ASCII format. This allows us to preserve all the groups previously defined or even modify them later in a text editor if necessary. This technique is particularly useful for labeling or tagging surfaces. After this step, the mesh can be exported in .msh format and used directly in open-source finite element codes such as `GetFem` (Yves Renard and Konstantinos Poulios, 2020), or converted into .xml format for use with `FEniCS` (Alnæs et al., 2015).

After obtaining the volumetric mesh and creating physical groups for boundary conditions, it was used to generate the muscle fiber orientations in the duodenum, which are essential for modeling tissue mechanics. The procedure follows the method described in Appendix. B . Briefly, this method involves solving Poisson's equations with specific Dirichlet boundary conditions, followed by computing fiber rotation using Rodrigues' rotation formula. The Dirichlet and Neumann conditions described in Appendix. B were used for the duodenum geometry, ensuring that the fiber generation procedure - remains fully consistent and reproducible within the standalone chapter.The results are shown in Figure. 18a–c, which present the longitudinal, circumferential, and diagonal fiber directions, respectively. This same procedure will be used in the following chapters to prepare the other geometries.

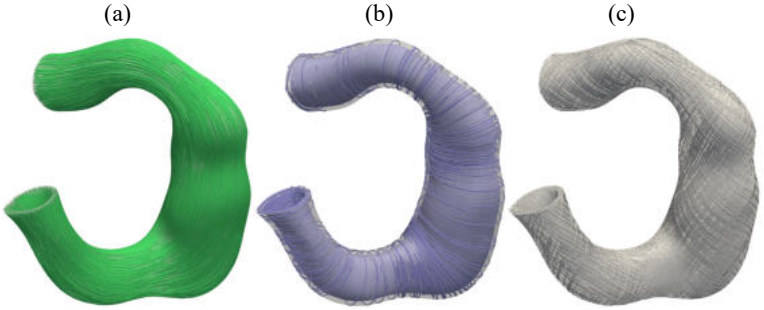

Figure 18: Fiber orientation in the duodenum. (a) Longitudinal fiber, (b) circumferential fiber and (d) diagonal fiber.

4.3 Experimental data collection and clinical observations

4.3.1 Experimental data collection

To ensure the reliability of the proposed models, a series of experiments were conducted in vivo on eight weaner male pigs with a weight of 41.7 ± 1.1 kg. These experiments were carried out at the University of Auckland, with ethical approval obtained from the University of Auckland Animal Ethics Committee (see Figure. 19a).

For the inflation test, the pigs were first anesthetized with isoflurane, after which a midline abdominal laparotomy was performed to access the abdominal cavity. A 20 cm segment of the jejunum was exteriorized, and a small incision was made at one end of this section to insert a balloon catheter (Mui Scientific, Toronto, Canada). The incision was then closed using suture thread to ensure a tight seal (see Figure. 19b). The barostat system was operated in pressure-control mode, maintaining the balloon pressure at a predefined set-point (mmHg). The system automatically adjusted the balloon volume to keep the luminal pressure constant. The barostat's analog output provided the balloon volume data, which were recorded on a computer. Throughout the experiment, changes in balloon volume were continuously monitored.

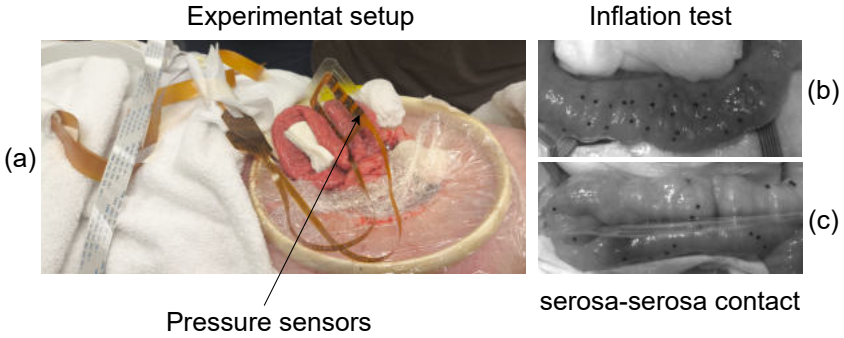

Figure 19: Experiment carried out at the University of Auckland, (a) shows the experimental setup used for the collection of the contact serosa-serosa contact pressure, (b) the inflation test used to collect the intraluminal volume change during the peristalsis, and (c) the serosa-serosa contact test used to collect the self-contact pressure during the peristalsis

For the external contact pressure, pressure sensors (for details on the pressure sensor and the calibration, see (Athavale, Paskaranandavadivel, et al., 2020)) were placed on the serosal surface of the intestine to measure contact pressures, including those arising from serosa–serosa self-contact and from the intestinal wall in general. For this experiment, a pressure sensor was placed between the outer surfaces of the intestine, which was arranged in a U- or C-shaped configuration, as shown in Figure 19c. The pressure sensor had eight channels, designed to record contact pressures between the serosal surfaces during intestinal motion. Unfortunately, despite the experimental protocol adopted, it was extremely difficult to obtain reliable data from all channels. In practice, only two channels provided usable pressure measurements. The pressures recorded from these two channels, shown in Figure. 20, illustrate how the data exhibited significant variability but still followed a consistent overall trend. This experimental protocol was used to collect not only contact pressure data between the serosal layers and volume variations from the barostat system, but also electrical activity recordings, which, however, were not used in this thesis.

It is important to note that these tests were conducted in vivo, which

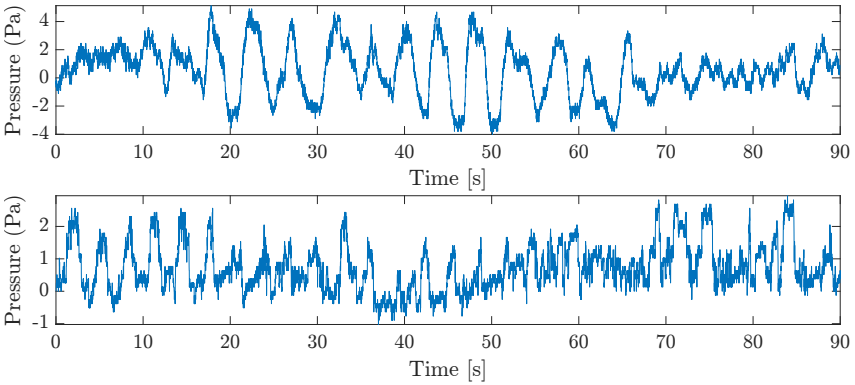

Figure 20: Experimental pressure collected from two channels.

made it extremely difficult to maintain the same intestinal position during each experiment. This variability made the interpretation of the experimental data particularly challenging.

The main difficulty came from the fact that the intestine is surrounded by an amniotic-like fluid, which caused it to slide continuously, making it hard to stabilize. Moreover, performing the procedure in vivo limited the accessibility and manipulability of the intestinal tissue, further complicating the experimental setup and data acquisition.

4.3.2 Geometry reconstruction during in vivo test

During this experiment, in addition to the numerical data collected, 3D images of the intestine in vivo were also acquired. For this purpose, the intestine was placed on a black mat with markers, which allowed the Creality CR-Scan Otter 3D structured-light scanner equipped with 8 infrared LEDs, a 4-lens stereoscopic system, a scanning rate of 20 frames per second, 24-bit color capture, and an accuracy of approximately 0.02mm, as specified by the manufacturer to capture its geometry. The data obtained from this scanning procedure consisted of a point cloud.

To convert this point cloud into a usable 3D surface, the open-source software CloudCompare was employed (Girardeau-Montaut et al., 2016).

CloudCompare is a 3D point cloud processing software capable of handling data from laser scanners, triangular meshes, and calibrated images. The results of this procedure are presented in Figure. 21, which shows the 3D reconstruction of the intestine captured from multiple angles and in different configurations.

To make this geometry suitable for subsequent numerical simulations, it was necessary to clean and refine the mesh using Meshmixer, before following the procedure described in subsection. 4.2.2.

Figure 21: 3D image of the intestine obtained from 3D scan model using Creality Scanner.

4.3.3 High-resolution manometry

One way to validate the model is by reproducing a clinical procedure, namely high-resolution manometry (HRM) (Pandolfino and Roman, 2011; Arbizu et al., 2017), which is commonly used to assess gastrointestinal function. HRM is an adaptation of conventional manometric techniques, employing an increased number of closely spaced pressure sensors. The data generated by HRM are typically displayed as tracings, similar to conventional manometry, but with much higher spatial resolution.

This procedure can be applied to nearly any segment of the gastrointestinal tract, from the esophagus to the anus. While HRM is a powerful tool for evaluating gastrointestinal motility, it remains sensitive to various factors such as patient positioning, recent food intake, and surrounding organs, which can influence the measurements.

Figure. 22 illustrates the catheter placement, typically comprising 36 pressure sensors, the individual pressure traces recorded by each sensor, and a heatmap representing the high-resolution manometry data. This technique will be revisited in chapter. 5 to validate the results obtained from our numerical model.

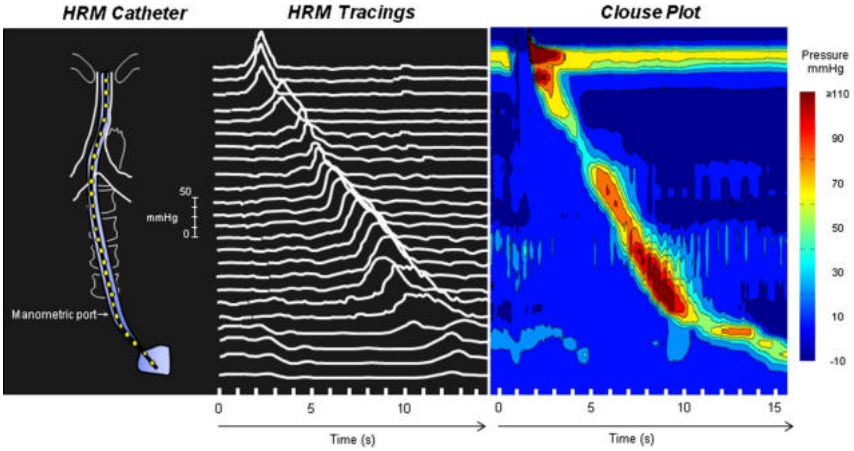

Figure 22: high-resolution manometry of the esophagus showing the placement of the sensors, and the pressure plot from each sensors (Pandolfino and Roman, 2011).

4.4 Conclusion

In this chapter, we focused on how clinical and experimental data can be integrated into numerical models to enhance their reliability. We began by describing how medical imaging data can be processed to obtain geometries suitable for finite element simulations. A complete workflow was presented, detailing the software used and the necessary file formats at each stage.

Next, we explained how experimental data were collected at the University of Auckland. Custom pressure sensors were developed to measure contact pressures, while a barostat was used to monitor luminal vol-

ume changes. Despite the inherent challenges of conducting these experiments in vivo, it was possible to reconstruct accurate 3D geometries of the intestine.

Finally, we discussed high-resolution manometry (HRM), a clinically essential technique for assessing gastrointestinal motility. The methodologies described in this chapter provide the foundation for improving and validating our numerical simulations, which will be further analyzed in chapters. 5 and 6.

Chapter 5

Digital twin model to enable 3D printing technologies

5.1 Introduction

In this chapter, we present the development and application of a digital model designed to simulate the implantation and functional behavior of a 3D bioprinted intestinal patch. The objective is to investigate how such a patch, once integrated into the intestinal wall, interacts with the underlying electromechanical activity of the tissue and contributes to restoring normal function.

We begin by analyzing the electromechanical behavior of the intestinal tissue under healthy conditions, using the model previously calibrated using the tests presented in the section 2.2 and appendices A. We will start by validating the model agains clinical observation, Then this validated framework serves as the reference for subsequent simulations. Building on this foundation, we then explore the effects of introducing a new bioprinted material layer, which is assumed to be attached to the intestinal surface via laser-assisted bonding. To better understand the influence of this engineered patch, a parametric analysis is performed

by varying the material properties and geometrical parameters of the patch. The simulations are conducted across different intestinal configurations, ranging from small- to large-intestine geometries, and include both physiological and pathological scenarios. Some parts of this chapter are adapted from author's previous publication (Djoumessi, Lenarda, Alessio Gizzi, Giusti, et al., 2024).

5.2 Problem configuration of the model and 3D-bioprinted patch setup

A series of numerical experiments is presented to characterize the coupled mechanical and electrophysiological response of an idealized segment of the human colon. These simulations aim to investigate and compare colonic motility under healthy conditions and post-surgical scenarios in which a portion of the computational domain—representing a lesion in the colonic epithelium—has been removed following a representative endoscopic submucosal dissection (ESD) and replaced with a 3D-printed implant patch. The numerical results are evaluated through intraluminal pressure topography maps and compared against available high-resolution colonic manometry data. Manometry is a diagnostic technique that quantifies intraluminal pressure within hollow organs, such as the esophagus, stomach, or intestines, using sensors integrated into a thin catheter (see subsection. 4.3.3 for more details). It provides detailed information on the amplitude, coordination, and propagation of muscular contractions, as well as sphincter function, and is therefore a key method for evaluating gastrointestinal motility disorders (Conklin, Pimentel, and Soffer, 2009; Li et al., 2019). Electrophysiological and mechanical constitutive parameters used in the simulations can be found in Tables 1 and 3, respectively.

Table 3: Mechanical constitutive parameters.

$\mu\,[\mathrm{kPa}]$	$k_1^l\,[\mathrm{kPa}]$	$k_2^l\,[-]$	$k_1^c\,[\mathrm{kPa}]$	$k_2^c\,[-]$	$k_1^d\,[\mathrm{kPa}]$	$k_2^d\,[-]$	$\theta\,[-]$
2.5	5.43	1.19	0.78	0.02	3.65	0.31	39.5

The computational domain is modeled as a hollow cylinder representing the typical dimensions of a tract of the human colon. Based on colonoscopy and surface measurements (Stauffer and Pfeifer, 2020; Helander and Fändriks, 2014), the colon diameter ranges from $4.8\ \mathrm{cm}$ to $6\ \mathrm{cm}$, while the transverse section length is approximately $50\ \mathrm{cm}$. In the present study, we consider a diameter of $5\ \mathrm{cm}$, a length of $50\ \mathrm{cm}$, and a wall thickness of $0.5\ \mathrm{cm}$. Figure 23 illustrates the geometry along with the applied boundary conditions.

The red elliptical region, characterized by semi-axes $r_{\min}$ and $r_{\max}$ and a thickness $h = 0.3\ \mathrm{cm}$, represents a bio-printed patch (e.g., albumin). Two representative implant geometries have been examined, fixing the minor semi-axis at $r_{\min} = 2\ \mathrm{cm}$ and varying the major semi-axis as $r_{\max} \in 2, 3\ \mathrm{cm}$. The patch is modeled as a Neo-Hookean material, with perfect bonding assumed at the tissue–patch interface to replicate the clinical condition of complete healing. The elastic modulus of the implanted patch, μ_p, is varied relative to that of the surrounding healthy tissue, μ_t, according to $\mu_p \in \mu_t/2, \mu_t, 2\mu_t$.

The intraluminal pressure generated by mechanical contraction was evaluated using Lamé's theory for thick-walled cylinders (Du, Lim, and Cheng, 2013; Choudhury, 2013; Lindeburg, 2019), enabling direct comparison with experimental manometry data. The circumferential stress σ_c in the cylinder wall was computed from the internal (p_i) and external (p_o) pressures, and the internal (r_i) and external (r_o) radii as:

$$\sigma_c = \frac{p_i r_i^2 - p_o r_o^2}{r_o^2 - r_i^2} - \frac{r_i^2 r_o^2 (p_o - p_i)}{r(r_o^2 - r_i^2)},, \tag{5.1}$$

where r is the radial coordinate, calculated from the Cartesian system aligned with the cylinder centerline.

For simplicity, and without loss of generality, the external pressure p_o exerted by surrounding tissues and organs was set to zero, ensuring equilibrium with the colon's cylindrical configuration. Since the active fibers on the inner surface of the colon are circumferentially oriented, the intraluminal pressure at $r = r_i$ can be expressed as:

$$p_i = \sigma_c \frac{r_o^2 - r_i^2}{r_o^2 + r_i^2},, \tag{5.2}$$

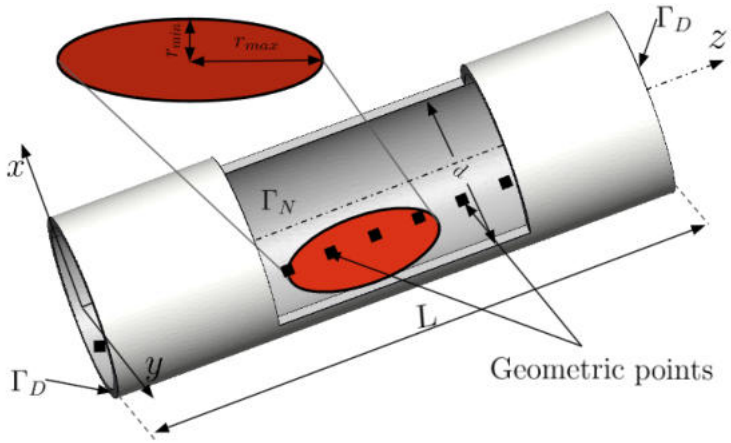

Figure 23: Sketch of the computational domain used in the numerical simulations with length $L = 50$ cm, diameter $d = 5$ cm, thickness 0.55 cm. Γ_D and Γ_N represent the Dirichlet and Neumann boundary conditions respectively. The red ellipsoidal region with axes $r_{\max}$, $r_{\min}$, and thickness $h = 0.3\,\mathrm{cm}$ represents the bio-printed patch. 'Geometric points' represent the points used to extract validation quantities.

so that, once electromechanical equilibrium is solved, σ_c is known and p_i can be directly obtained. Importantly, the pressure reported in the parametric studies corresponds to intraluminal surface, not to the hydrostatic pressure inside the solid due to material incompressiblity.

Topographic maps of intraluminal pressure, simulating high-resolution manometry, were generated following the clinical protocol in (Conklin, Pimentel, and Soffer, 2009; Li et al., 2019). In the simulations, p_i was evaluated at 36 equally spaced locations along the computational domain. The resulting values were then processed and visualized using an in-house `Matlab2022` code.

5.3 Healthy case and validation

The first numerical test aimed to simulate the electromechanical behavior of a healthy colonic tract (corresponding to the condition $\mu_p = \mu_t$).

Figure 24 shows the numerical results obtained by finite element simulations for two representative snapshots (a zoomed clip of the region of interest is shown in Appendix B.1). In particular, the spatial distribution of the SMC transmembrane potential u_s (first row) and the hydrostatic pressure p (second row) are shown in the deformed / contracted state. After a transient period of system stabilization (see section2.2 for details), multiple slow waves coexist on the domain and propagate in the axial direction, correctly reproducing healthy colon peristalsis.

Besides, manometry maps[1] (Fig. 24) and pressure topography maps (Fig. 25) provide a faithful representation of the intraluminal pressure generated by muscle contraction. Manometry map analysis reveals qualitative agreement with clinical data from the literature Arbizu et al., 2017, as illustrated in Fig. 24 for the healthy case. Specifically, the space-time diagram highlights the intensity and speed of propagation (slope computed as space/time) of p_i field (5.2). As observed in clinical data, a stronger intraluminal pressure is measured according to the excitation wave speed, thus changing along the GI tract in favor of the mixing function. Moreover, it is worth mentioning that in the healthy case, the motility pattern follows the propagating waves smoothly without impediments or gaps.

5.4 The role of patch geometry and stiffness

In this section, we provide a preliminary parametric analysis comparing different properties of the bio-printed patch, namely geometry and stiffness. Figure 26 shows a graphical representation of the numerical results obtained varying the size of the elliptical region $r_{\max} \in \{2, 3\}$ cm and considering a stiffer patch material other than the surrounding tissue, namely $\mu_p = 2\mu_t$.

[1] I would like to express my sincere gratitude to John Wiley and Sons for granting permission (License Number: 5752600572739, dated March 19, 2024) to reproduce Figure from the article "Prospective evaluation of same day versus next day colon manometry results in children with medical refractory constipation" by A. Arbizu L et al., published in Neurogastroenterology and Motility (Vol. 29, Issue 7, March 20, 2017). Their kind authorization made it possible to include this material in my thesis.

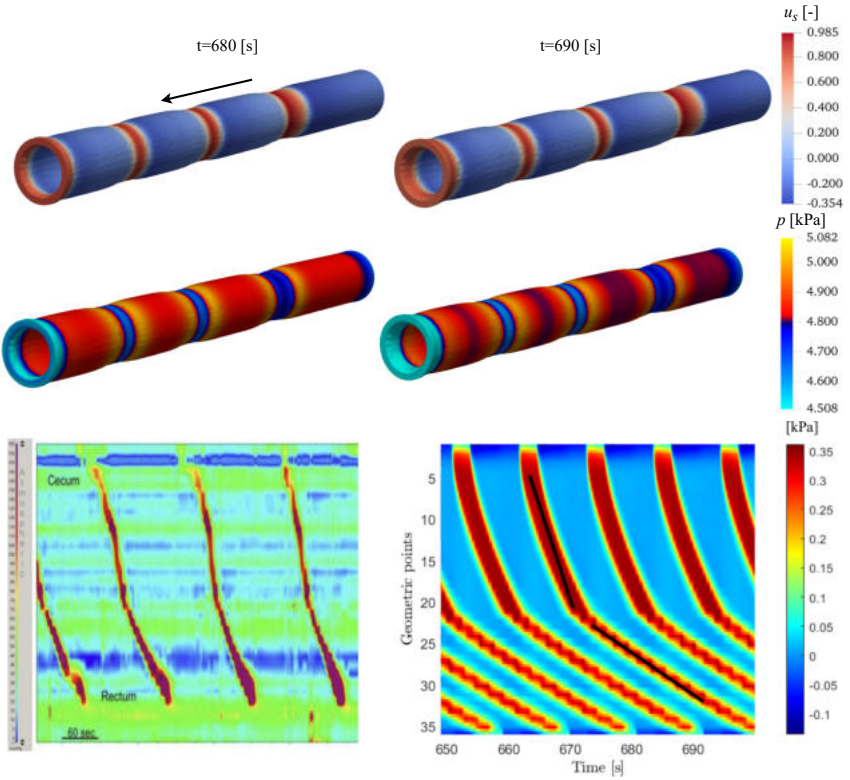

Figure 24: (Top) Temporal evolution of the SMC transmembrane potential u_s and hydrostatic pressure p in the healthy condition ($\mu_p = \mu_t$). The arrow represents the direction of propagation. (Bottom) Topography map of the intraluminal pressure p_i corresponding to HRM map in a healthy colon tract: (a) clinical results taken from (Arbizu et al., 2017), (b) numerical model with $\mu_p = \mu_t$. Black lines represent the slope, i.e., conduction velocity, in the space-time diagram.

It can be noticed that although the slow wave propagation is not considerably altered by the presence of the patch (representative of the case when the implant is fully cellularized), such that only geometrical couplings are implied, the intraluminal pressure distribution critically changes due to the presence of a stiff patch. In particular, the overall

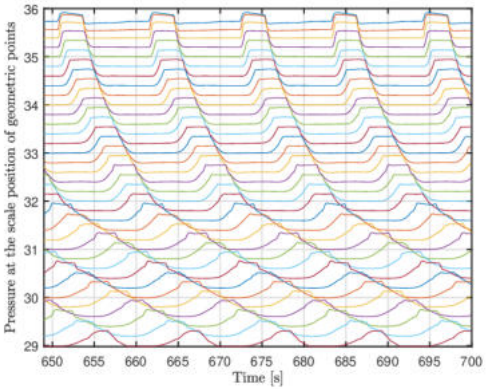

Figure 25: Pressure topography map corresponding to the numerical manometry in Fig. 24.

patch area shows much higher p_i levels (from about 5 kPa in the healthy case to more than 7 kPa in the stiff patch case), concurring to increase the stress state of the surrounding tissue and thus enhancing the development of pathological scars (Gizzi, Cherubini, Pomella, et al., 2012; Simone et al., 2018).

Figure 27 shows analyses conducted varying patch size $r_{\max} \in \{2, 3\}$ cm but considering a softer material other than the host surrounding tissue, namely $\mu_p = \mu_t/2$. As expected, a similar behavior is obtained for the SMC voltage field, i.e., the voltage field only experiences geometric coupling, but, in this case, the intraluminal pressure lowers (from about 5 kPa in the healthy case to less than 3 kPa in the soft patch case) on the overall patch region. Such a general stress mismatch could affect the stability of the implant (it may lose its position) with concurrent loss of contractility efficiency.

To further emphasize the critical role of material stiffness in the overall colon motility, we discuss the resulting topography maps for the selected pathological cases, as shown in Fig. 28 and Fig. 29. A direct comparison with the healthy case provided in Fig. 24 highlights that the region surrounding the patch material reduces its contractility for a stiffer

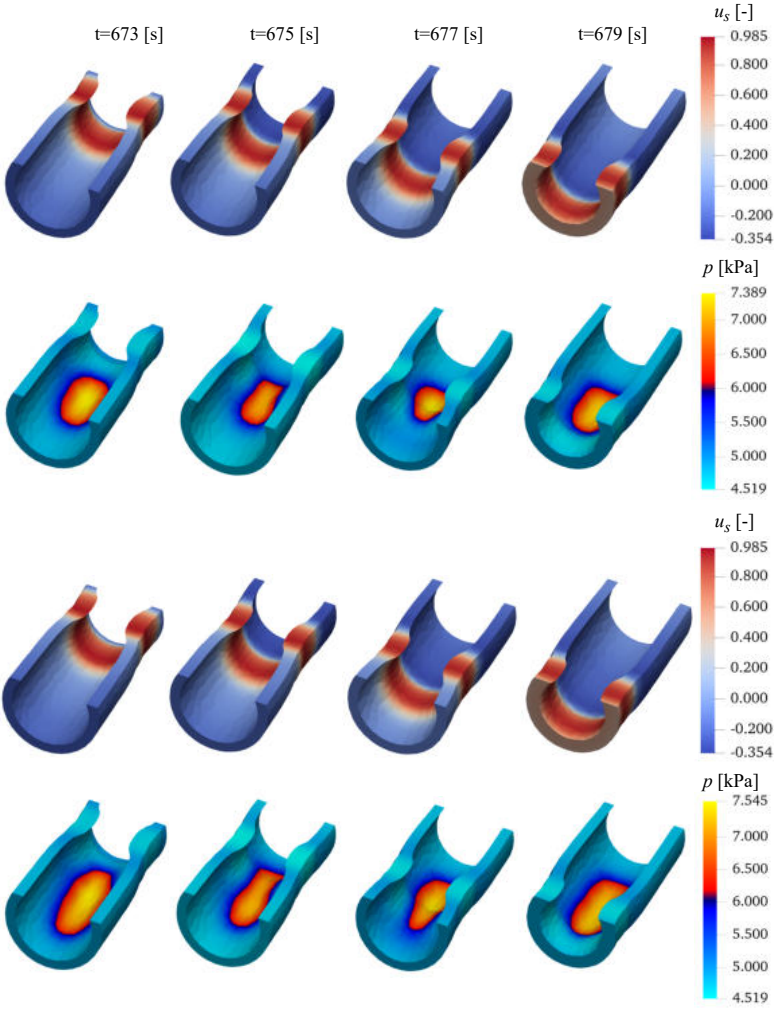

Figure 26: Temporal evolution of SMC transmembrane voltage u_s and hydrostatic pressure p in proximity of the patch region with parameters $r_{\max} = 2, r_{\min} = 2, \mu_p = 2\mu_t$ (top), and $r_{\max} = 3, r_{\min} = 2, \mu_p = 2\mu_t$ (bottom).

or softer patch. Moreover, a critical gap can be observed in the intra-

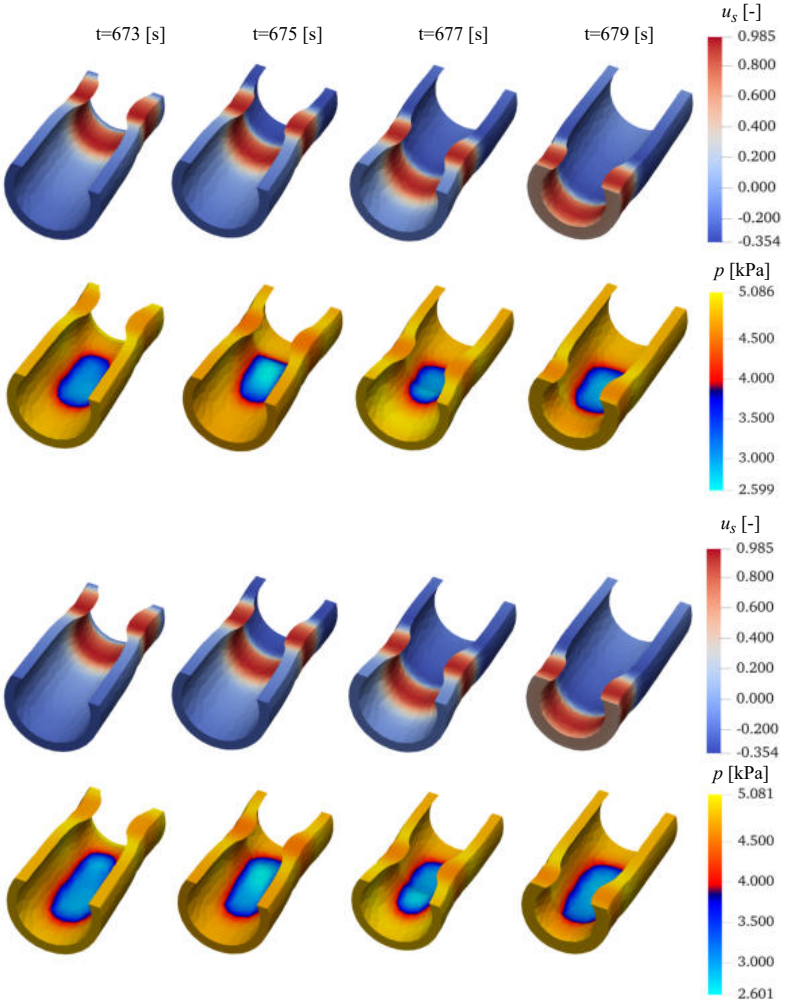

Figure 27: Temporal evolution of SMC transmembrane voltage u_s and hydrostatic pressure p in proximity of the patch region with parameters $r_{\max} = 2, r_{\min} = 2, \mu_p = 0.5\mu_t$ (top), and $r_{\max} = 3, r_{\min} = 2, \mu_p = 0.5\mu_t$ (bottom).

luminal pressure profiles that break, thus reducing the lateral wall dis-

placement. Such a contractility impairment is more evident in the case of the stiff patch, concurring to a wrong scar remodeling in the long-term tissue adaptation. Contrarily, selected differences in patch size do not alter the resulting motility behavior, which seems to be ruled by the patch material properties other than its geometrical features.

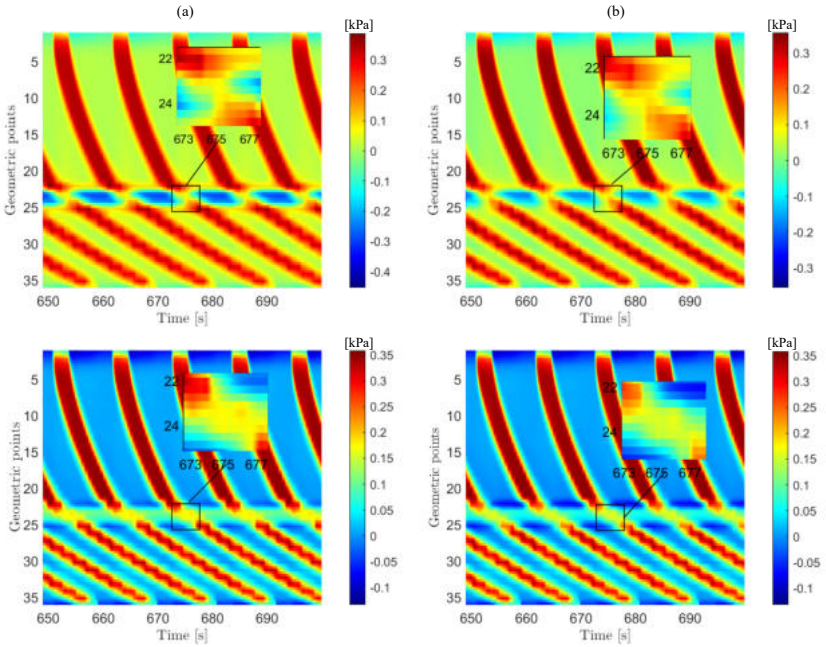

Figure 28: HRM maps for two implant configurations after the LTS with parameters $\mu_p = 2\mu_t$ (top) and $\mu_p = 0.5\mu_t$ (bottom). Columnwise discriminates between $r_{\max} = 2, r_{\min} = 2$ (a) and $r_{\max} = 2, r_{\min} = 3$ (b).

5.5 The role of patch electrical conductivity

In this numerical test, the electrophysiological properties of the implant are varied from those of the surrounding host tissue; namely, the SMC and ICC electrical conductivity in the patch, D_s^p, D_i^p, are ten times lower than those in the tissue, D_s^t, D_i^t. The size of the elliptical region is fixed

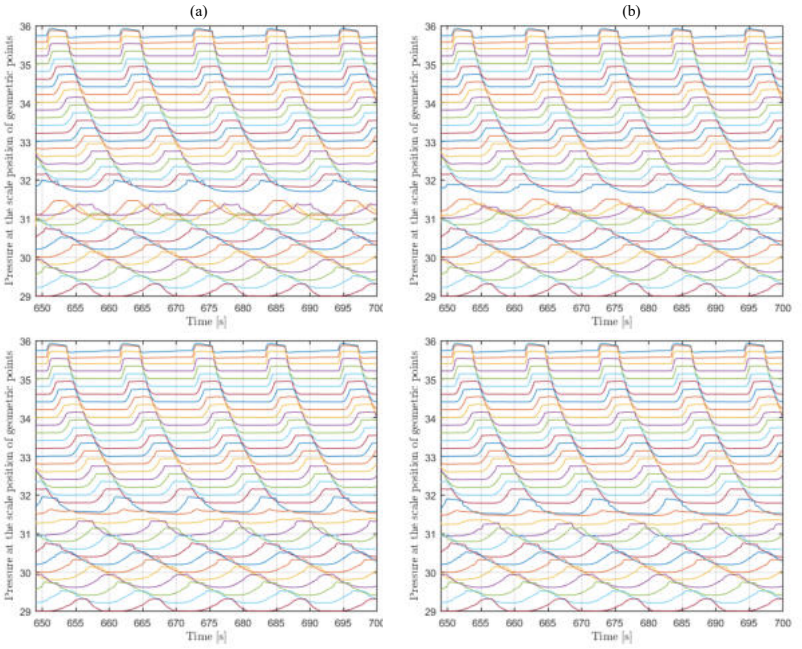

Figure 29: Topography pressure maps for the HRM in Fig. 28 two implant configurations after the LTS with parameters $\mu_p = 2\mu_t$ (top) and $\mu_p = 0.5\mu_t$ (bottom). Columnwise discriminates between $r_{\max} = 2, r_{\min} = 2$ (a) and $r_{\max} = 2, r_{\min} = 3$ (b).

at $r_{\min} = 2\,\mathrm{cm}$ and $r_{\max} = 3\,\mathrm{cm}$ and material stiffness is considered $\mu_p = 2\mu_t$.

Figure 30 shows the evolution of the hydrostatic pressure p in the surroundings of the implant, where no significant variations can be observed compared to the previous analysis in Fig. 26. However, because of the altered electrophysiological properties, the slow wave spatiotemporal distribution changes, and, in particular, the conduction velocity of the excitation wave lowers by enlarging the action potential wavelength when passing across the implant. Such a perturbation affects the overall displacement field inducted on the colon surrounding the patch, concurring with an altered pattern obtained for the intraluminal pressure

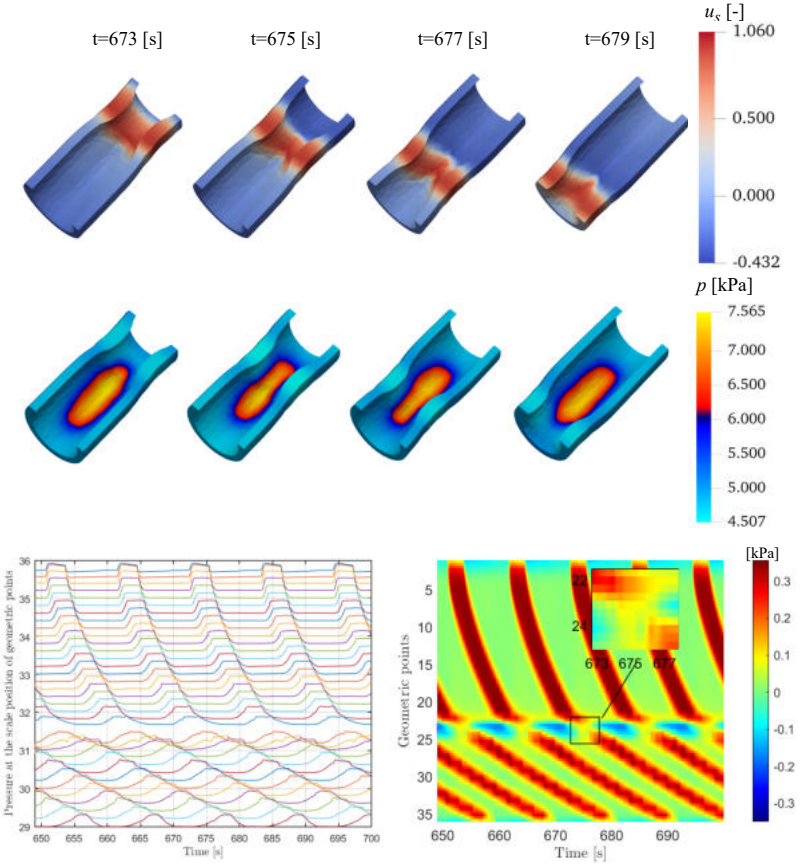

Figure 30: Temporal evolution of SMC transmembrane voltage u_s and hydrostatic pressure p around the patch region with parameters $r_{\max} = 3$ and $r_{\min} = 2$ with stiffness $\mu_p = 2\mu_t$ and the diffusion coefficients $D_s^p = 0.1D_s$ and $D_i^p = 0.1D_i$. HRM map with $\mu_p = 2\mu_t$ with in-homogeneous diffusivity $D_s^p = 0.1D_s$ and $D_i^p = 0.1D_i$.

map. Accordingly, such a preliminary analysis, in conjunction with the topographic pressure profiles in Fig. 30, confirms the sensitivity of colon motility to material stiffness and excitability. The gap in the p_i map is more pronounced than the case in Fig. 28 because the contraction of the

tissue surrounding the patch is delayed. To better understand the effect of diffusivity, we repeated the simulation by reducing again the diffusivity of the patch by ten, and the results are presented in Appendix B.2. The results confirm no significant difference with those provided in Fig. 30, which means that diffusivity alone has a minor effect on the overall material behavior.

5.6 The role of patch contractility

In this numerical test, the implant's electrophysiological properties and contractility vary from the surrounding host tissue. Namely, the SMC and ICC electrical conductivity in the patch, D_s^p, D_i^p, are a hundred times lower than those in the tissue, D_s^t, D_i^t, and the amplitude of contractility in Eq. (3.6), α_l^p, α_c^p, is reduced as by 50%. The size of the elliptical region is fixed at $r_{\min} = 2\,\mathrm{cm}$ and $r_{\max} = 3\,\mathrm{cm}$ and material stiffness is considered $\mu_p = 2\mu_t$.

Figure 31 shows the evolution of the hydrostatic pressure p in the surroundings of the implant. It is worth noting that due to the reduction of contractility, significant variations can be observed in hydrostatic pressure compared to the case in Fig. 26. As electrophysiological properties are altered, the slow wave spatiotemporal distribution changes, and, in particular, the conduction velocity of the excitation wave lowers by enlarging the action potential wavelength when passing across the implant. The two contributions notably affect the overall displacement field u where a low displacement of 0.4 cm is observed around the patch (see third row in Fig. 30), enforcing an altered motility pattern demonstrated by a clear gap in the intraluminal pressure profile in Fig. 31–a p_i gap more pronounced compared to the case in Fig. 30. Accordingly, such analysis confirms the sensitivity of colon motility to material stiffness, excitability, and contractility.

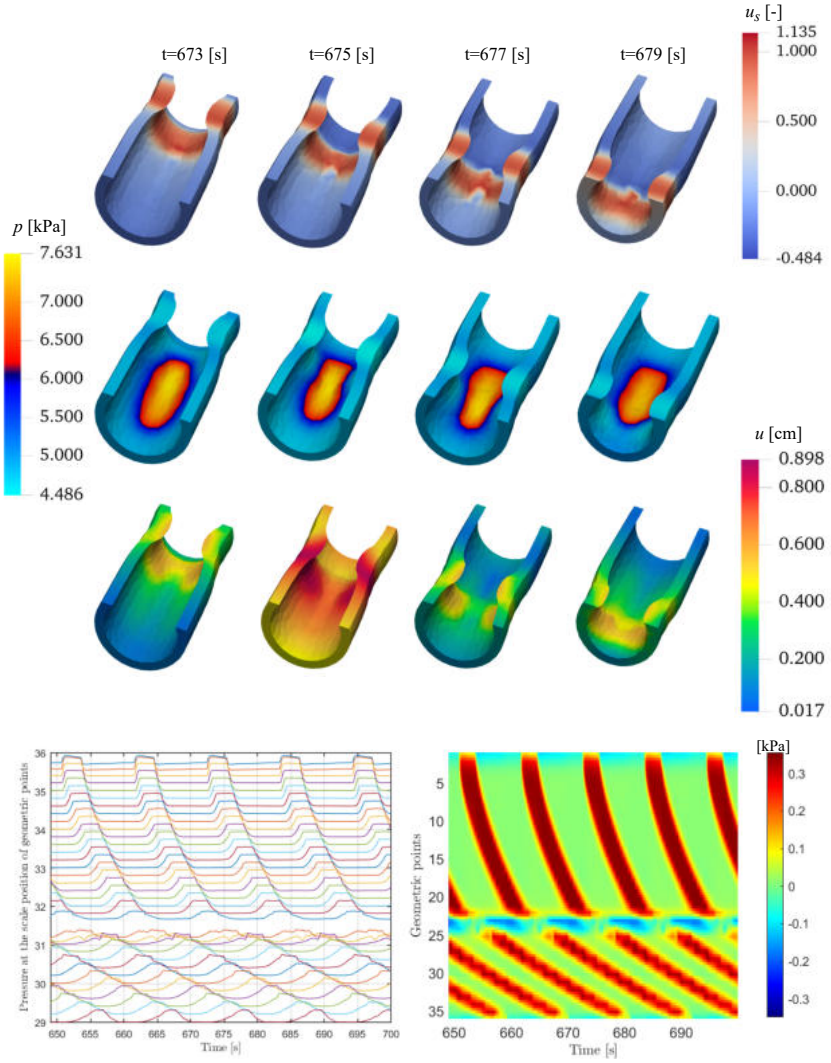

Figure 31: Temporal evolution of SMC transmembrane voltage u_s, of hydrostatic pressure p and the displacement u around the patch region with parameters $r_{\max} = 3$ and $r_{\min} = 2$ with stiffness $\mu_p = 2\mu_t$ and the diffusion coefficients $D_s^p = 0.01D_s$ and $D_i^p = 0.01D_i$. HRM map with $\mu_p = 2\mu_t$ with in-homogeneous diffusivity $D_s^p = 0.01D_s$ and $D_i^p = 0.01D_i$ and the contractility $\alpha_l^p = 50\%\alpha_l$ and $\alpha_c^p = 50\%\alpha_c$.

5.7 The role of a non-cellularized patch

In this numerical test, we consider a patch not yet fully cellularized (representative of an early healing stage) with altered electrophysiological properties. Namely, the SMC and ICC electrical conductivity D_s^p, D_i^p are 10^2 times lower than those in the tissue, D_s^t, D_i^t, and the reaction terms Eq. (2.3) are 10^3 times lower (i.e., the reaction terms are multiplied by a constant 10^{-3} factor). The patch size and stiffness are maintained as in the previous case.

Figure 32 shows the evolution of the hydrostatic pressure p in the surroundings of the implant. Though no significant variations are observed compared to the case in Fig. 26, altered electrophysiological properties induce a critical change in slow wave spatiotemporal dynamics leading to wavebreaks around the patch (no closed rings). In particular, the excitation wave is slowed, and its amplitude is reduced, thus flattening and prolonging the duration of SMC action potential. The two reaction-diffusion contributions affect the colon wall's overall motility, leading to an altered pattern of intraluminal pressure maps: a clear gap in the recorded traces is representative of no contraction. This analysis is aligned with the topographic pressure profiles presented in Fig. 32, further confirming the sensitivity of colon motility to cellular viability of bioprinted material.

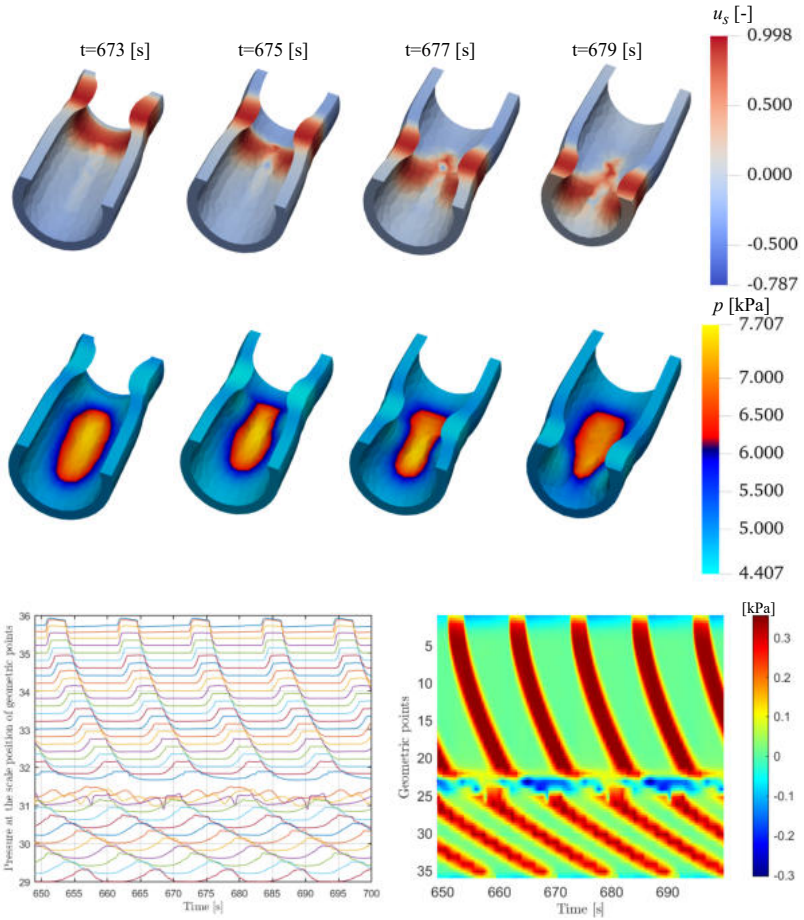

Figure 32: Temporal evolution of SMC transmembrane voltage u_s and hydrostatic pressure p around the patch region with parameters $r_{\max} = 3$ and $r_{\min} = 2$ with stiffness $\mu_p = 2\mu_t$ and the diffusion coefficients $D_s^p = 0.01 D_s$ and $D_i^p = 0.01 D_i$. HRM map with $\mu_p = 2\mu_t$ with in-homogeneous diffusivity $D_s^p = 0.01 D_s$ and $D_i^p = 0.01 D_i$ with the reaction terms (Eq. (3.22)) 10^3 times lower inside the patch.

5.8 The role of patch contractility and altered electrophysiology

In the last numerical test, we combine the multiple cases discussed before by considering a not fully cellularized patch (reducing the reaction terms by 10^{-3} and the diffusion coefficients by 10^{-2}) but also considering a reduced material contractility via α_l^p, α_c^p lowered by 50%. Size and stiffness of the patch are maintained as in the previous case.

Figure 33 shows the results of the combined ill cases. As expected, hydrostatic pressure and slow waves are affected similarly, as well as the displacement field u, which is practically two times lower than the case in Fig. 31. However, in relation to HRM and topography maps, no contraction is associated with a reduced displacement of 0.006 cm, complemented by a larger gap on the map p_i comprising a wider region around the patch. Such a comprehensive analysis confirms the role and sensitivity of colon motility to bio-printed material properties in various features.

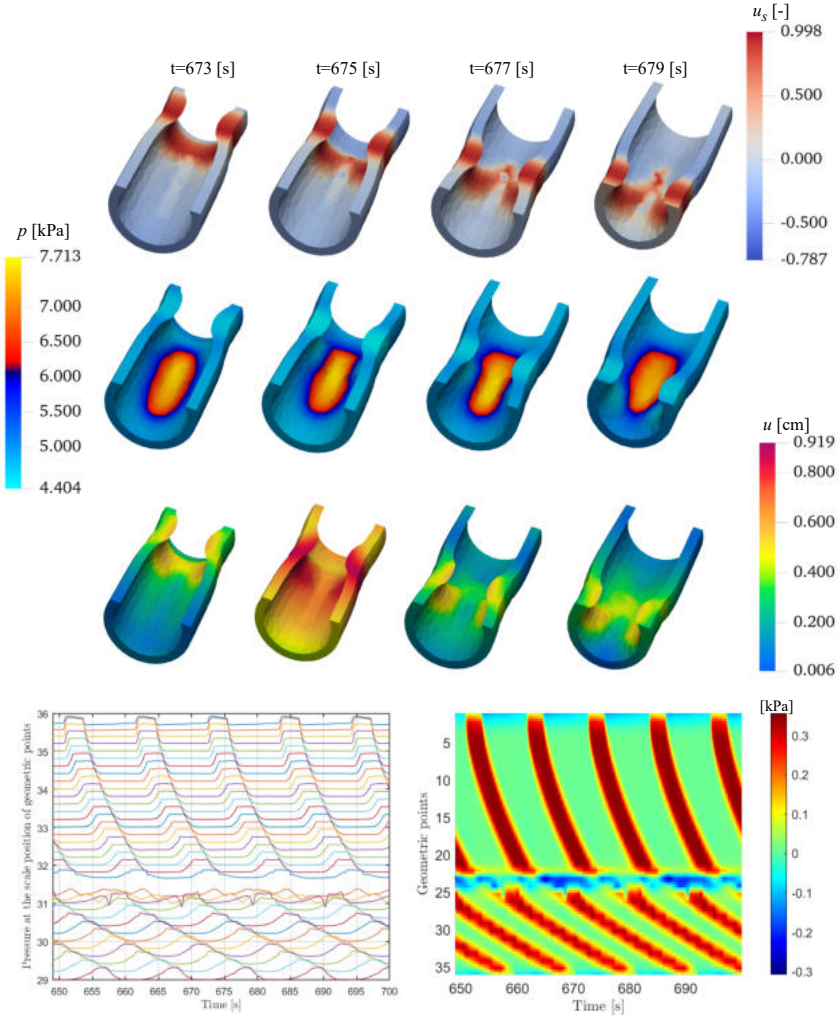

Figure 33: Temporal evolution of SMC transmembrane voltage u_s, the hydrostatic pressure p and the displacement u around the patch region with parameters $r_{\max} = 3$ and $r_{\min} = 2$ with stiffness $\mu_p = 2\mu_t$ and the diffusion coefficients $D_s^p = 0.01 D_s$ and $D_i^p = 0.01 D_i$. HRM map and the pressure map with $\mu_p = 2\mu_t$ with in-homogeneous diffusivity $D_s^p = 0.01 D_s$ and $D_i^p = 0.01 D_i$ and the contractility $\alpha_l^p = 50\% \alpha_l$ and $\alpha_c^p = 50\% \alpha_c$ and the reaction terms (Eq. (3.22)) 10^3 times lower inside the patch.

5.9 Electromechanics in real duodenum model

In this section, the electromechanical model is applied to a realistic geometry of the human duodenum, reconstructed from CT-scan data. The geometry was prepared following the procedure described in chapter. 4. The electromechanical model was then employed to simulate peristaltic motion on this anatomical configuration and the material parameters were the same used to obtain the results in Figure. 34.

As shown in Figure. 34, and consistent with the results presented in Figure. 24, the electrical wave forms concentric bands that propagate along the intestine, indicating a good agreement between the results obtained on the idealized geometry and those on the realistic one.

Furthermore, it is observed that the slow waves induce muscle contractions that are in phase with the electrical activity. Another important observation is that the propagation speed of the slow waves increases in the curved regions of the duodenum, which is in perfect agreement with the results previously reported in Figure. 24. Observing Figure. 34, we observe that the hydrostatic pressure measured in a healthy human duodenum is approximately twice as large as the value reported in the idealized healthy case of our simulation (see Figure. 24). This difference can be attributed to the complex geometry of the real duodenum, which includes anatomical features such as curvature, nonuniform wall thickness, mucosal folds, and varying luminal diameter. These structural complexities tend to create localized pressure concentration zones, which naturally increase the hydrostatic pressure compared to that obtained from an idealized, smoother geometry.

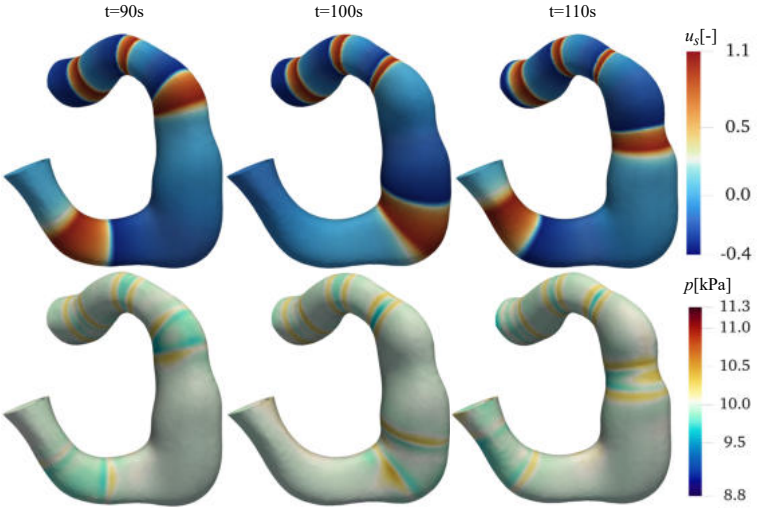

Figure 34: Temporal evolution of the SMC transmembrane potential u_s and hydrostatic pressure p in the healthy human duodenum.

5.10 Conclusion

In this chapter, we presented the results obtained from the electromechanical model developed in chapters. 2 and 3. We began by defining the problem framework and describing the 3D bioprinted patch setup. Before investigating the specific effects of the bioprinted patch, the model was first validated to ensure that it accurately reproduced clinical observations of intestinal motility.

Once validated, the model was employed to perform a parametric study of the patch's influence on intestinal motility. In particular, we analyzed the effects of patch size, contractility, conductivity, and stiffness. The results revealed that the size of the patch was less critical than its material composition. When the newly deposited material was less stiff than the healthy tissue, weak contractions were still observed within the patch region, as confirmed by the manometric curves. Conversely, when the patch was stiffer than the surrounding tissue, no contraction was detected.

Moreover, in the case of a rigid and non-cellularized patch, the simulations showed that it did not respond to electrical activation, confirming its mechanical passivity in the absence of functional cells.

One of the main limitations of this model lies in its use of an idealized cylindrical geometry. In reality, the intestine can come into contact with itself or with external medical devices during certain clinical procedures. These interactions are not captured in the present formulation. In the next chapter, we will therefore introduce the mechanics of contact and discuss how it enhances the realism of the model by accounting for self-contact and external device interactions.

Chapter 6

Digital twins of the gastrointestinal pathologies

6.1 Introduction

In this chapter, we present the results obtained by introducing contact mechanics into the previously developed electromechanical model. We first focus on the integration of self-contact, followed by the analysis of the interaction between the intestine and external devices. However, it should be noted that the results for the second case remain preliminary and have not yet been fully validated. The purpose of this chapter is to demonstrate that the proposed approach enables the simulation of more complex and clinically relevant scenarios.

We begin by defining the problem configuration for each case. The self-contact model is first validated using a benchmark test and further supported by clinical observations. Once validated, this model is employed to investigate the effects of pre- and post-surgical pathological conditions on intestinal motility.

The second model, involving the contact between the intestine and an external distension balloon, is then introduced and validated. This configuration is used to explore the mechanical and physiological interactions arising during clinical procedures. Finally, a simplified case study

is presented using a patient-specific geometry, illustrating the applicability of the framework to realistic anatomical configurations.

Some parts of this chapter are adapted from author's previous publications (Djoumessi, Lenarda, Alessio Gizzi, Giusti, et al., 2024; Djoumessi, Lenarda, Alessio Gizzi, and Paggi, 2025).

6.2 Problem configuration and effect of surrounding organs

6.2.1 Problem configuration

The model problem considers a segment of the intestine, geometrically idealized as a three-dimensional U-shaped domain (Figure. 35). This configuration was selected to represent an intestinal section that may undergo self-contact, either during peristaltic wave propagation or as a consequence of pathological conditions leading to displacement from its physiological configuration.

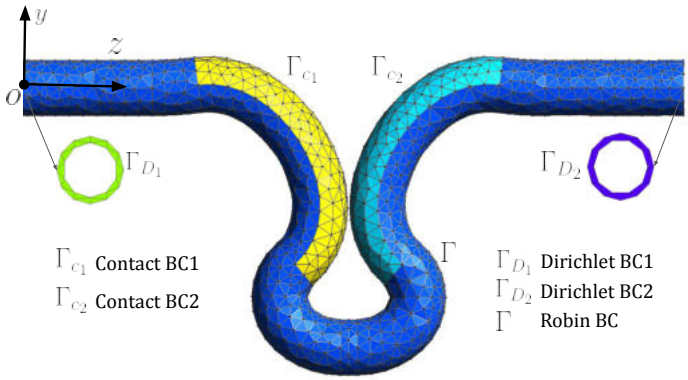

Figure 35: Problem setting: Γ_{c_1} and Γ_{c_2} are contact surfaces, while Γ, Γ_{D_1}, and Γ_{D_2} are used for Robin and Dirichlet boundary conditions, respectively.

As shown in Figure. 35, the contact surfaces are identified as the inner faces of the structure, highlighted in yellow and cyan, and denoted by

Γ_{c_1} and Γ_{c_2}, respectively. The end surfaces, depicted in green and violet, correspond to the Dirichlet boundary regions (Γ_{D_1}, Γ_{D_2}) and are either fixed or assigned a prescribed displacement, depending on the specific problem setup.

6.2.2 Effect of surrounding organs

Unlike other organs, the intestine is not protected by the rib cage, which makes it susceptible not only to self-contact but also to interactions with surrounding organs. Such contacts can have a significant impact on intestinal motility, potentially altering manometric recordings. Since these interactions are not uniformly distributed, we developed in this section a special boundary condition that accounts for this effect by introducing a distributed stiffness representation. To account for distributed springs connecting the intestine with the surrounding soft tissues, we impose the following Robin boundary condition (see Figure. 36):

$$\boldsymbol{P}\boldsymbol{N} + \eta(r,z) J \boldsymbol{F}^{-T} \boldsymbol{u} = \boldsymbol{0}, \quad \text{on } \partial\Omega \times (0, t_{\text{final}}) \tag{6.1}$$

where, $\boldsymbol{N}$ is the unit normal at the reference configuration and the term $\eta(r,z)$ represents a spatially varying stiffness defined as:

$$\eta(r,s) = \eta_{min} + (\eta_{max} - \eta_{min}) \left(1 + \beta \frac{|s - s_{min}|}{|s_{max} - s_{min}|}\right) \exp\left(-\gamma \frac{r - R}{R}\right) G_\theta(\theta), \tag{6.2}$$

with, $r = \sqrt{(x - x_c(s))^2 + (y - y_c(s))^2}$ the radial distance from the centerline coordinates $(x_c(s), y_c(s))$ and s the curvilinear coordinate; η_{min} and η_{max} are the minimum and maximum stiffness values, respectively; β introduces a stiffness gradient along the z_c-direction; R denotes the mean radius of influence of the surrounding organs on the considered GI tract; γ controls the radial decay of the stiffness coefficient $\eta(r,s)$ around R, such that the stiffness decreases progressively with distance from the mean radius. Finally, $G_\theta(\theta)$ is an azimuthal Gaussian function defined as:

$$G_\theta(\theta) = \begin{cases} \exp\left(-\dfrac{(\theta - \theta_0)^2}{2\sigma^2}\right), & \text{if } |\theta - \theta_0| \leq \frac{\pi}{2}, \\ 0, & \text{else}, \end{cases} \tag{6.3}$$

where, the azimuthal angle θ is defined as $\theta = \arctan 2(y - y_c(s), x - x_c(s))$; σ stands for the standard deviation and θ_0 is the preferred azimuthal angle.

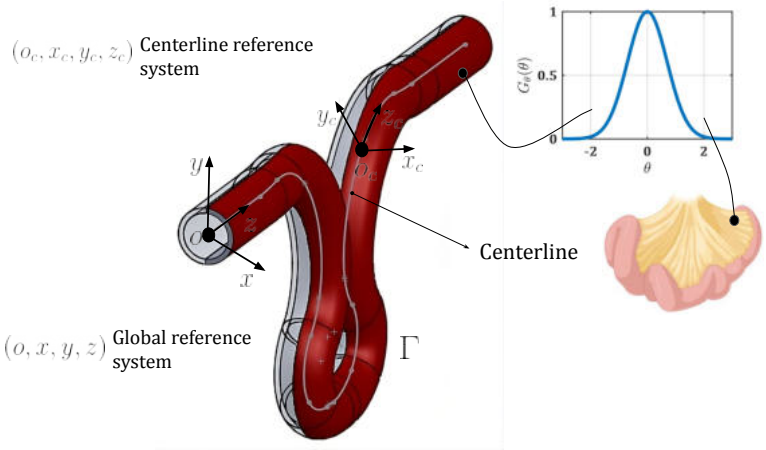

Figure 36: Schematic of the distribution of the stiffness η on the boundary Γ. The stiffness is distributed along the surface by means of the Gaussian function $G_\theta(\theta)$ linked to the local reference system, $(0_c, x_c, y_c, z_c)$ on the centerline, whereas $(0, x, y, z)$ stands for the global coordinate system.

The spatial distribution of $\eta(r, s)$ considers axial and radial heterogeneities in stiffness, avoiding out-of-plane displacements (see Fig. 58(a)). Such an approach is inspired by (Propp et al., 2020) and allows us to model several scenarios which will be analyzed in the subsequent sections: (i) the mechanical interaction between the digestive tract and its environment (mesentery); (ii) the presence of an herniation in a pre-surgical setting; (iii) the adhesion syndrome as a result of a post-surgical stiffening and the development of scar bands. The spatially varying stiffness function $\eta(r, s)$ reflects the fact that the mesentery does not uniformly surround the intestine. Anatomically, the mesenteric insertion typically covers only a portion of the intestinal circumference—usually on the posterior-lateral side—and its mechanical influence decreases gradually away from this region (see Figure. 36). This non-uniformity is cap-

tured by combining a radial exponential decay with a gaussian distribution in the azimuthal direction. In addition, a longitudinal gradient is introduced to mimic physiological variations along the bowel length. This formulation allows us to represent the compliant yet directionally localized mechanical support provided by the mesentery in a biomechanically and anatomically consistent manner.

6.3 Taking self-contact in the model

In this section, we begin by validating our contact model and then proceed to use it to investigate the cases of interest.

6.3.1 Validation of the contact model

Before performing any simulations, it is essential to ensure that the contact algorithm operates correctly. To this end, the contact method was tested against a benchmark problem from Wriggers et al. (Wriggers, Schröder, and Schwarz, 2013). The problem configuration is explained in Fig .37. In this benchmark, the upper body is moved downwards in progressive steps to compress the elastic foundation. We model the upper body and the foundation as linear elastic materials with different material properties. The constitutive law for each solid is characterized by $\boldsymbol{\sigma} = \lambda \text{tr}(\epsilon)\mathbf{I} + 2\mu\epsilon$, where λ and μ are the Lamé constants and ϵ is the strain. The following material properties were $E_u = 7000$ MPa, $E_f = 70000$ MPa, $\nu_u = 0.3$, and $\nu_f = 0.45$, where the subscripts 'u' and 'f' stand for the upper body and foundation, respectively. The numerical test is performed using the following weak form for all test functions $\delta\boldsymbol{v}$ belonging to an admissible Hilbert space.

$$\begin{aligned} \mathcal{B}(\boldsymbol{u}; \delta\boldsymbol{v}) := &\int_{\Omega_0} \boldsymbol{\sigma}(\boldsymbol{u}) : \epsilon(\delta\boldsymbol{v}) \, \mathrm{d}V \\ &+ \int_{\Gamma_{c_u}} K_0 \langle \text{tol} - g_{c_u} \rangle \boldsymbol{n}_{c_u} \cdot \delta\boldsymbol{v} \, \mathrm{d}\Gamma \\ &+ \int_{\Gamma_{c_f}} K_0 \langle \text{tol} - g_{c_f} \rangle \boldsymbol{n}_{c_f} \cdot \delta\boldsymbol{v} \, \mathrm{d}\Gamma = 0, \end{aligned} \tag{6.4}$$

In Eq. 6.4, $\boldsymbol{n}_{c_u}$ and $\boldsymbol{n}_{c_f}$ denote the contact normals, and g_{c_u} and g_{c_f} represent the corresponding contact gaps, computed from the contact boundaries Γ_{c_u} and Γ_{c_f}, respectively. The normal stress distribution obtained with the contact method is reported in Fig. 37.

We observe that the method exhibits a violation when the compression is maintained beyond a certain threshold (tol). However, this gap violation appears to be minimally affected by the defined tolerance. The vertical displacement of the foundation against the vertical displacement of the upper body is shown in Fig. 37 as reported in (Wriggers, Schröder, and Schwarz, 2013). The results show little variation with respect to the tolerance, demonstrating the robustness of the method.

An additional analysis was performed to assess the computational cost of our algorithm. Specifically, we compared the time required to compute the contact gap in two configurations: with and without the use of nearest neighbor search (NNS). The analysis was carried out as a function of the number of degrees of freedom (DoFs) in the system. As shown in Fig. 37, the incorporation of NNS leads to a substantial reduction in computational time, particularly at higher DoFs. The figure also reports the time-saving percentage per degree of freedom. Notably, for problems with a small number of DoFs, the overhead introduced by the NNS may outweigh its benefits, resulting in a negative time saving. However, as the DoFs increase, the efficiency gain becomes increasingly pronounced, demonstrating the scalability and effectiveness of the NNS-based approach for large-scale problems.

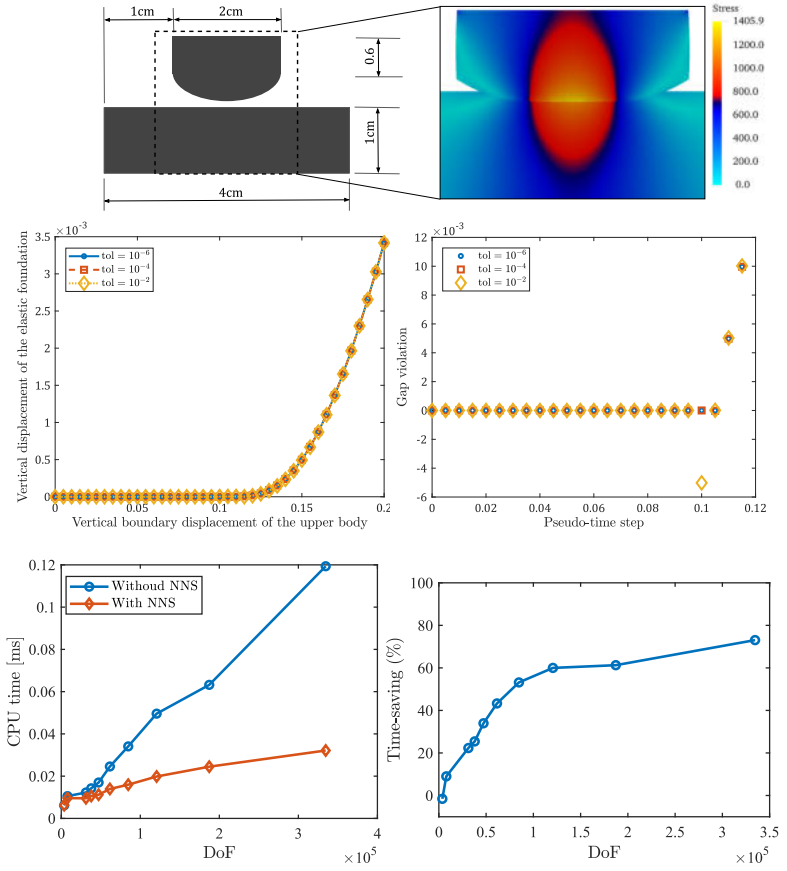

Figure 37: Benchmark problem of the compression of an elastic body against an elastic foundation. The mesh was refined with a local dimension of 0.03 cm for the two bodies. The zoom plot shows the stress, gap violation and vertical displacement of the plate for the benchmark problem. The two solids are modeled as linear elastic bodies with different material properties: $E_u = 7000$ MPa , $\nu_u = 0.3$, $E_f = 70000$ MPa , $\nu_f = 0.45$. The last two figures represent the computational time with and without the nearest neighbor contact search (NNS) vs. the number of DoFs. and time-saving percentage per degree of freedom.

6.3.2 Modeling of the presence of the mesentery/ surrounding organs

The present case is considered as a reference for a healthy condition. The boundary parameters used to simulate the effect of the mesenteric layer attaching the intestine tract to the posterior abdominal wall are given in Tab. 4. The numerical analysis was performed maintaining the same electrophysiological and mechanical properties as those used in the case shown in Appendix D, where no confinement was considered.

Table 4: Parameters for distributed boundary conditions.

η_{max} [kPa/cm]	η_{min} [kPa/cm]	σ [rad]	β [$-$]	γ [$-$]	θ_0 [rad]
0.3	0.1	$\pi/3$	0.5	0.2	0.0

When comparing the two cases, due to the lack of any mechano-electric feedback, we observe the same spatiotemporal distribution of membrane potential u_s (see Fig. 38). However, a notable difference in the global displacement $\boldsymbol{u}$ is obtained. In the unconfined case (Fig. 57) the displacement reaches a maximum of 1.52 cm. In contrast, with the application of the Robin-type condition, the global displacement is reduced by approximately 0.67 cm (see Fig. 38). Pressure distribution curves also show higher values in the unconfined case.

Indeed, without a distributed boundary condition, the intestine moves more freely, leading to increased pressure. To better illustrate our findings, Fig. 39 compares the displacement configurations among the two cases at selected times. The results clearly show that when the intestine is not confined by the presence of other organs, it exhibits significant motility, even in the out of the plane direction, as highlighted in Fig. 39(a). In contrast, when the Robin boundary condition is applied, the domain is stabilized and prevented from moving freely in all directions, as shown in Fig. 39(b).

Figure 40 confirms quantitatively such an observation, showing the displacements in the x- (Fig. 40(a)) and z- (Fig. 40(b)) directions. Figure. 40(c) further shows the intraluminal pressure map (manometry patterns) for the distributed boundary case. Regions labeled as 'Geometric

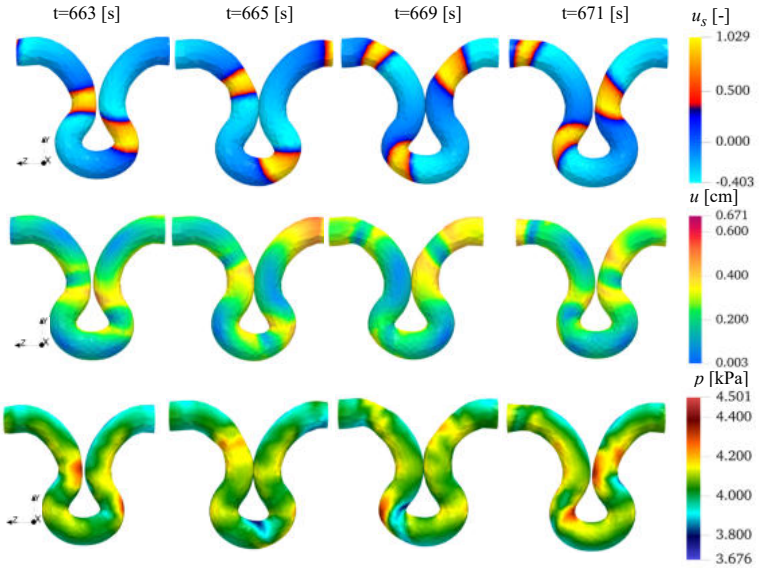

Figure 38: Temporal evolution of SMC transmembrane voltage u_s, hydrostatic pressure p and displacement u. Electrophysiological and mechanical parameters in Tab. 1(Healthy case).

pressure' represent constant pressure values induced by the corners of the geometry. Regions labeled 'Contact pressure' are due to the pressure exerted by the self-contact boundary. While these pressures are essential for understanding the structure of the problem, they do not significantly affect the peristaltic motion, as confirmed by the diagonal patterns in Fig. 40(c). However, it is worth noticing that the model can highlight areas characterized by pressure concentrations and the pressures induced by contact between the intestinal surfaces.

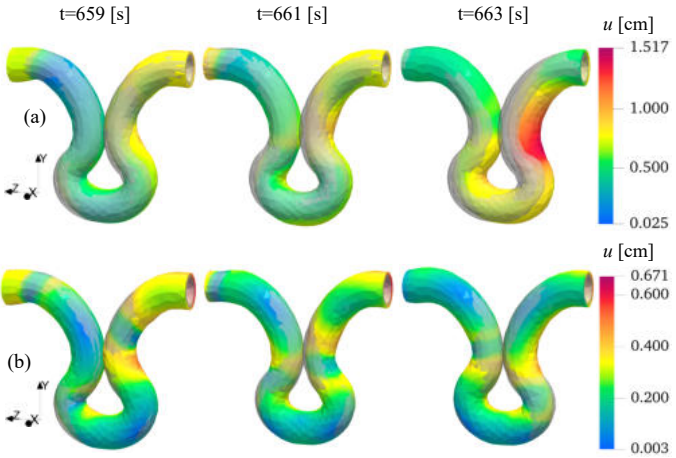

Figure 39: Effect of the Robin boundary condition. Displacement magnitude $\boldsymbol{u}$ (a) without and (b) with the Robin boundary condition applied.

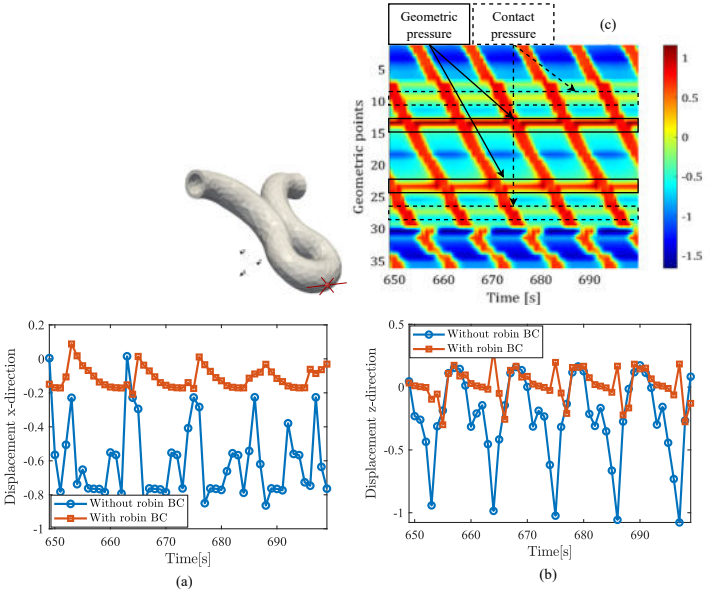

Figure 40: Comparison of displacement components time course at point $(0, -17, 19.4)$: (a) $x-$direction, (b) $z-$direction and (c) Simulated manometry for the healthy case. The regions labeled as 'Geometric pressure' represent constant pressures induced by the corners of the geometry while the regions labeled 'Contact pressure' are due to the pressure exerted by self-contact. Geometric points (not shown in Fig. 35) refer to 36 points spaced 1 cm apart, extracted from the inner surface of the geometry presented in Fig. 36 along the centerline. Please reader should see in (Djoumessi, Lenarda, Alessio Gizzi, Giusti, et al., 2024) for more details

6.3.3 Effect of contact mechanics and clinical validation

For this discussion, we revisit the manometric data obtained from both the experimental model and the simulation performed without mechanical contact (Fig. 41). This initial simulation allowed us to formulate several hypotheses, since a comparison between the experimental and simulated manometry revealed distinct pressure bands in the experimental data that were absent in the simulation. These observations led us to question whether the pressure bands could be attributed to the position of the intestine within the abdominal cavity, to self-contact of the intestine, or to interactions with surrounding organs.

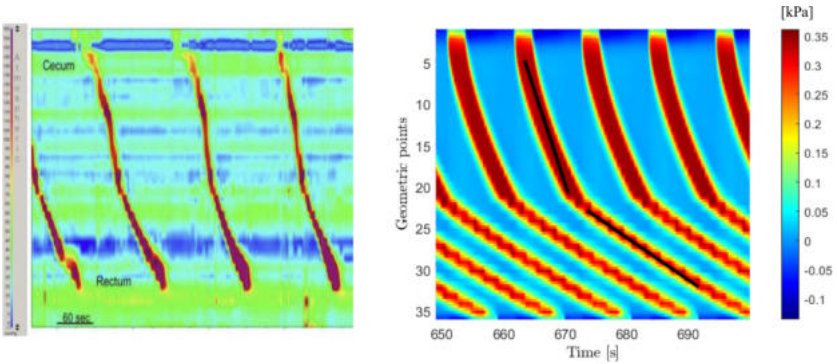

Figure 41: Topography map of the intraluminal pressure p_i corresponding to HRM map in a healthy colon: clinical results taken from (Arbizu et al., 2017), and numerical model with $\mu_p = \mu_t$. Black lines represent the slope, i.e., conduction velocity, in the space-time diagram.

By subsequently introducing self-contact and implementing a special boundary condition that accounts for the presence of the mesentery, we were able to address these hypotheses. As shown in the manometric curve of Figure. 40(c), and by comparing it with the experimental recordings, we observed that the missing pressure bands indeed appeared in the updated simulation. This result highlights the critical role of contact mechanics in accurately modeling the intestinal system.

6.3.4 Modeling strangulation in abdominal hernia

We consider intestinal hernias as a clinical case study (see Fig. 42). Intestinal hernia is a pathological condition in which part of the intestine protrudes through an opening in the abdominal wall or a weakened muscle. Such a condition can occur in a number of anatomical locations, notably in the groin (inguinal hernia) or around the navel (umbilical hernia). Two levels of herniation are considered, moderate and severe (Wiesner and Mortele, 2011; Slater et al., 2014; Şimşek et al., 2020).

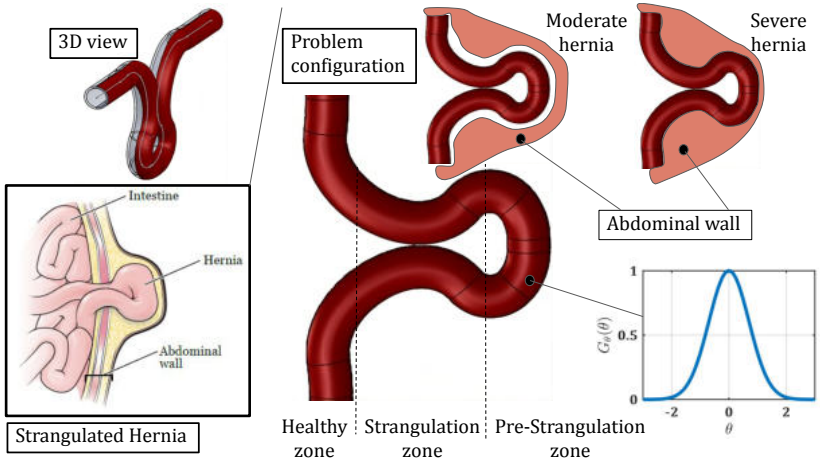

Figure 42: An abdominal strangulated hernia (picture adapted from (Center, 2023)). Hernia problem configuration schematics. The mesentery boundary is highlighted in red with associated Gaussian function $G_\theta(\theta)$. Healthy section, strangulation and pre-strangulation zones are identified. Moderate and severe hernia cases are provided on the right.

The area affected by a hernia can be divided into three distinct zones (as shown in Fig. 42), each with specific mechanical properties. In the healthy zone, the intestinal wall retains its physiological elastic characteristics. In the strangulation zone, blood flow is interrupted, leading to ischemia, degradation of cellular structures, and a significant increase in stiffness. Finally, the pre-strangulation zone is subjected to mechanical stress with possible signs of inflammation and edema, leading to an

intermediate stiffness between the healthy zone and the strangulation zone, influenced by fluid accumulation and partial tissue degradation (Wiesner and Mortele, 2011; Sghaier et al., 2023; Şimşek et al., 2020). Simulation parameters are given in Tab. 5.

Table 5: Mechanical and Electrophysiological parameters used for Hernia simulation.

Mechanical Parameters			
Zones	**Healthy**	**Strangulation**	**Pre-Strangulation**
μ [kPa]	2.5	3	2.7
k_1^l [kPa]	5.14	7	6
k_2^l [$-$]	1.19	2.1	2
k_1^c [kPa]	0.78	0.9	0.8
k_2^c [$-$]	0.02	0.04	0.03
k_1^d [kPa]	3.65	4	3.66
k_2^c [$-$]	0.31	0.35	0.33
Electrophysiological Parameters (Healthy zone)			
SMC layer		**ICC layer**	
$k_s = 10$	$a_s = 0.06$	$k_i = 7$	$a_i = 0.5$
$\beta_s = 0$	$\lambda_s = 8$	$\beta_i = 0.5$	$\lambda_i = 8$
$\epsilon_s = 0.15$	$\alpha_s = 1$	$\epsilon_i = \epsilon_i(z)$	$\alpha_i = -1$
$D_{si} = 0.3$	$D_s = 0.4$	$D_{is} = 0.3$	$D_i = 0.04$

Remark In the hernia, for the strangulation zone, the diffusion coefficients $D_s^s = 0.1D_s$ and $D_i^s = 0.1D_i$ and in the pre-strangulation, the diffusion coefficients $D_s^{ps} = 0.5D_s$ and $D_i^{ps} = 0.5D_i$.

In the case of severe intestinal hernia, local variations in electrophysiological properties are observed (Misiakos et al., 2014; Keeley et al., 2019; Şimşek et al., 2020). The healthy zone, away from the compression, retains physiological behavior with intact conductivity. The pre-strangulation zone undergoes mechanical stress and partial impairment of blood perfusion, resulting in mild inflammation and edema. These effects locally increase the electrical resistance, modeled by a moderate reduction in the diffusion coefficient. Finally, the strangulation zone is marked by severe ischemia and cellular necrosis. This region is modeled

by a drastic decrease in the diffusion coefficient, representing a significant reduction in the conduction capacity of electrical signals.

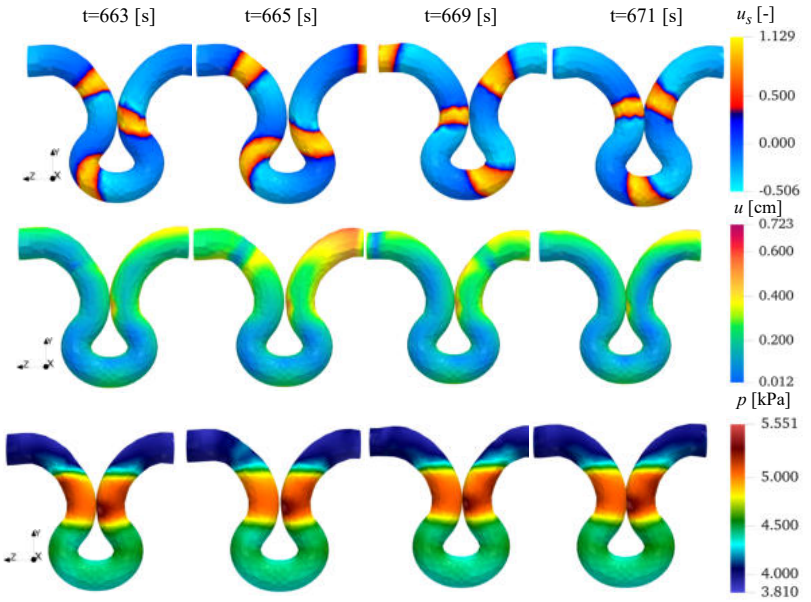

Figure 43: Temporal evolution of SMC transmembrane voltage u_s, hydrostatic pressure p and displacement u for the severe hernia case.

Simulation results for moderate strangulation are provided in Appendix D.1: the electrical wave propagates without significant constraints, allowing almost physiological intestine contraction in the strangulation and pre-strangulation zones. The overall motility of the healthy zone is maintained, thus remaining functional. However, in the case of severe strangulation, Fig. 43, a marked slowing of the electrical wave is observed in the strangulation and pre-strangulation zones, leading to a significant reduction in contraction rate and associated motility.

Manometric measurements in strangulation hernias are technically impossible to perform in clinical conditions due to the severe compression of the intestinal lumen that prevents catheter passage. In our self-contact computational framework, intraluminal pressure levels can be

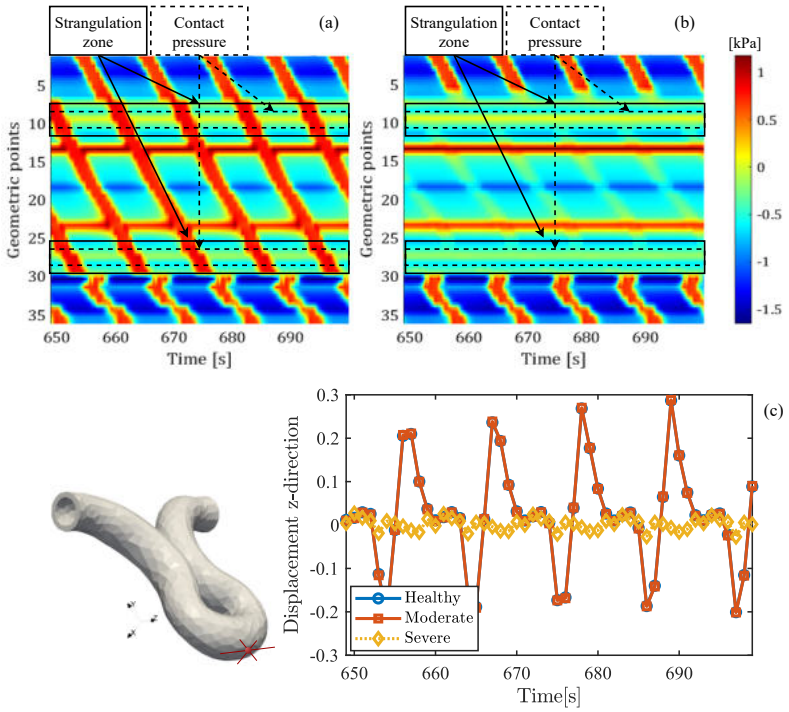

Figure 44: Simulated manometry for (a) moderate and (b) severe hernia cases. Contractions are absent in the strangulated region of the severe case. (c) Time evolution of z-displacement at point $(0,\ -17,\ 19.4)$ for healthy, moderate, and severe configurations.

analyzed for the first time. In the case of moderate strangulation, Fig. 44(a), the manometric curves showed active contraction in the pre-strangulation zone, constant pressure in the strangulation zone (attributed to pressure exerted by contact surfaces), and persistent physiological contraction in the healthy zones. On the other hand, in the case of severe strangulation, Fig. 44(b), the curves also revealed a constant contact pressure in the strangulation zone and absence of contraction due to the contact surfaces, associated with negligible contraction in the pre-strangulation zone. It is worth noticing that, in the severe case, the constant pressure

is more pronounced than in the moderate case. Such high stress is due to the additional load exerted by the abdomen, acting as an external constraint.

To better understand the underlying phenomena, Fig. 44(c) illustrates the displacement in the z-direction within the pre-strangulation zone for three scenarios: healthy, moderate hernia, and severe hernia. For the moderate hernia case, the displacement closely resembles the healthy case, suggesting the onset of a hernia or a very mild condition. On the other hand, in the case of severe hernia, the computed displacement is significantly smaller despite muscle contraction responding to electrical activation. Such a lack of motility can be attributed to the portion of the intestine that has passed through and is constrained by the abdomen.

6.3.5 Modeling intestinal adhesion syndrome

One potential application of our model is the study of intestinal adhesion syndrome (Tabibian et al., 2017), a common condition that arises after surgical interventions or abdominal inflammations. This syndrome is characterized by the formation of fibrous bands, known as adherents, which connect different parts of the intestine or adjacent organs. These adhesions can lead to severe complications such as chronic pain, intestinal obstructions, and impaired intestinal motility (Attard and MacLean, 2007; Strik et al., 2016).

To investigate this phenomenon without directly modeling the adhesions themselves, we based our study on the geometry shown in Fig. 45(a). From this configuration, we aimed to simulate the restrictive effects of adhesions by introducing specialized boundary conditions as show in Eq. 6.5.

$$\boldsymbol{P}\boldsymbol{N} + \eta(r,z) J\boldsymbol{F}^{-T}\boldsymbol{u} + \eta_a J\boldsymbol{F}^{-T}(\boldsymbol{u} - \boldsymbol{u}_{ref}) = 0, \quad \text{on } \partial\Omega \times (0, t_{\text{final}}) \tag{6.5}$$

here, η_a stands for the adherence stiffness (see Fig. 58(b)) while $\boldsymbol{u}_{ref}$ is the initial displacement of the intestinal wall. This approach involves adding a mechanical constraint that replicates the impact of adhesions

on displacements and forces. Through this method, we can examine how local restrictions influence intestinal dynamics while maintaining a general electromechanical framework. Material stiffness changes according to Tab. 6 and the electrophysiology parameter for the healthy case are in the Table 5.

Table 6: Mechanical constitutive parameters for adhesion syndrome simulation

Zones	Healthy	Adherence
μ [kPa]	2.5	3.1
k_1^l [kPa]	5.14	7
k_2^l [−]	1.19	2.1
k_1^c [kPa]	0.78	0.8
k_2^c [−]	0.02	0.04
k_1^d [kPa]	3.65	4
k_2^c [−]	0.31	0.35

Remark For the Adhesion, the diffusion coefficients are $D_s^a = 0.125 D_s$ and $D_i^a = 0.125 D_i$ in the adhesion region.

For this last test case, we present only the pressure maps in Fig. 45(b, c), comparing them with the results from Fig. 38, where adhesion was not considered. At $t = 668$ s, in both cases, self-contact is observed. However, at $t = 671$ s, a clear difference emerges: in the scenario without adhesion, the intestinal surfaces separate due to the peristaltic wave, while in the case with adhesion, the surfaces remain in contact. Such a condition is further confirmed in Fig. 46(b) showing the average absolute displacement between two points located at the adherence region. The absolute displacement is reduced then adhesions are present. Reduced motility is also observed on the manometry curves in Fig. 46(a). In particular, instead of contraction waves, a slight constant pressure appears, indicating the force exerted by the adhesion, forcing the intestinal walls to remain in contact.

To further investigate this condition, we examined the behavior beyond the adhesion zone. Fig. 46(c1) and Figure Fig. 46(c2) display the dis-

placement and action potential at a point located after the adhesion zone. We observe that the action potential is delayed in the case with adhesion, which consequently slows down the contraction speed. However, this does not systematically affect the displacement amplitude. These findings are in perfect agreement with the manometry results.

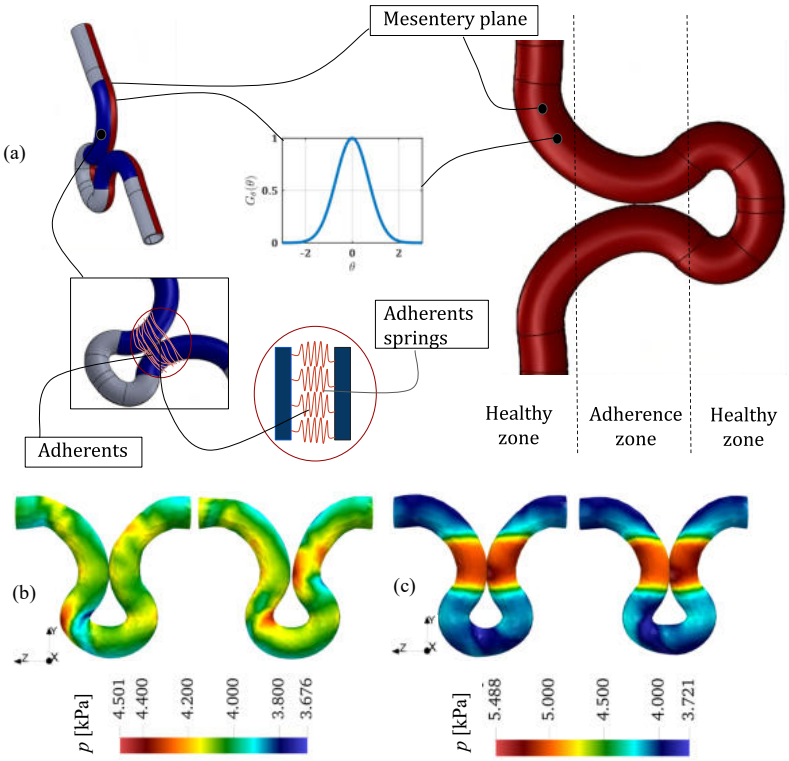

Figure 45: (a) Schematics of the adhesion problem configuration. The mesentery surface is highlighted in red, along with the associated Gaussian distribution of stiffness. Adherents are modeled as distributed springs along the blue boundary. Temporal evolution of the hydrostatic pressure p in the case of severe intestinal adhesion syndrome: (b) without adhesion, and (c) with adhesion, where the material stiffness has been modified in the adhesion region ($\eta_a = 0.9, [\text{kPa/cm}]$, $\boldsymbol{u}_{ref} = 0$). Electrophysiological parameters can be found in Table 5.

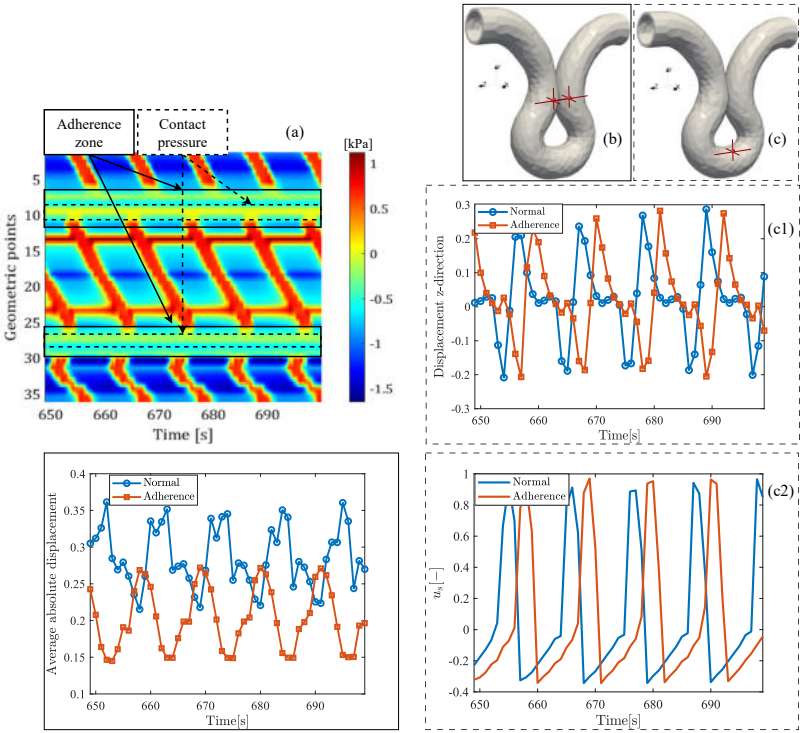

Figure 46: (a) Simulated manometry in the region affected by the adhesion syndrome. No contractions are observed within the adhesion zone. The area labeled Contact pressure indicates pressure levels resulting from self-contact of tissue surfaces.(b) Absolute displacement between two points located within the adhesion region. (c) Comparison between displacement and smooth muscle membrane potential at the point with coordinates $(1.40,\ -14.1,\ 18.9)$ after adherence zone: (c1) membrane potential u_s in the x-direction, (c2) displacement u in the z-direction.

6.4 External devices applications

In this section, a contextual setup is necessary, as we focus on the interaction between the intestinal wall and external medical devices, specifically a distension balloon. The contact model used here corresponds to the second formulation developed earlier in chapter. 3, which is designed to handle the interaction between multiple bodies coming into contact. For the examples presented in this section, the subscripts i and b denote the quantities related to the intestine and the balloon, respectively. Importantly, this model does not require any structural modification, since it has been inherently formulated to capture the mechanical contact between distinct deformable surfaces, allowing us to simulate realistic physiological interactions under various loading and boundary conditions.

6.4.1 Barostatic distension problem

The first numerical test (called Barostatic distension problem) aims to simulate the interaction between the balloon and the intestine during intestinal motility, without considering intestinal self-contact. This simulation is performed on an idealized geometry, where the intestinal diameter is set to 2.8 cm (corresponding to the average physiological range of 2–3 cm), with a length of 20 cm. The balloon, 5 cm in length, is positioned at the center of the intestine. The configuration of the problem is illustrated in Figure 47. During the contraction of the intestine, a progressively increasing pressure is applied to the inner surface of the balloon, allowing it to inflate and exert deformation on the intestinal wall. To prevent numerical instabilities and ensure convergence, the internal balloon pressure is applied incrementally using small time steps, enabling the contact detection algorithm to properly activate the contact constraints. The parameters used for this simulation are provided in the appendix.

The results shown in Figure. 48 demonstrate that when the intestine contracts, it simultaneously compresses the balloon, resulting in a mutual transfer of forces between the two surfaces. This interaction allowed us to compute the intraluminal volume variation, as illustrated in Fig-

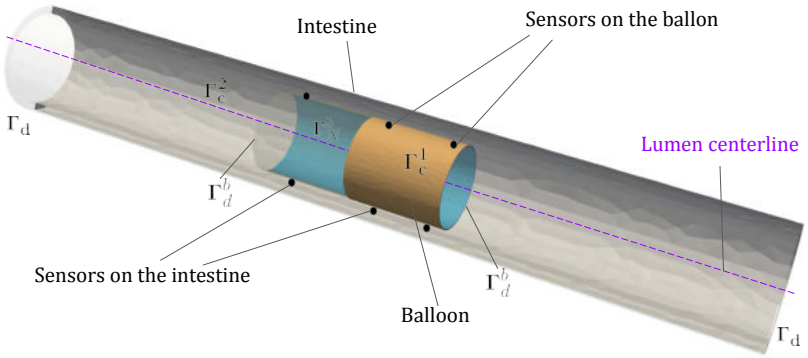

Figure 47: Configuration of the barostatic distension problem. The surfaces Γ_c^1 and Γ_c^2 represent the contact interfaces of the balloon and the intestine, respectively. The surfaces Γ_d and Γ_d^b are used to fix the ends of the intestine and the balloon, respectively. The three points located on the balloon correspond to the positions where contact pressure and contact force data are collected for the balloon, while the points placed on the intestine are used to extract pressure and contact force data on the intestinal wall.

ure. 49.

Furthermore, as time progresses, we observe a progressive increase in the contact force, which can be attributed to the balloon inflation occurring over time. This increase in pressure leads to a reduction in the intestinal contraction rate, a phenomenon also visible in Figure. 49. Over time, this process may impede or even block intestinal contractions, which is consistent with the experimental and numerical observations previously discussed in chapter 4.

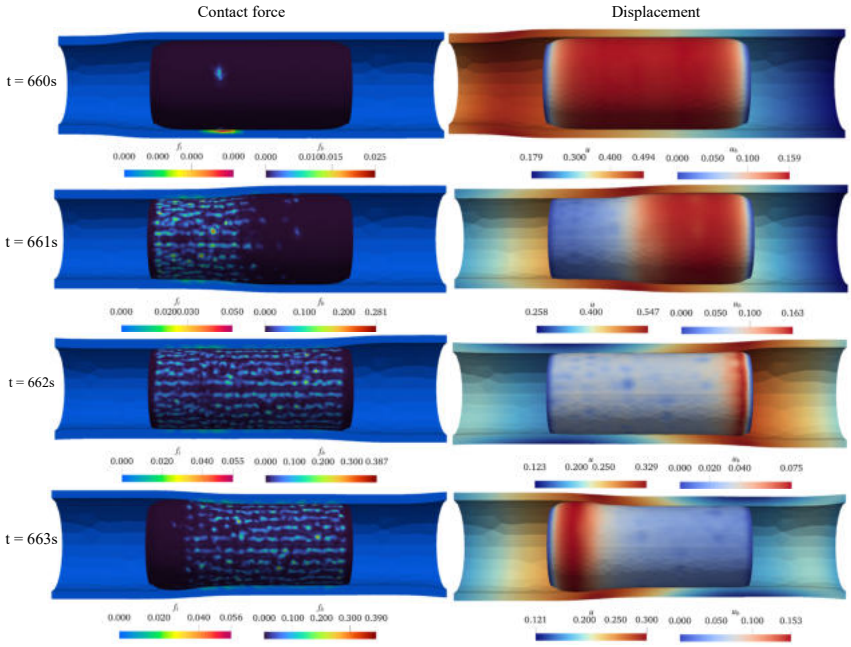

Figure 48: Numerical results of the electromechanics with contact model. The quantities f_i and f_b represent the contact force on the intestine and balloon, respectively, while $\boldsymbol{u}_i$ and $\boldsymbol{u}_b$ represent their displacement.

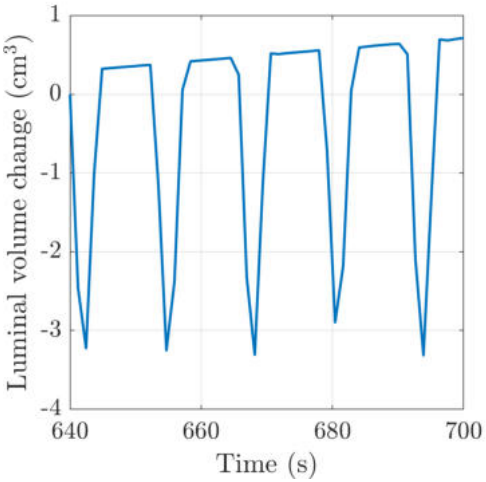

Figure 49: The change in volume of the luminal surface.

6.5 Restoring intestinal lumen

In this section, we investigate how this procedure can be used to simulate a clinical operation commonly performed by physicians. In certain pathological conditions, the intestinal lumen becomes narrowed, preventing normal propagation of luminal contents. To address this issue, physicians often insert a balloon into the intestinal tract, which is then inflated to mechanically restore the lumen and reestablish proper flow. After maintaining inflation for a specific duration, the balloon is deflated and carefully removed.

To replicate this clinical scenario, we extracted a segment of the colon as described in chapter. 4. The central line of the intestinal geometry was then obtained and used to design the balloon in SolidWorks 2013, which was subsequently positioned inside the intestinal lumen using in-house code written in `GetFem` (Yves Renard and Konstantinos Poulios, 2020), as shown in Figure 2. The balloon was then gradually inflated, allowing the intestinal lumen to be restored progressively.

The results in Figure. 50 obtained at t = 50 s, 65 s, and 85 s clearly demonstrate that the balloon is capable of restoring the intestinal lumen, effectively simulating the clinical dilation procedure. This modeling approach also highlights the potential use of such a setup for the deployment of intestinal prostheses.

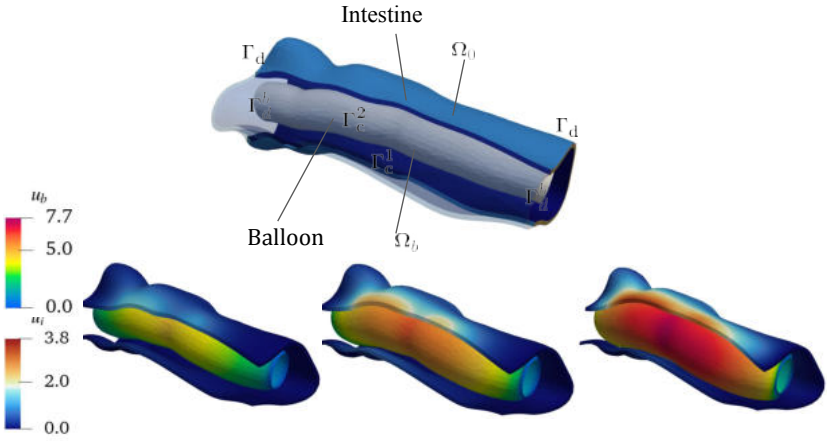

Figure 50: Preliminary result of the restoration of patient-specific colon lumen (still ongoing work). The simulation shows the displacement of the intestine $\boldsymbol{u}_i$ and the balloon $\boldsymbol{u}_b$ at the time 50 s, 65 s, and 80 s, respectively.

6.6 Conclusion

In this chapter, we investigated the electromechanical model by incorporating contact mechanics. The study began with the implementation of self-contact, followed by the extension to multi-body contact. The self-contact model was first validated through a benchmark test, confirming the reliability and accuracy of our algorithm.

From a quantitative perspective, we then analyzed the limitations previously observed in the validation of the manometric curves obtained from the electromechanical model without contact. By introducing self-contact, the model was able to reproduce the manometric profiles and pressure bands that appear in clinical observations.

The enhanced model was subsequently used to the study of pathological cases, including strangulated hernia and adhesion syndrome, showing its ability to capture complex physiological and mechanical interactions. Finally, the multi-body contact formulation was employed to simulate the interaction between the intestine and external medical devices, further highlighting the robustness and versatility of the proposed model in reproducing realistic clinical scenarios.

Chapter 7

Conclusions and future developments

Throughout this study, we have developed a series of methods and techniques to achieve our objectives of modeling, experimenting, and applying an electromechanical framework capable of reproducing the complex behavior of the gastrointestinal system. The work was structured into several chapters, each focusing on a specific aspect—from the mathematical and numerical modeling to experimental validation and clinical application. We introduced novel computational strategies for geometry preparation, electromechanical coupling, and contact mechanics, while also integrating experimental and clinical data to ensure physiological accuracy. These models were then applied to simulate realistic physiological and pathological scenarios, as well as to improve the design and understanding of medical devices. Overall, this thesis provides a comprehensive foundation for linking computational biomechanics with experimental and clinical data, paving the way for more reliable, patient-specific simulations. The following sections provide detailed conclusions and discussions for each chapter, along with the limitations of this work.

7.1 Conclusions

An electromechanical model of the gastrointestinal system was developed, combining electrophysiology, active mechanics, and contact mechanics. This model was constructed following a rigorous methodology to ensure its coherence and scientific validity. In this section, we present a synthesis of the main chapters to highlight the continuity and complementarity between the different stages of our approach—from the formulation of the model to its application in both physiological and pathological cases.

7.1.1 Electrophysiology

This section served as the foundation of our modeling framework, focusing on the electrophysiology of the gastrointestinal (GI) system. To achieve this, we first described the fundamental mechanisms governing GI electrophysiology and identified the two main types of cells responsible for this activity: the Interstitial Cells of Cajal (ICCs) and the Smooth Muscle Cells (SMCs). We then examined the structural organization of these cells at both microscopic and macroscopic scales, as well as their respective roles and interactions.

The ICCs are distributed throughout the intestinal wall, while the SMCs are localized primarily within the smooth muscle layer. When the ICCs are activated, they generate an electrical potential that propagates to the SMCs through gap junctions. Once activated, the SMCs produce a slow-wave electrical activity that maintains the rhythmic movement of the intestine. When this potential exceeds a given threshold, it triggers another type of electrical event known as a spike-burst, which initiates mechanical contraction.

We also showed that effective intestinal contraction requires that ICCs oscillate synchronously at the same frequency. From a modeling perspective, the literature offers two main classes of electrophysiological models: biophysical models and phenomenological models. After reviewing the state of the art and comparing several existing approaches, we adopted the phenomenological model proposed by Aliev, which provides a good

balance between biological accuracy and computational efficiency.

Once the cellular-level model was defined, we extended it to the tissue and organ scales by introducing a diffusion term into the governing equations, allowing the spatial propagation of electrical activity. With this framework established, a series of simulations were performed to calibrate and validate the model. In particular, entrainment analysis and conduction velocity tests were conducted to determine the characteristic timing and frequency of ICC activation, parameters that were essential for coupling the electrophysiological model with the mechanical component.

7.1.2 Active mechanics and contact

In this section, we provide a comprehensive overview of the mechanical modeling developed throughout this thesis. We began by describing the structural organization of the intestine, which consists of multiple layers reinforced by fibers oriented in different directions: longitudinal, circumferential, and symmetric diagonal. This structure naturally defines the intestine as an orthotropic hyperelastic material. From the literature, various modeling approaches exist to describe such materials, ranging from phenomenological models to structure-based and microstructure-based models. In this work, we selected a structure-based model inspired by Holzapfel, which allows the explicit inclusion of four families of fibers (circumferential, longitudinal, and two diagonal fibers) for the anisotropic component, while the isotropic matrix was modeled using a Neo-Hookean formulation. The model parameters were calibrated using a fitting procedure based on uniaxial and inflation test data. Once the material behavior was defined, the equilibrium equations of continuum mechanics were established to model intestinal deformation under the assumption of full incompressibility.

To couple the mechanical model with the previously developed electrophysiological model, we employed the widely used active strain approach. This strategy introduces an intermediate configuration between the reference and current configurations, encapsulating all inelastic phe-

nomena within a single deformation tensor. This tensor includes a structural component accounting for the fiber directions, where only the longitudinal and circumferential fibers were considered active. This allowed the mechanical response to be modulated by the electrophysiological activation function, providing a direct link between electrical activity and contraction.

Given that the intestine is surrounded by other organs and can come into contact with itself during peristaltic motion, a mechanical contact model was incorporated. The initial contact formulation was based on a penalty method, where the gap between surfaces was computed by evaluating the distances from a point on one surface to all points on the opposing surface and vice versa. Due to the computational cost of this approach, we developed an optimized algorithm using a nearest-neighbor search based on a kd-tree, significantly reducing the problem's complexity. To further generalize the approach, a second contact model based on an augmented Lagrangian method was implemented, enabling the simulation of interactions between the intestine and multiple external devices.

Once all components of the model were established, the finite element method was employed to discretize and solve the governing equations. A staggered approach was applied, and a mixed formulation was used to enforce incompressibility and avoid volumetric locking. This mixed formulation simultaneously considers displacements and pressures, which under certain conditions can introduce pressure spikes. To address this, a stabilization term was added to the variational formulation of the problem, ensuring stable and accurate numerical solutions. Tow algorithm was developed to handle the governing equations and implemented in the open source software `FEniCS` and `GetFem`.

7.1.3 Data assimilation

We began by demonstrating how anatomical geometry can be implemented in the numerical model. For this purpose, medical imaging data were segmented using 3D Slicer, from which we extracted a STL file nec-

essary for mesh processing. The geometry was then imported into Meshmixer, where surface cleaning and group separation were performed. The cleaned model was exported again in ASCII-encoded STL format, which facilitated subsequent processing without additional modification. The geometry was then imported into Gmsh, where we defined and labeled the different surfaces with specific tags corresponding to boundary conditions required by the simulations. Once the patient-specific geometry was finalized, we validated this pipeline by solving a Poisson problem, which was necessary to generate the orientation of muscle fibers within the intestinal domain.

Next, we developed a dedicated procedure for extracting the intestinal centerline, which is an essential step for accurately defining the excitability pattern of interstitial cells of Cajal (ICCs). To this end, we prepared an alternative geometry, this time with closed surfaces at both ends, and implemented a custom code based on the VMTK (Vascular Modeling Toolkit) library to extract the centerline from the 3D geometry automatically. This allowed us to capture the natural curvature of the intestinal segment and define spatial variations of activation along its longitudinal axis.

We then described the experimental data collection process, which presented significant technical and logistical challenges. The experiments were conducted at the University of Auckland, following approval from the university's animal ethics committee. In vivo experiments were performed on pigs, under anesthesia, after a laparotomy procedure during which a segment of the intestine was gently exteriorized for study. Multiple types of data were collected, including electrical activity, changes in intestinal volume, and serosa–serosa contact pressure. To measure volume variations, a barostat was used to maintain a constant internal pressure in the balloon while monitoring the volume changes of the intestinal segment. For the measurement of contact pressure between serosal surfaces, we developed a custom-built pressure sensor, specifically designed for these in vivo conditions.

Finally, this chapter concluded with a detailed description of the manometric process, which plays a crucial role in the validation of our numer-

ical model. Manometry provided direct in vivo measurements of pressure propagation and motility patterns along the intestine, allowing us to compare and assess the accuracy of the simulated results against experimental observations.

7.1.4 Applications

A comprehensive multiphysics modeling framework was proposed, combining active strain electromechanics , tissue anisotropy, and cellular electrophysiology. For the colonic case, the model enabled the characterization of contractility in the presence of bio-printed deposited materials (e.g., via LTS procedures) assumed to bond perfectly with the surrounding healthy tissue. The numerical solution was achieved through a hybrid finite element scheme: a monolithic coupling for the electrophysiological component and a staggered scheme for the electromechanical coupling implemented in open source `FEniCS` and `GetFem`. An extensive calibration phase was performed to ensure the robustness of the in silico model, validated through several benchmark tests, including: (i) transmembrane action potential conduction velocity; (ii) entrainment frequency and stability of ICCs and SMCs temporal dynamics; (iii) fine-tuning of strain energy material parameters from multiaxial experimental data.

After this validation phase, the developed model was employed to investigate the effect of a laser-welded patch material on the motility of the colon. We first validated the model by comparing manometric curves obtained from simulations with those measured in clinical settings, ensuring the reliability of the predicted motility patterns. Once validated, we conducted a parametric study of the patch, focusing on its size and composition. It was observed that the size of the patch had only a minor influence on the motility response, whereas its mechanical and electrophysiological properties played a much more significant role. The patch was modeled as a neo-Hookean material, whose stiffness could either exceed or fall below that of healthy tissue. The simulations revealed that the critical case corresponded to a patch stiffer than the

surrounding intestinal wall. Therefore, our subsequent analyses focused on this scenario, in which we systematically varied the electrical conductivity and contractility of the patch. These analyses demonstrated that reduced electrical coupling and excessive stiffness led to the most pronounced disruptions in coordinated peristaltic waves. The model was also applied to a realistic duodenal geometry, confirming its capability to reproduce physiological motility patterns under realistic conditions.

Despite the successful validation (to some extend) through high-resolution manometry, where the model was able to reproduce the propagating contraction waves, a discrepancy remained. Specifically, clinical manometry recordings often exhibited horizontal pressure bands that were absent in our initial simulations. To address this limitation, we introduced a self-contact model into the numerical framework. This self-contact formulation was an unbiased penalty-based approach, where the gap function was computed as the Euclidean distance between nodes belonging to opposing surfaces. Since this computation is typically time-consuming, we implemented an optimized nearest-neighbor search algorithm based on a kd-tree structure, significantly reducing computational cost. Once the self-contact mechanism was integrated, the simulated manometric patterns exhibited the horizontal pressure bands observed in clinical data, thereby improving the physiological realism of the model.

Recognizing that the intestine is surrounded by various neighboring organs, we further developed a special boundary condition to account for the mechanical influence of adjacent structures. This boundary condition introduced a nonlinear stiffness distribution along the intestinal wall, modeled using Gaussian-type spatial functions, allowing us to realistically simulate organ confinement effects. The new model was first validated using a benchmark contact test, confirming the robustness of the formulation, and then further verified through manometric comparison, which demonstrated its improved accuracy in reproducing clinical pressure patterns. Consequently, this enhanced model provided a valuable tool to investigate pathological conditions, such as strangulated hernias and post-surgical adhesion syndromes, where contact and compression play crucial roles.

To further generalize the contact formulation, we extended the model to handle multiple interacting bodies and complex convex contact surfaces. This was achieved using an augmented Lagrangian approach, in which the gap computation was performed using a ray-tracing algorithm. This extension significantly broadened the applicability of our framework and enabled the simulation of clinically relevant interactions, in particular, the insertion and inflation of a balloon catheter within the intestine during peristalsis. This case was especially important, as it provided another means of experimental validation, using balloon inflation tests conducted at the University of Auckland. The agreement between the simulated and experimental data further confirmed the accuracy and robustness of our electromechanical and contact coupling framework.

Ultimately, this work represents, to the best of our knowledge, the first in silico prediction of intestinal electromechanical motility in curved three-dimensional geometries prone to self-contact. The developed model opens promising perspectives for the analysis and prediction of intestinal motility across a wide range of clinical situations, offering a virtual tool to support diagnosis, surgical planning, and the assessment of implantable medical devices.

7.2 Limitations and perspectives

7.2.1 Limitations

Despite the promising results and the broad applicability of the developed framework, several limitations remain, both in the electrophysiological and mechanical components of the model.

From the electrophysiological perspective, the model is currently capable of generating only a single type of wave, namely the slow wave, as it does not incorporate the variability necessary to reproduce both slow waves and spike bursts, the latter typically resulting from neuronal activation. Moreover, the electrical propagation occurs in a single direction, whereas in physiological observations, intestinal activity frequently exhibits anterograde, retrograde, or even simultaneous bidirec-

tional waves. This limitation arises from the absence of the enteric nervous system in the formulation, which in reality introduces the stochastic behavior and wave coordination observed in vivo.

On the mechanical side, the model still relies on a neo-Hookean formulation for the extracellular matrix, which, although computationally convenient, may not fully capture the nonlinear anisotropic response of intestinal tissue. Additionally, the active strain formulation currently assumes an identical contractility for both longitudinal and circumferential fiber families at each point. This simplification neglects the physiological interplay between these directions — during peristalsis, longitudinal contraction should be accompanied by circumferential relaxation, and vice versa.

Another important limitation lies in the experimental integration. Although in vivo data were collected during animal experiments, the number of usable data points was limited, and it was not possible to fully validate the model against experimental measurements. The scarcity and partial nature of the data prevented a robust quantitative validation of the experimental protocol itself.

Finally, the model does not explicitly represent the intestinal content. Instead, the chyme was idealized as a uniform internal pressure applied to the luminal surface. While this simplification allowed us to study wall mechanics and peristaltic motion efficiently, it does not capture the fluid–structure interactions or the complex viscous effects associated with real chyme transport.

7.2.2 Perspectives

In future, we plan to extend the model presented in chapter. 2 by introducing neuronal regulation, which plays a crucial role in differentiating not only the type of electrical waves but also the resulting motility patterns of the intestine. To this end, we will implement two complementary approaches: (i) Chaos-based neuronal coupling. we will propose to couple Eq. 2.1.1 with a neuronal model of the Hindmarsh–Rose type (Innocenti and Genesio, 2009). This class of models has the ability to ex-

hibit multistability in certain regions of the phase space, allowing for the coexistence of multiple waveforms. In particular, it can generate both bursting activity and spike trains, which represent a hallmark of intestinal electrophysiology. The electrical signals obtained from this model will be regularized and coupled with the existing framework, thereby introducing additional stochasticity and enabling the representation of neuronal control. An additional advantage of this approach is its relatively low dimensionality, which makes it straightforward to implement. (ii) Biophysical modeling with neuronal input. Alternatively, we will build upon existing biophysically inspired electrophysiological models, which typically neglect neuronal regulation. Recently, a new formulation was proposed that incorporates enteric neuronal stimulation, successfully predicting its effects on slow-wave activity (Athavale, Avci, et al., 2024b). However, this model did not capture the coexistence of different wave types. Starting from this formulation, we intend to identify and derive the relevant quantities required to reproduce and synchronize the coexistence of slow waves and spike-burst activity within the intestinal wall.

For the mechanical modeling of the intestinal tissue, I plan to develop a distribution function that will allow us to differentiate not only the individual layers but also the distinct fiber orientations within each layer. This will provide a more physiologically realistic representation of the anisotropic structure of the gastrointestinal wall.

Moreover, we aim to introduce an additional level of complexity by explicitly modeling the presence of food within the intestine, treating it as a highly viscous fluid. To the best of our knowledge, a few models of this type have been developed to simulate the transport of food in the stomach (Palmada, Cater, et al., 2023; Palmada, Hosseini, et al., 2023). However, in these studies, contractions were imposed, and the fluid–structure coupling was considered only in one direction, where tissue deformation influenced the fluid but not vice versa.

In contrast, we plan to implement a fully coupled fluid–structure in-

teraction (FSI) model, in which the bidirectional interplay between intestinal wall contraction and fluid dynamics is captured. Furthermore, a porosity model will be incorporated to represent the filtration of nutrients through the intestinal wall (Taffetani, Ricardo Ruiz-Baier, and Waters, 2021), thereby providing a more comprehensive description of gastrointestinal function.

Appendix A

Calibration and estimation of mechanical parameters

Some parts of this appendix are taken from author's previous publications (Djoumessi, Lenarda, Alessio Gizzi, Giusti, et al., 2024; Djoumessi, Lenarda, Alessio Gizzi, and Paggi, 2025).

To calibrate our passive material model and associated code, we undertook a series of tests to calibrate the model parameters. These tests include a uniaxial test based on Nagaraja data (Nagaraja et al., 2021), and a triaxial test using cylinder occlusion based on Sokolis data (Sokolis and Sassani, 2013). We would like to point out that as we did not have the original experimental data, we were content to validate part of the authors' experimental curve. To this end, we have extracted data from their figure to use it as a reference. About the uniaxial test, most of the parameters were taken from Nagaraja et al. (2021) study, which we then used as a basis for approximating certain points in Sokolis and Sassani (2013) experimental data.

We began by attempting to reproduce Nagaraja's experimental results with our model. To this end, we performed a uniaxial test aimed at reproducing Nagaraja's experimental results for the case where β (the cutting angle of the sample.) is equal to $90°$. This test was performed for

the maximum and minimum values of the parameters, and some parameters were adjusted to approximate the experimental values. Figure 51 below illustrates the comparison between the model and the experimental. We can see that the model comes closer to the experimental curve for the minimum parameters. This shows that these parameters can be used without causing errors in the code. The calibrated data are summarised in the following table7.

To be more consistent about the model's performance, we carried out a

Table 7: Table of Material used for the uni-axial test (Nagaraja et al., 2021)

sets	$\mu[kPa]$	$k_1^l[kPa]$	$k_2^l[-]$	$k_1^c[kPa]$	$k_2^c[-]$	$k_1^d[kPa]$	$k_2^d[-]$	$\theta[\circ]$
max	5	77.35	1.04	0.95	0.06	7.38	0.6	39.78
min	5	5.14	1.19	0.78	0.02	3.65	0.31	38.18

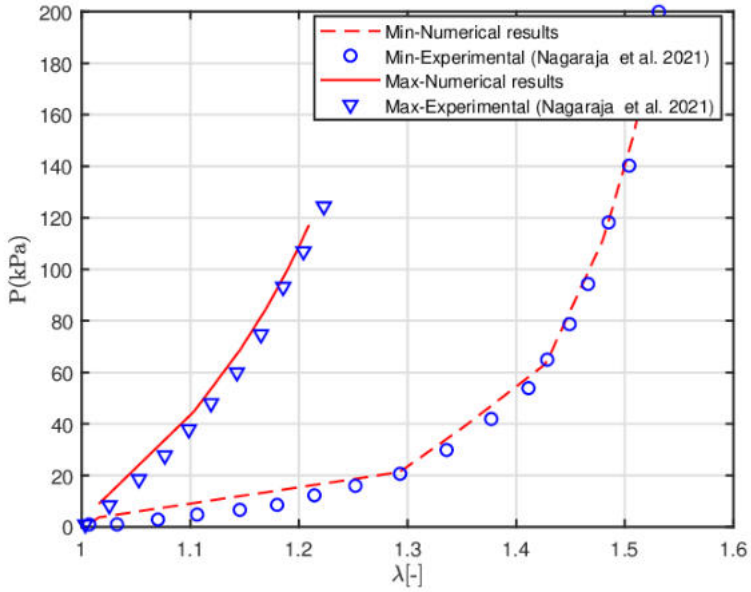

Figure 51: Comparison between simulation of the uni-axial test and experimental data.

carefully calibrated inflation test. As shown in the figure 52, a $3.5\ cm$ long cylinder was used for this purpose (Sokolis and Sassani, 2013). Pressure was applied to the inner surface of the cylinder, while both ends were clamped. After each inflation, the parameters were carefully adjusted to reproduce the experimental data faithfully and to extract the outer radius. The agreement between the model and the experimental data from (Sokolis and Sassani, 2013) is clearly demonstrated in the figure below. The parameters obtained after calibration are detailed in Table 8. These data will be crucial for all future simulations.

It is important to note that, for both cases considered, we sought to minimize a cost function. For the uniaxial and biaxial tests, the cost function was defined as $\mathrm{Cos} = \sqrt{(P_{\mathrm{exp}} - P_{\mathrm{num}})^2 / P_{\mathrm{exp}}^2}$, where P denotes the first Piola–Kirchhoff stress, either experimentally measured or numerically computed. For the inflation test, the cost function used was $\mathrm{Cos} = \sqrt{(p_{\mathrm{exp}} - p_{\mathrm{num}})^2 / p_{\mathrm{exp}}^2}$, where p corresponds to the intraluminal pressure. In all cases, a very good agreement between experimental and numerical data was obtained, with a consistently high correlation coefficient for each test.

Table 8: Table of Material used for the three-axial test

params	$\mu[kPa]$	$k_1^l[kPa]$	$k_2^l[-]$	$k_1^c[kPa]$
values	2.5	5.4324	1.19	0.78
params	$k_2^c[-]$	$k_1^d[kPa]$	$k_2^d[-]$	$\theta[\circ]$
values	0.02	3.65	0.31	39.5

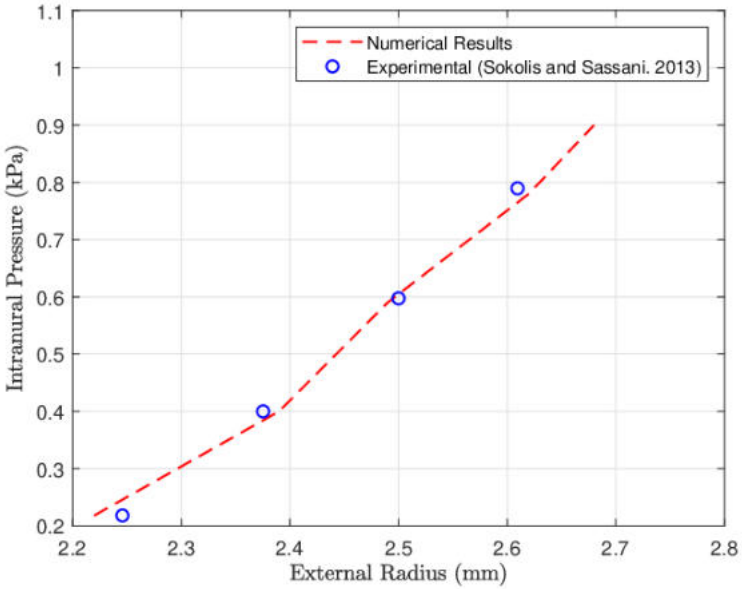

Figure 52: Comparison between simulation of the three-axial test and experimental data.

Appendix B

Fiber generation procedure

Some parts of this appendix are taken from author's previous publications (Djoumessi, Lenarda, Alessio Gizzi, Giusti, et al., 2024; Djoumessi, Lenarda, Alessio Gizzi, and Paggi, 2025).

We start by the configuration show in Figure 53. The curvilinear coordinates are obtained by solving the stationary modified scalar diffusion with the corresponding boundary conditions.

$$\nabla^2 \zeta = 0 \quad on \quad \Omega_0 \tag{B.1a}$$

$$\zeta = \zeta_0 \quad on \quad \partial\Gamma_D \tag{B.1b}$$

$$\boldsymbol{n} \cdot \nabla \zeta = 0 \quad on \quad \partial\Gamma_N \tag{B.1c}$$

where ζ is an arbitrary scalar field, ζ_0 is the value prescribed on the Dirichlet boundary ($\partial\Gamma_D$), and $\boldsymbol{n}$ is the unit vector of the surface normal. The discrete longitudinal vector field $\nabla\zeta_z$ is obtained by solving Eqs. B.1 with the Neumann boundary condition prescribed on the inner and outer surfaces, together with the Dirichlet boundary condition prescribed on both end surfaces as shown in Figure. 53. The final longitudinal fiber direction is obtained by the normalisation $\boldsymbol{n}_l = \nabla\zeta_z / \|\nabla\zeta_z\|$. The radial vector direction $\boldsymbol{n}_r$ is obtained similarly, only the Neumann and Dirichlet boundary conditions must be interchanged. Then, the circumferential fiber direction $\boldsymbol{n}_c$ is defined as a cross product of the unitary

radial and longitudinal vector fields, $\boldsymbol{n}_r$ and $\boldsymbol{n}_l$. Regarding the helical fiber direction, two additional parameters are necessary, a unit vector $\boldsymbol{r}_0$ aligned with the centreline and the angle θ that will determine the rotational anisotropy from the circumferential direction. Once the radial direction has been computed, we project the centreline on the normal direction and compute the so-called flat fiber field $\boldsymbol{r}_f$(Ruiz-Baier et al., 2020). Then the diagonal fibers are obtained by using the Rodrigues rotation formula.

$$\boldsymbol{n}_{d1} = \boldsymbol{r}_f \cos(\theta) + (\boldsymbol{n}_l \times \boldsymbol{r}_f) \sin(\theta) + \boldsymbol{n}_l(\boldsymbol{n}_l \cdot \boldsymbol{r}_f)(1 - \cos(\theta)) \tag{B.2}$$

a similar expression can be derived for $\boldsymbol{n}_{d2}$.

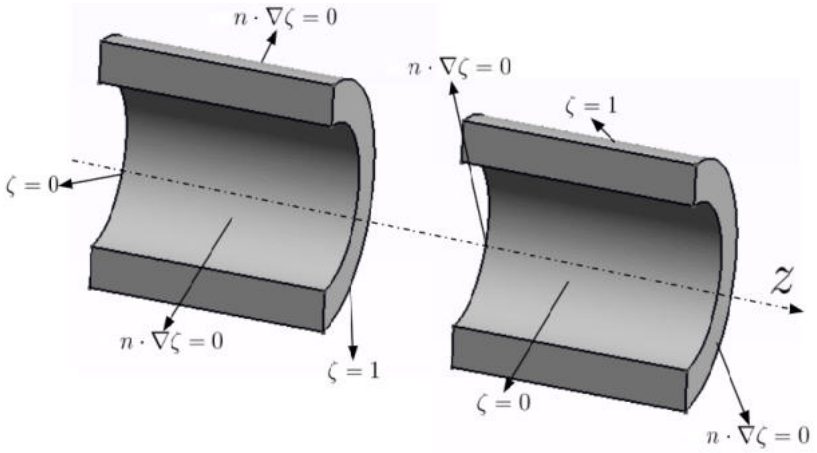

Figure 53: Configuration used to compute fiber orientation in the colon, left represents the configuration for the longitudinal fibers and right the configuration for the radial fibers.

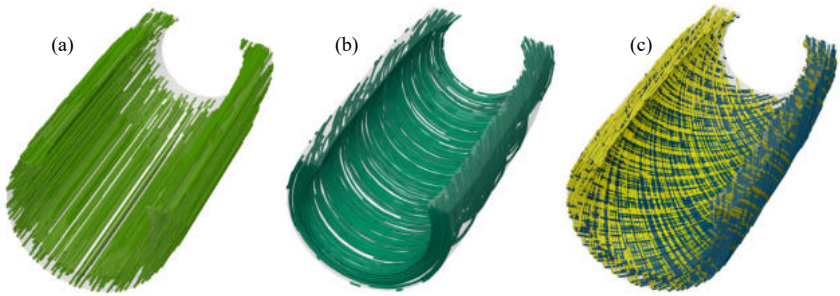

Figure 54: Result of the fiber structure used for all simulations (a) the longitudinal fiber, (b) circumferential fibers, and (c) the diagonal fibers. All the fiber families are homogenised throughout all the thicknesses.

B.1 Zoomed clip of the region of interest where the patch is located

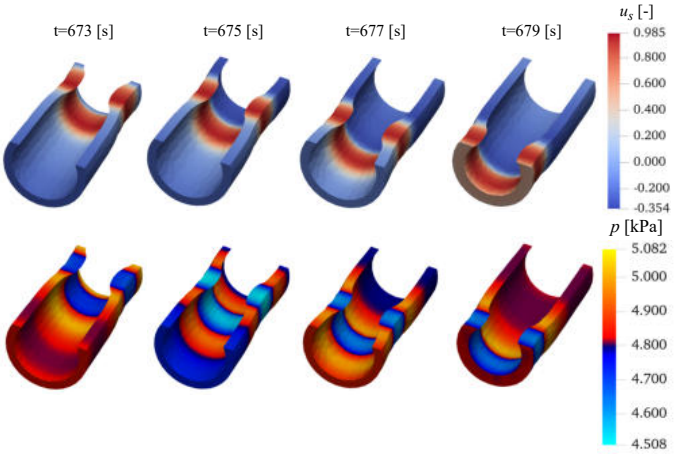

Figure 55: Temporal evolution of the hydrostatic pressure p, the action potential in the smooth muscle layer u_s, and the longitudinal and circumferential fibers distribution in the deformed domain corresponding to healthy condition ($\mu_p = \mu_t$).

B.2 Numerical solution of the nonlinear diffusivity

Note: Some parts of this appendix are taken from author's previous (Djoumessi, Lenarda, Alessio Gizzi, Giusti, et al., 2024; Djoumessi, Lenarda, Alessio Gizzi, and Paggi, 2025).

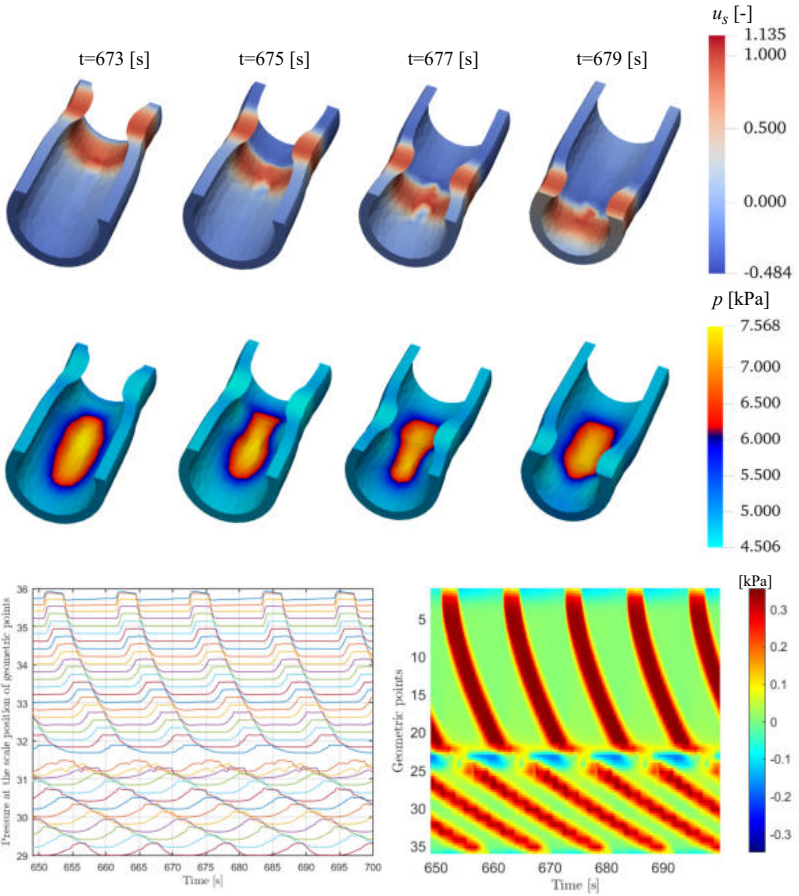

Figure 56: Temporal evolution of hydrostatic pressure p and the action potential in the smooth muscle layer u_s in a region around an elliptical geometry of radii $r_{\max} = 3$ and $r_{\min} = 2$ with stiffness $\mu_p = 2\mu_t$ and the diffusion coefficients $D_s^p = 0.01 D_s$ and $D_i^p = 0.01 D_i$. HRM map with $\mu_p = 2\mu_t$ with in-homogeneous diffusivity $D_s^p = 0.01 D_s$ and $D_i^p = 0.01 D_i$

Appendix C

Application to the problem setting

Note: Some parts of this appendix are taken from author's previous (Djoumessi, Lenarda, Alessio Gizzi, Giusti, et al., 2024; Djoumessi, Lenarda, Alessio Gizzi, and Paggi, 2025).

After testing our contact code on the benchmark problem, we proceeded to integrate the contact code into the full electromechanical framework and solved the problem on the geometry described in Fig. 35 using the mechanical problem explained in Eq. 3.28.

We observe in Fig. 57 that the contact code effectively prevents interpenetration between the contact surfaces. This is particularly evident in the pressure curves, which show an increase in pressure at the contact regions when the surfaces come into contact, notably at t=667s and t=669s. This confirms that the implemented code successfully handles the contact between the two surfaces. This result was used as a reference for the rest of the simulation

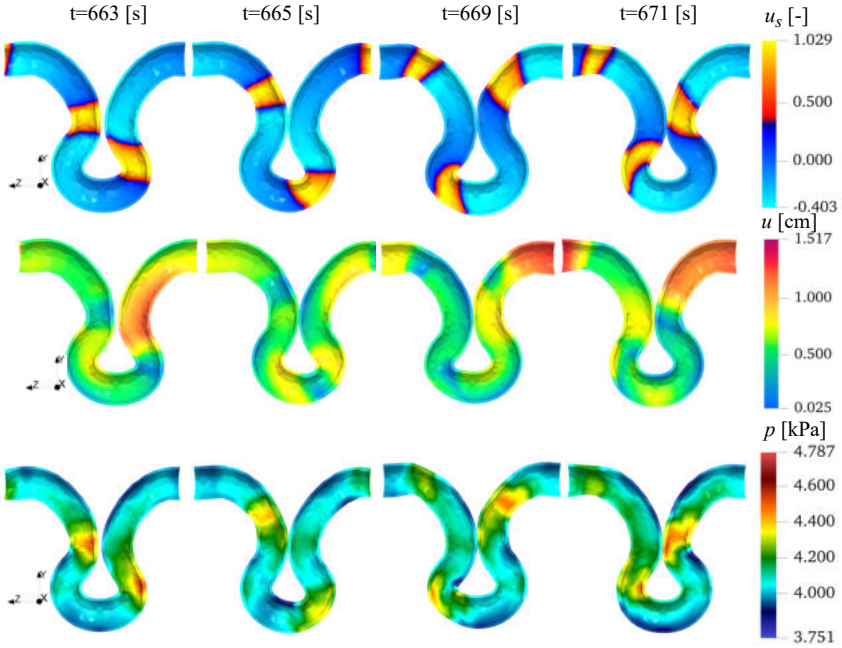

Figure 57: Temporal evolution of SMC transmembrane voltage u_s, of hydrostatic pressure p and the displacement u for the Euclidean distance method

Appendix D

Distribution of the stiffness for Robin BC used in all simulations

Note: Some parts of this appendix are taken from author's previous (Djoumessi, Lenarda, Alessio Gizzi, Giusti, et al., 2024; Djoumessi, Lenarda, Alessio Gizzi, and Paggi, 2025).

This section illustrates the distribution of stiffness $\eta(r, s)$ across a surface of the geometry and the additional stiffness η_a, which accounts for the effects of adhesions. Since the stiffness $\eta(r, s)$ represents the influence of the mesentery, it was included in all simulations. On top of this baseline stiffness, an additional stiffness was introduced solely in the presence of adhesions to simulate the case of the adhesion syndrome.

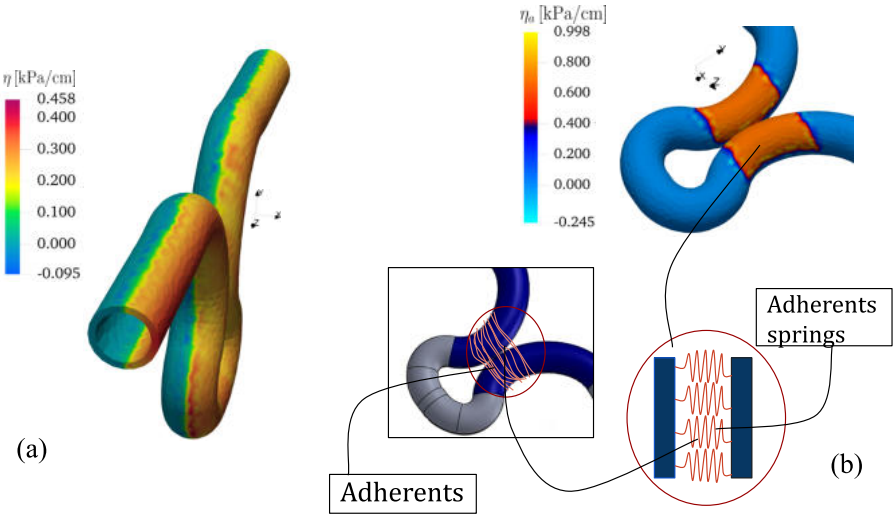

Figure 58: (a) distribution of the stiffness η representing the effect of mesentery and (b) shows the distribution of the stiffness η_a showing the effect of the adherents.

D.1 Result for the moderate Hernia

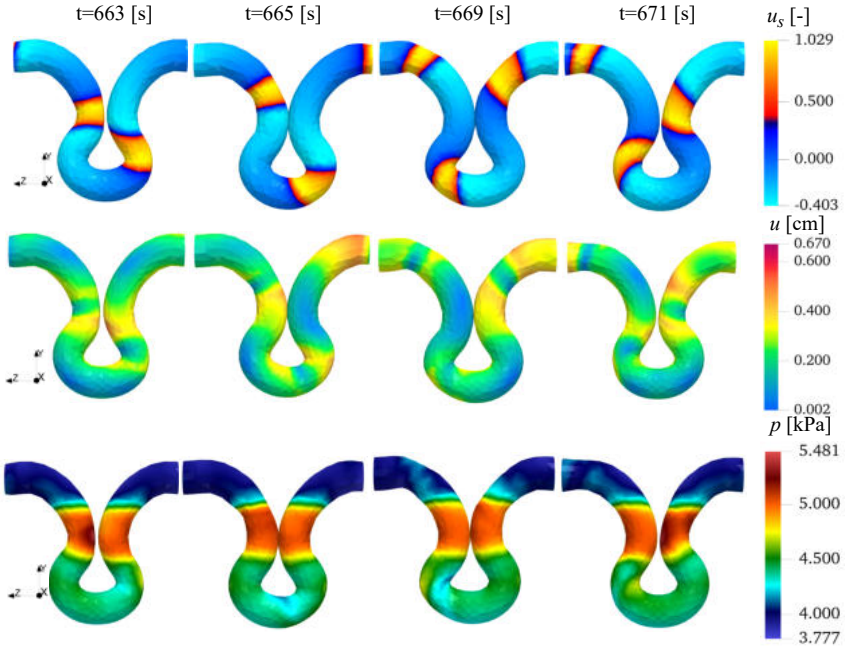

Figure 59: Temporal evolution of SMC transmembrane voltage u_s, hydrostatic pressure p and displacement u for the moderate hernia case.

Bibliography

Ackerman, Michael J (2002). "The visible human project". In: *Proceedings of the IEEE* 86.3, pp. 504–511.

Alduini, Pietro (2021). *Endoscopic system*. WO2021152530A1.

Aliev, Rubin R, William Richards, and John P Wikswo (2000). "A simple nonlinear model of electrical activity in the intestine". In: *Journal of Theoretical Biology* 204.1, pp. 21–28.

Alnæs, Martin et al. (2015). "The FEniCS project version 1.5". In: *Archives of Numerical Software* 3.100.

Ambrosi, Davide et al. (2011). "Electromechanical coupling in cardiac dynamics: the active strain approach". In: *SIAM J. Appl. Math.* 71.2, pp. 605–621.

Arbizu, Ricardo A et al. (2017). "Prospective evaluation of same day versus next day colon manometry results in children with medical refractory constipation". In: *Neurogastroenterology & Motility* 29.7, e13050.

Ashbell, Ido et al. (2023). "Laser tissue soldering of the gastrointestinal tract: A systematic review LTS of the gastrointestinal tract". In: *Heliyon*.

Athavale, Omkar N, Recep Avci, et al. (Jan. 2024a). "Neural regulation of slow waves and phasic contractions in the distal stomach: a mathematical model". In: *Journal of Neural Engineering* 20.6, p. 066040. DOI: 10.1088/1741-2552/ad1610. URL: https://dx.doi.org/10.1088/1741-2552/ad1610.

— (2024b). "Neural regulation of slow waves and phasic contractions in the distal stomach: a mathematical model". In: *Journal of Neural Engineering* 20.6, p. 066040.

Athavale, Omkar N, Madeleine R Di Natale, et al. (2024). "Mapping the rat gastric slow-wave conduction pathway: bridging in vitro and in vivo methods, revealing a loosely coupled region in the distal stom-

ach". In: *American Journal of Physiology – Gastrointestinal and Liver Physiology* 327.2, G254–G266.
Athavale, Omkar N, Niranchan Paskaranandavadivel, et al. (2020). "Design of pressure sensor arrays to assess electrode contact pressure during in vivo recordings in the gut". In: *2020 42nd Annual International Conference of the IEEE Engineering in Medicine & Biology Society (EMBC)*. IEEE, pp. 4204–4207.
Attard, Jo-Anne P and Anthony R MacLean (2007). "Adhesive small bowel obstruction: epidemiology, biology and prevention". In: *Canadian Journal of Surgery* 50.4, p. 291.
Azzouz, Laura L and Sandeep Sharma (2018). *Physiology, Large Intestine*. Treasure Island (FL): StatPearls Publishing.
Baker, Salah A et al. (2025). "Novel imaging approach for simultaneous tracking of cell dynamics in distinct tissue layers reveals cells involved in colonic peristalsis". In: *Frontiers in Imaging* 4, p. 1538533.
Basov, Svetlana et al. (2019). "Strong bonding of corneal incisions using a noncontact fiber-optic laser soldering method". In: *Journal of Biomedical Optics.* 24.12, pp. 128002–128002.
Birkelbach, Moritz Alexander et al. (2020). "In vitro feasibility analysis of a new sutureless wound-closure system based on a temperature-regulated laser and a transparent collagen membrane for laser tissue soldering (LTS)". In: *International Journal of Molecular Sciences.* 21.19, p. 7104.
Bozorgmehri, Babak et al. (2021). "A study of contact methods in the application of large deformation dynamics in self-contact beam". In: *Nonlinear Dynamics* 103, pp. 581–616.
Brandstaeter, Sebastian et al. (2018). "Computational model of gastric motility with active-strain electromechanics". In: *ZAMM – Journal of Applied Mathematics and Mechanics* 98.12, pp. 2177–2197.
Buist, ML et al. (2006). "Multiscale modelling of human gastric electric activity: can the electrogastrogram detect functional electrical uncoupling?" In: *Experimental physiology* 91.2, pp. 383–390.
Byrnes, Kevin Gerard et al. (2019). "Anatomy of the mesentery: Current understanding and mechanisms of attachment". In: *Seminars in Cell & Developmental Biology*. Vol. 92. Elsevier, pp. 12–17.
Cardoz, Althea V et al. (2024). "Acute Intestinal Obstruction Due to Obturator Hernia: A Case Series". In: *Cureus* 16.4.
Center, Memorial Sloan Kettering Cancer (2023). *About Your Abdominal Incisional Hernia Surgery*. Accessed on 2024-12-06. URL: `https://`

www.mskcc.org/cancer-care/patient-education/about-your-abdominal-incisional-hernia-surgery.
Chadi, Sami A et al. (2016). "Emerging trends in the etiology, prevention, and treatment of gastrointestinal anastomotic leakage". In: *Journal of Gastrointestinal Surgery.* 20, pp. 2035–2051.
Chavan, Kishor S, Bishnu Prasad Lamichhane, and Barbara I Wohlmuth (2007). "Locking-free finite element methods for linear and nonlinear elasticity in 2D and 3D". In: *Computer Methods in Applied Mechanics and Engineering* 196.41-44, pp. 4075–4086.
Cherubini, C et al. (2008). "An electromechanical model of cardiac tissue: Constitutive issues and electrophysiological effects". In: *Progress in Biophysics and Molecular Biology* 97.2-3, pp. 562–573.
Chirianni, F, G Vairo, and M Marino (2024). "Development of process design tools for extrusion-based bioprinting: From numerical simulations to nomograms through reduced-order modeling". In: *Computer Methods in Applied Mechanics and Engineering* 429, p. 116685.
Choudhury, Susanta (2013). "Stress analysis of thick walled cylinder". PhD thesis.
Conklin, Jeffrey, Mark Pimentel, and Edy Soffer (2009). *Color atlas of high resolution manometry*. Springer.
Corrias, Alberto and Martin L Buist (2007). "A quantitative model of gastric smooth muscle cellular activation". In: *Annals of Biomedical Engineering.* 35, pp. 1595–1607.
— (2008). "Quantitative cellular description of gastric slow wave activity". In: *American Journal of Physiology – Gastrointestinal and Liver Physiology.* 294.4, G989–G995.
Corrias, Alberto, Peng Du, and Martin L Buist (2013). "Modelling Tissue electrophysiology in the GI tract: past, present and future". In: *New Advances in Gastrointestinal Motility Research*, pp. 167–195.
Djoumessi, René Thierry, Pietro Lenarda, Alessio Gizzi, Simone Giusti, et al. (2024). "In silico model of colon electromechanics for manometry prediction after laser tissue soldering". In: *Computer Methods in Applied Mechanics and Engineering* 426, p. 116989. ISSN: 0045-7825.
Djoumessi, René Thierry, Pietro Lenarda, Alessio Gizzi, and Marco Paggi (2025). "A self-contact electromechanical framework for intestinal motility". In: *Computational Mechanics*. ISSN: 1432-0924. DOI: 10.1007/s00466-025-02692-4. URL: https://doi.org/10.1007/s00466-025-02692-4.

Drouet, Guillaume (2017). "Salome-Meca: une plate-forme au service de la simulation mécanique". In: *13e colloque national en calcul des structures*.

Du, Peng, Stefan Calder, et al. (2018). "Progress in mathematical modeling of gastrointestinal slow wave abnormalities". In: *Frontier in Physiology* 8, p. 1136.

Du, Peng, Jeelean Lim, and Leo K Cheng (2013). "A model of electromechanical coupling in the small intestine". In: *Multiscale Computational Modeling in Biomechanics and Biomedical Engineering*, pp. 179–207.

Du, Peng, Greg O'Grady, et al. (2010). "Multiscale modeling of gastrointestinal electrophysiology and experimental validation". In: *Critical Reviews™ in Biomedical Engineering* 38.3.

Faville, RA et al. (2008). "A biophysically based mathematical model of unitary potential activity in interstitial cells of Cajal". In: *Biophysical journal* 95.1, pp. 88–104.

Fedorov, Andriy et al. (2012). "3D Slicer as an image computing platform for the Quantitative Imaging Network". In: *Magnetic resonance imaging* 30.9, pp. 1323–1341.

Frager, David et al. (1996). "Detection of intestinal ischemia in patients with acute small-bowel obstruction due to adhesions or hernia: efficacy of CT." In: *AJR. American Journal of Roentgenology* 166.1, pp. 67–71.

Fung, Candice and Pieter Vanden Berghe (2020). "Functional circuits and signal processing in the enteric nervous system". In: *Cellular and Molecular Life Sciences* 77.22, pp. 4505–4522.

Furtado, TA, AC Carvalho, and DPC Garcia (2024). "Estrangulated obturatory hernia. Case report of a challenging diagnosis of obstructive syndrome". In: *International Journal of Surgery Case Reports*, p. 109643.

Gerasimenko, Alexander Yu et al. (2022). "Reconstruction of soft biological tissues using laser soldering technology with temperature control and biopolymer nanocomposites". In: *Bioengineering* 9.6, p. 238.

Geuzaine, Christophe and Jean-François Remacle (2009). "Gmsh: A 3-D finite element mesh generator with built-in pre-and post-processing facilities". In: *International journal for numerical methods in engineering* 79.11, pp. 1309–1331.

Girardeau-Montaut, Daniel et al. (2016). "CloudCompare". In: *France: EDF R&D Telecom ParisTech* 11.5, p. 2016.

Gizzi, A, C Cherubini, S Migliori, et al. (2010). "On the electrical intestine turbulence induced by temperature changes". In: *Physical Biology* 7.1, p. 016011.

Gizzi, A, C Cherubini, N Pomella, et al. (2012). "Computational modeling and stress analysis of columellar biomechanics". In: *Journal of the Mechanical Behavior of Biomedical Materials* 15, pp. 46–58.

Gizzi, Alessio et al. (2015). "Theoretical and numerical modeling of nonlinear electromechanics with applications to biological active media". In: *Communications in Computational Physics* 17.1, pp. 93–126.

Han, W. et al. (2024). "Nonlinear NMM analysis for large deformation and contact problems: Using full strain-rotation decomposition algorithm and augmented Lagrangian method enhanced open-closed iteration". In: *Engineering Analysis with Boundary Elements* 169, p. 105971.

Hanani, Menachem, Gianrico Farrugia, and Terumasa Komuro (2005). "Intercellular coupling of interstitial cells of Cajal in the digestive tract". In: *International Review of Cytology* 242, pp. 249–282.

Helander, Herbert F and Lars Fändriks (2014). "Surface area of the digestive tract–revisited". In: *Scandinavian Journal of Gastroenterology* 49.6, pp. 681–689.

Hodgkin, Alan L and Andrew F Huxley (1952). "A quantitative description of membrane current and its application to conduction and excitation in nerve". In: *Journal of Physiology* 117.4, p. 500.

Holland, Amy Marie et al. (2021). "The enteric nervous system in gastrointestinal disease etiology". In: *Cellular and Molecular Life Sciences* 78.10, pp. 4713–4733.

Holzapfel, Gerhard A. (2002). "Nonlinear Solid Mechanics: A Continuum Approach for Engineering Science". In: *Meccanica* 37.4, pp. 489–490.

Hou, Wenfeng et al. (2018). "An advanced k nearest neighbor classification algorithm based on KD-tree". In: *2018 IEEE International Conference of Safety Produce Informatization (IICSPI)*. IEEE, pp. 902–905.

Huang, Huang-Chiao et al. (2013). "Laser welding of ruptured intestinal tissue using plasmonic polypeptide nanocomposite solders". In: *ACS nano* 7.4, pp. 2988–2998.

Innocenti, Giacomo and Roberto Genesio (2009). "On the dynamics of chaotic spiking-bursting transition in the Hindmarsh–Rose neuron". In: *Chaos: An Interdisciplinary Journal of Nonlinear Science* 19.2.

Jadhav, Gauri S, Geet R Adhikari, and Rajashree S Purohit (2022). "A prospective observational study of ventral hernia". In: *Cureus* 14.8.

Kamaludin, Sarah and Prakash Thamburaja (2023). "Efficient neighbour search algorithm for nonlocal-based simulations—Application to failure mechanics". In: *Journal of Failure Analysis and Prevention* 23.2, pp. 540–547.

Keeley, JA et al. (2019). "Predictors of ischemic bowel in patients with incarcerated hernias". In: *Hernia* 23, pp. 277–280.
Klifto, KM et al. (2021). "Risk factors, outcomes, and complications associated with combined ventral hernia and enterocutaneous fistula single-staged abdominal wall reconstruction". In: *Hernia*, pp. 1–12.
Koh, Sang Don et al. (2003). "Conductances responsible for slow wave generation and propagation in interstitial cells of Cajal". In: *Current opinion in pharmacology* 3.6, pp. 579–582.
Kuruppu, Sachira, Leo K Cheng, Timothy R Angeli-Gordon, et al. (2024). "Electromechanical Response of Mesenteric Ischemia Defined Through Simultaneous High-Resolution Bioelectrical and Video Mapping". In: *Annals of Biomedical Engineering* 52.3, pp. 588–599.
Kuruppu, Sachira, Leo K Cheng, Recep Avci, et al. (2022). "Relationship between intestinal slow-waves, spike-bursts, and motility, as defined through high-resolution electrical and video mapping". In: *Journal of Neurogastroenterology and Motility* 28.4, p. 664.
Kyloh, Melinda et al. (2011). "Identification of the visceral pain pathway activated by noxious colorectal distension in mice". In: *Frontiers in neuroscience* 5, p. 16.
Laursen, TA and JC1242927 Simo (1993). "A continuum-based finite element formulation for the implicit solution of multibody, large deformation-frictional contact problems". In: *Int. J. Numer. Methods Eng.* 36.20, pp. 3451–3485.
Li, Yu-Wei et al. (2019). "High-resolution colonic manometry and its clinical application in patients with colonic dysmotility: A review". In: *World Journal of Clinical Cases* 7.18, p. 2675.
Lindeburg, Michael R (2019). *PPI Mechanical Engineering Reference Manual, eText-6 Months, 1 Year*. Simon and Schuster.
Mildenberger, Peter, Marco Eichelberg, and Eric Martin (2002). "Introduction to the DICOM standard". In: *European radiology* 12.4, pp. 920–927.
Misiakos, E et al. (2014). "Strangulated inguinal hernia". In: *Inguinal Hernia* 4, p. 87.
Mlika, Rabii, Yves Renard, and Franz Chouly (2017). "An unbiased Nitsche's formulation of large deformation frictional contact and self-contact". In: *Computer Methods in Applied Mechanics and Engineering* 325, pp. 265–288.
Moazzez, A et al. (2021). "Outcomes of concomitant mesh placement and intestinal procedures during open ventral hernia repair". In: *Hernia* 25, pp. 701–708.

Mushaben, Madaline et al. (2018). “Spatiotemporal modeling of laser tissue soldering using photothermal nanocomposites”. In: *Lasers in Surgery and Medicine* 50.2, pp. 143–152.
Nagaraja, Sindhu et al. (2021). “On a phase-field approach to model fracture of small intestine walls”. In: *Acta Biomaterialia* 130, pp. 317–331.
Nan, Z. et al. (2023). “Strong-anisotropy-induced instability and discussion on kink band under complex loads”. In: *Extreme Mechanics Letters* 62, p. 102043.
Neto, Alfredo Gay and Peter Wriggers (2020). “Numerical method for solution of pointwise contact between surfaces”. In: *Computer Methods in Applied Mechanics and Engineering* 365, p. 112971.
Nisky, Ilana et al. (2015). “Teleoperated versus open needle driving: Kinematic analysis of experienced surgeons and novice users”. In: *2015 IEEE International Conference on Robotics and Automation (ICRA)*. IEEE, pp. 5371–5377.
Paggi, Marco and Giorgio Zavarise (2011). “Contact mechanics of microscopically rough surfaces with graded elasticity”. In: *European Journal of Mechanics – A/Solid* 30.5, pp. 696–704.
Palmada, Nadun, John Edward Cater, et al. (2023). “Anatomically realistic computational model of flow and mixing in the human duodenum”. In: *Physics of Fluids* 35.1.
Palmada, Nadun, Saeed Hosseini, et al. (2023). “A systematic review of computational fluid dynamics models in the stomach and small intestine”. In: *Applied Sciences* 13.10, p. 6092.
Pandolfino, John E and Sabine Roman (2011). “High-resolution manometry: an atlas of esophageal motility disorders and findings of GERD using esophageal pressure topography”. In: *Thoracic surgery clinics* 21.4, pp. 465–475.
Patel, Bhavesh et al. (2022). “Biomechanical constitutive modeling of the gastrointestinal tissues: A systematic review”. In: *Materials & Design.* 217, p. 110576.
Patton, Haley N et al. (2024). “Simultaneous optical imaging of gastric slow waves and contractions in the in vivo porcine stomach”. In: *American Journal of Physiology – Gastrointestinal and Liver Physiology* 327.6, G765–G782.
Piersanti, Roberto et al. (2021). “Modeling cardiac muscle fibers in ventricular and atrial electrophysiology simulations”. In: *Computer Methods in Applied Mechanics and Engineering* 373, p. 113468.
Popp, Alexander, Michael W Gee, and Wolfgang A Wall (2009). “A finite deformation mortar contact formulation using a primal–dual active

set strategy". In: *International Journal for Numerical Methods in Engineering* 79.11, pp. 1354–1391.
Popp, Alexander, Markus Gitterle, et al. (2010). "A dual mortar approach for 3D finite deformation contact with consistent linearization". In: *International Journal for Numerical Methods in Engineering* 83.11, pp. 1428–1465.
Pore, Tejal, Sandeep G Thorat, and Archana A Nema (2021). "Review of contact modelling in nonlinear finite element analysis". In: *Materials Today: Proceedings* 47, pp. 2436–2440.
Poulios, K. and Y. Renard (2015). "An unconstrained integral approximation of large sliding frictional contact between deformable solids". In: *Computers & Structure* 153, pp. 75–90.
Precup, Gabriela and Dan-Cristian Vodnar (2019). "Gut Prevotella as a possible biomarker of diet and its eubiotic versus dysbiotic roles: a comprehensive literature review". In: *British Journal of Surgery* 122.2, pp. 131–140.
Propp, Adrienne et al. (2020). "An orthotropic electro-viscoelastic model for the heart with stress-assisted diffusion". In: *Biomechanics and Modeling in Mechanobiology* 19, pp. 633–659.
Puértolas, S et al. (2020). "A comparative study of hyperelastic constitutive models for colonic tissue fitted to multiaxial experimental testing". In: *Journal of the Mechanical Behavior of Biomedical Materials* 102, p. 103507.
Quarteroni, Alfio et al. (2017). "Integrated heart—coupling multiscale and multiphysics models for the simulation of the cardiac function". In: *Computer Methods in Applied Mechanics and Engineering* 314, pp. 345–407.
Renard, Yves and Konstantinos Poulios (2020). "GetFEM: Automated FE modeling of multiphysics problems based on a generic weak form language". In: *ACM Transactions on Mathematical Software (TOMS)* 47.1, pp. 1–31.
Rossi, Simone et al. (2014). "Thermodynamically consistent orthotropic activation model capturing ventricular systolic wall thickening in cardiac electromechanics". In: *European Journal of Mechanics – A/Solids* 48, pp. 129–142.
Ruiz-Baier, R et al. (2020). "Thermo-electric effects in an anisotropic active-strain electromechanical model". In: *Communications in Computational Physics* 27.1, pp. 87–115.

Sanders, Kenton M, Yoshihiko Kito, et al. (2016). "Regulation of gastrointestinal smooth muscle function by interstitial cells". In: *Physiology* 31.5, pp. 316–326.
Sanders, Kenton M, Sean M Ward, and Sang Don Koh (2014). "Interstitial cells: regulators of smooth muscle function". In: *Physiological Reviews.*
Sauer, Roger A and Laura De Lorenzis (2015). "An unbiased computational contact formulation for 3D friction". In: *International Journal Numerical Methods and Engineering* 101.4, pp. 251–280.
Schmidt, Ryan and Karan Singh (2010). "Meshmixer: an interface for rapid mesh composition". In: *ACM SIGGRAPH 2010 Talks*, pp. 1–1.
Sensoy, Ilkay (2021). "A review on the food digestion in the digestive tract and the used in vitro models". In: *Current Research in Food Science* 4, pp. 308–319.
Sghaier, Asma et al. (2023). "Extensive small bowel necrosis due to congenital para duodenal hernia: A diagnostic and therapeutic challenge: Case Report". In: *International Journal of Surgery Case Reports* 108, p. 108423.
Sharma, Swati and Martin Lindsay Buist (2025). "A comparative study of constitutive relations and variational formulations for modeling gastrointestinal peristalsis". In: *Journal of the Mechanical Behavior of Biomedical Materials* 168, p. 107013.
Sharon, Yarden and Ilana Nisky (2018). "Expertise, teleoperation, and task constraints affect the speed–curvature–torsion power law in RAMIS". In: *Journal of Medical Robotics Research.* 3.03n04, p. 1841008.
Simone, P et al. (2018). "Postbariatric brachioplasty with posteromedial scar: physical model, technical refinements, and clinical outcomes". In: *Plastic and Reconstructive Surgery* 141, pp. 344–353.
Şimşek, Arife et al. (2020). "Factors affecting strangulation and necrosis in incarcerated abdominal wall hernias". In: *Cyprus Journal of Medical Sciences* 5.4, pp. 279–283.
Slater, NJ et al. (2014). "Criteria for definition of a complex abdominal wall hernia". In: *Hernia* 18, pp. 7–17.
Sokolis, Dimitrios P (2021). "Variation of passive biomechanical properties of the small intestine along its length: microstructure-based characterization". In: *Bioengineering* 8.3, p. 32.
Sokolis, Dimitrios P and Sofia G Sassani (2013). "Microstructure-based constitutive modeling for the large intestine validated by histological observations". In: *Journal of the Mechanical Behavior of Biomedical Materials* 21, pp. 149–166.
Stauffer, Clyde M and Christopher Pfeifer (2020). "Colonoscopy". In.

Strik, Chema et al. (2016). "Long-term impact of adhesions on bowel obstruction". In: *Surgery* 159.5, pp. 1351–1359.
Sulaiman, Sarah and Luca Marciani (2019). "MRI of the Colon in the Pharmaceutical Field: The Future before us". In: *Pharmaceutics* 11.4, p. 146.
Tabibian, N et al. (2017). "Abdominal adhesions: A practical review of an often overlooked entity". In: *Annals of Medicine and Surgery* 15, pp. 9–13.
Taffetani, Matteo, Ricardo Ruiz-Baier, and Sarah Waters (2021). "Coupling Stokes flow with inhomogeneous poroelasticity". In: *The Quarterly Journal of Mechanics and Applied Mathematics* 74.4, pp. 411–439.
Temizer, I, P Wriggers, and TJR2877959 Hughes (2012). "Three-dimensional mortar-based frictional contact treatment in isogeometric analysis with NURBS". In: *Computer Methods in Applied Mechanics and Engineering* 209, pp. 115–128.
Turrentine, Florence E et al. (2015). "Morbidity, mortality, cost, and survival estimates of gastrointestinal anastomotic leaks". In: *Journal of the American College of Surgeons* 220.2, pp. 195–206.
Urie, Russell et al. (2015). "Gold nanorod-collagen nanocomposites as photothermal nanosolders for laser welding of ruptured porcine intestines". In: *ACS Biomaterials Science & Engineering* 1.9, pp. 805–815.
Wiesner, W and K Mortele (2011). "Small bowel ischemia caused by strangulation in complicated small bowel obstruction. ct findings in 20 cases with histo-pathological correlation". In: *Journal of the Belgian Society of Radiology* 94.6, pp. 309–314.
Winant, Abbey J et al. (2014). "More than just metastases: a practical approach to solid mesenteric masses". In: *Abdominal imaging* 39.3, pp. 605–621.
Wriggers, P, J Schröder, and A Schwarz (2013). "A finite element method for contact using a third medium". In: *Computational Mechanics* 52, pp. 837–847.
Wriggers, Peter (2006). *Computational Contact Mechanics*. 2nd. Berlin, Heidelberg: Springer. ISBN: 978-3-540-32608-0.
Xiao, Chang-Fang et al. (2024). "Influence of the examination position and distension medium on the rectal sensory test in patients with functional constipation". In: *BMC gastroenterology* 24.1, p. 238.
Xuan, Lingkuan et al. (2024). "A penalty-based cell vertex finite volume method for two-dimensional contact problems". In: *Computational Mechanics*, pp. 1–16.

Yeoh, Jing Wui, Alberto Corrias, and Martin L Buist (2017). "Modelling human colonic smooth muscle cell electrophysiology". In: *Cellular and Molecular Bioengineering* 10, pp. 186–197.

Zel'dovich, Ya B and DA Frank-Kamenetsky (1938). "Towards the theory of uniformly propagating flames". In: *Doklady AN SSSR*. Vol. 19, pp. 693–697.

Unless otherwise expressly stated, all original material of whatever nature created by René Thierry Djoumessi and included in this thesis, is licensed under a Creative Commons Attribution Noncommercial Share Alike 3.0 Italy License.

Check on Creative Commons site:

https://creativecommons.org/licenses/by-nc-sa/3.0/it/legalcode/

https://creativecommons.org/licenses/by-nc-sa/3.0/it/deed.en

Ask the author about other uses.